

Factorisation schemes for proton PDFs

S. Delorme^{a,1}, A. Kusina^{b,1}, A. Siódmok^{c,2}, J. Whitehead^{d,1,2}

¹Institute of Nuclear Physics, Polish Academy of Sciences, 31-342 Kraków, Poland

²Jagiellonian University, ul. prof. Stanisława Łojasiewicza 11, 30-348 Kraków, Poland

Received: date / Accepted: date

Abstract Beyond leading-order, perturbative QCD requires a choice of factorisation scheme to define the parton distribution functions (PDFs) and hard-process cross-section. The modified minimal-subtraction ($\overline{\text{MS}}$) scheme has long been adopted as the default choice due to its simplicity. Alternative schemes have been proposed with specific purposes, including, recently, PDF positivity and NLO parton-shower matching. In this paper we assemble these schemes in a common notation for the first time. We perform a detailed comparison of their features, both analytically and numerically, and estimate the resulting factorisation-scheme uncertainty for LHC phenomenology.

Keywords QCD · Factorization · PDFs

Contents

1	Introduction	1
2	Factorisation schemes	2
	2.1 Notation and definitions	2
	2.2 Summary of scheme motivations	4
	2.3 Scheme definitions	6
3	Scheme comparisons	6
	3.1 PDFs	6
	3.2 Anatomy of transformed PDFs	11
	3.3 Momentum sum-rule	19
	3.4 Number sum-rules	21
	3.5 Positivity	21
	3.6 Coefficient functions	25
4	Phenomenological impact of scheme choice	28
	4.1 Z-plus-jet	29
	4.2 Higgs-plus-jet	29
5	Discussion and conclusions	32
	Appendix A: Notation and conventions	33

Appendix B:	Supplementary transformed PDFs	33
Appendix C:	Supplementary transformation decompositions	33
Appendix D:	Test of perturbative inversion	37
Appendix E:	Validation	37

1 Introduction

Since the first next-to-leading-order (NLO) QCD calculations [1–14] it has been recognised that the factorisation of hadronic cross-sections into a perturbative (short-distance) partonic cross-section, and universal (long-distance) parton distribution functions is not unique beyond leading-order in QCD. The choice of which terms at each perturbative order to treat as universal defines a PDF factorisation scheme (FS). PDFs in different schemes are related to each other by convolution with a transformation kernel, which is defined perturbatively up to the relevant order in α_s .

While NLO calculations using different schemes have the same formal perturbative accuracy, their predictions may nevertheless differ through the inclusion of different higher-order terms. These higher-order terms, especially when logarithmic, may be numerically large, and their effects significant.

Early calculations favoured the DIS scheme [1], defined to absorb all perturbative corrections to the deep inelastic scattering cross-section into the parton distribution functions. Subsequently, the modified-minimal-subtraction ($\overline{\text{MS}}$) scheme [2] came into favour due to its simplicity. Today, $\overline{\text{MS}}$ is the ‘default’ factorisation scheme in use for the overwhelming majority of QCD calculations and predictions.

In the intervening period, a number of alternative factorisation schemes have been proposed with a range of motivations. These include recent proposals for a new

^ae-mail: stephane.delorme@ifj.edu.pl

^be-mail: aleksander.kusina@ifj.edu.pl

^ce-mail: andrzej.siodmok@uj.edu.pl

^de-mail: james.whitehead@uj.edu.pl

scheme to enforce the positivity of PDFs [15], schemes for NLO calculations matched to parton showers [16–21], and a scheme aiming to separate short- from long-distance corrections using arguments about dimensional regularisation and confinement [22].

In this paper, we summarise the different schemes, their motivations, and collect their definitions in relation to $\overline{\text{MS}}$ PDFs in consistent conventions using a unified notation. We compare the schemes both analytically and numerically, identify common elements, assess their numerical significance at the level of PDFs and coefficient functions, and consider the possible impact of the factorisation-scheme choice for practical phenomenology. We conclude by identifying a small number of discrete parameters which span much of the deviation between the schemes.

2 Factorisation schemes

We work within the formalism of collinear factorisation [23–25] which relates a hadronic cross-section to the convolution of a perturbatively-calculable coefficient function, C , independent of hadronic physics, with non-perturbative PDFs f_i describing the distribution of parton i within the hadron (here, the proton). For DIS-like processes, with a single PDF, this can schematically be written as:

$$\sigma_{lh}(\mu_F, \mu_R) = \sigma_0 \sum_i f_i(\mu_F) \otimes C_i(\mu_F, \mu_R), \quad (1)$$

and for Drell–Yan-like processes, with two PDFs, as:

$$\sigma_{hh}(\mu_F, \mu_R) = \sigma_0 \sum_{i,j} f_i(\mu_F) \otimes f_j(\mu_F) \otimes C_{ij}(\mu_F, \mu_R), \quad (2)$$

where higher-twist terms of the order of $\mathcal{O}(\Lambda_{\text{QCD}}^2/\mu_F^2)$ are neglected, indices i, j run over partonic flavours, μ_F and μ_R denote factorisation and renormalisation scales respectively, and the convolution \otimes is defined as:

$$\begin{aligned} (f \otimes g)(x) &:= \int_x^1 \frac{dz}{z} f(z) g\left(\frac{x}{z}\right) \\ &\equiv \int_0^1 dz \int_0^1 dy \delta(x - yz) f(y) g(z). \end{aligned} \quad (3)$$

For the result to be factorisation-scheme independent, the factorisation-scheme-dependent PDFs and coefficient functions must each compensate for the factorisation-scheme dependence of the other.

2.1 Notation and definitions

2.1.1 Factorisation scheme transformations

We define PDFs in different factorisation schemes according to their relationship with PDFs in the $\overline{\text{MS}}$ scheme, via a transformation of the form

$$\mathbf{f}^{\text{FS}} = \mathbb{K}^{\overline{\text{MS}} \rightarrow \text{FS}} \otimes \mathbf{f}^{\overline{\text{MS}}}, \quad (4)$$

where explicitly

$$f_a^{\text{FS}}(x, \mu) = \sum_b \int_x^1 \frac{dz}{z} \mathbb{K}_{ab}^{\overline{\text{MS}} \rightarrow \text{FS}}(z, \mu) f_b^{\overline{\text{MS}}}\left(\frac{x}{z}, \mu\right), \quad (5)$$

performed locally for each scale μ .

We expand the matrix of convolution kernels $\mathbb{K}_{ab}^{\overline{\text{MS}} \rightarrow \text{FS}}$ perturbatively as¹

$$\begin{aligned} \mathbb{K}_{ab}^{\overline{\text{MS}} \rightarrow \text{FS}}(z, \mu) &= \delta_{ab} \delta(1-z) + \frac{\alpha_s(\mu)}{2\pi} \mathbb{K}_{ab}^{\overline{\text{MS}} \rightarrow \text{FS}}(z, \mu) \\ &\quad + \mathcal{O}(\alpha_s^2). \end{aligned} \quad (6)$$

Equivalently, for convenience, we can express the same transformation using

$$(xf)(z, \mu_F) \equiv z f(z, \mu_F) \quad (7)$$

instead of $f(z, \mu_F)$ (as is provided for example by the LHAPDF library [26]). Then,

$$\begin{aligned} (xf)_a^{\text{FS}}(x, \mu_F) &= \sum_b \int_x^1 dz \mathbb{K}_{ab}^{\overline{\text{MS}} \rightarrow \text{FS}}(z, \mu_F) (xf_b)^{\overline{\text{MS}}}\left(\frac{x}{z}, \mu_F\right). \end{aligned} \quad (8)$$

To order α_s , this transformation has perturbative inversion

$$\begin{aligned} \mathbb{K}_{ab}^{\text{FS} \rightarrow \overline{\text{MS}}}(z, \mu) &= \delta_{ab} \delta(1-z) - \frac{\alpha_s(\mu)}{2\pi} \mathbb{K}_{ab}^{\overline{\text{MS}} \rightarrow \text{FS}}(z) \\ &\quad + \mathcal{O}(\alpha_s^2), \end{aligned} \quad (9)$$

and so

$$\mathbb{K}_{ab}^{\text{FS} \rightarrow \overline{\text{MS}}}(z) = -\mathbb{K}_{ab}^{\overline{\text{MS}} \rightarrow \text{FS}}(z). \quad (10)$$

We therefore specify only the ‘forward’ transformation.²

Other perturbative expansions in α_s are given according to the convention

$$\begin{aligned} F(\alpha_s, \mu) &= F^{(0)}(\mu) + \left(\frac{\alpha_s(\mu)}{2\pi}\right) F^{(1)}(\mu) + \dots \\ &= \sum_k \left(\frac{\alpha_s(\mu)}{2\pi}\right)^k F^{(k)}(\mu). \end{aligned} \quad (11)$$

¹In general we will suppress the possible explicit μ -dependence of $\mathbb{K}_{ab}^{\overline{\text{MS}} \rightarrow \text{FS}}(z, \mu)$.

²In Appendix D we test the validity of this perturbative inversion numerically.

2.1.2 Coefficient functions

We write the hadronic cross-section for hadron-hadron boson-production process $pp \rightarrow V + X$, differential with respect to the invariant mass (squared) of the boson, within the framework of collinear factorisation as

$$\frac{d\sigma}{dM^2}(P_1, P_2) = \sigma^{(0)} \frac{M^2}{s} \int_0^1 d\xi_1 d\xi_2 dz \delta\left(\xi_1 \xi_2 z - \frac{M^2}{s}\right) \sum_{a,b} f_a^{\text{FS}}(\xi_1, \mu_F) f_b^{\text{FS}}(\xi_2, \mu_F) C_{ab}^{\text{FS}}(z, M; \mu_F, \mu_R) \quad (12)$$

for partonic flavours a, b , FS-scheme parton distribution functions $f_a^{\text{FS}}, f_b^{\text{FS}}$, incoming hadronic momenta P_1, P_2 and collinear momentum fractions $\xi_{1,2}$. The partonic coefficient function $C_{ab}^{\text{FS}}(z, M; \mu_F, \mu_R)$ is normalised to the pointlike Born cross-section by the $\sigma^{(0)}$ factor, and may be expanded perturbatively; for the processes we consider, the leading-order contribution is $\delta(1-z)$ for the active partonic flavours.

Since the left-hand-side of Eq. (12) is explicitly independent of the (unphysical) choice of factorisation-scheme, so must the right-hand-side be. Rewriting the double-convolution integral as a matrix in flavour-space using the notation of Eq. (4),

$$\left[\mathbf{f}^{\text{FS}\top} \otimes \mathbf{C}^{\text{FS}} \otimes \mathbf{f}^{\text{FS}} \right] \left(\frac{M^2}{s} \right) \quad (13)$$

$$\begin{aligned} &\equiv \mathbf{f}^{\overline{\text{MS}}\top} \otimes \mathbb{K}^{\overline{\text{MS}} \rightarrow \text{FS}\top} \otimes \mathbf{C}^{\text{FS}} \otimes \mathbb{K}^{\overline{\text{MS}} \rightarrow \text{FS}} \otimes \mathbf{f}^{\overline{\text{MS}}} \\ &= \mathbf{f}^{\overline{\text{MS}}\top} \otimes \mathbb{K}^{\overline{\text{MS}} \rightarrow \text{FS}\top} \otimes \left(\mathbb{K}^{\overline{\text{MS}} \rightarrow \text{FS}\top} \right)^{-1} \\ &\quad \otimes \mathbf{C}^{\overline{\text{MS}}} \otimes \left(\mathbb{K}^{\overline{\text{MS}} \rightarrow \text{FS}} \right)^{-1} \otimes \mathbb{K}^{\overline{\text{MS}} \rightarrow \text{FS}} \otimes \mathbf{f}^{\overline{\text{MS}}} \\ &\equiv \left[\mathbf{f}^{\overline{\text{MS}}\top} \otimes \mathbf{C}^{\overline{\text{MS}}} \otimes \mathbf{f}^{\overline{\text{MS}}} \right] \left(\frac{M^2}{s} \right), \end{aligned} \quad (14)$$

where factorisation-scheme independence provides the equality in Eq. (14). Therefore

$$\mathbf{C}^{\text{FS}} = \mathbb{K}^{\text{FS} \rightarrow \overline{\text{MS}}\top} \otimes \mathbf{C}^{\overline{\text{MS}}} \otimes \mathbb{K}^{\overline{\text{MS}} \rightarrow \text{FS}}, \quad (15)$$

or to NLO in perturbation theory,

$$C_{ab}^{\text{FS}(0)} = C_{ab}^{\overline{\text{MS}}(0)} \quad (16)$$

$$\begin{aligned} C_{ab}^{\text{FS}(1)} &= C_{ab}^{\overline{\text{MS}}(1)} \\ &\quad - \sum_c \left[\mathbb{K}_{ca}^{\overline{\text{MS}} \rightarrow \text{FS}} \otimes C_{cb}^{\overline{\text{MS}}(0)} + C_{ac}^{\overline{\text{MS}}(0)} \otimes \mathbb{K}_{cb}^{\overline{\text{MS}} \rightarrow \text{FS}} \right]. \end{aligned} \quad (17)$$

For processes with flavour-diagonal leading-order coefficient functions this reduces to

$$C_{ab}^{\overline{\text{MS}}(1)} - \mathbb{K}_{ba}^{\overline{\text{MS}} \rightarrow \text{FS}} \otimes C_{bb}^{\overline{\text{MS}}(0)} - C_{aa}^{\overline{\text{MS}}(0)} \otimes \mathbb{K}_{ab}^{\overline{\text{MS}} \rightarrow \text{FS}}. \quad (18)$$

For the processes considered here, only one of the transition terms above will contribute unless $a = b$; since the

coefficient functions are consistently normalised to be $\delta(1-z)$ at leading-order, explicit dependence on $C^{\overline{\text{MS}}(0)}$ will drop out completely.

2.1.3 DGLAP evolution

The DGLAP equations [27–29] familiar from $\overline{\text{MS}}$ calculations also hold in other factorisation schemes [30], albeit with modified splitting functions \mathbb{P}^{FS} :

$$\mu^2 \frac{\partial}{\partial \mu^2} \mathbf{f}^{\text{FS}}(\mu) = \mathbb{P}^{\text{FS}}(\mu) \otimes \mathbf{f}^{\text{FS}}(\mu). \quad (19)$$

The relationship between the splitting functions in factorisation scheme FS and $\overline{\text{MS}}$ can be obtained upon taking the logarithmic derivative $\partial/\partial(\log \mu^2)$ of Eq. (4).

$$\begin{aligned} \mathbb{P}^{\text{FS}}(\mu) &= \mu^2 \left(\frac{\partial}{\partial \mu^2} \mathbb{K}^{\overline{\text{MS}} \rightarrow \text{FS}}(\mu) \right) \otimes \mathbb{K}^{\text{FS} \rightarrow \overline{\text{MS}}}(\mu) \\ &\quad + \mathbb{K}^{\overline{\text{MS}} \rightarrow \text{FS}}(\mu) \otimes \mathbb{P}^{\overline{\text{MS}}}(\mu) \otimes \mathbb{K}^{\text{FS} \rightarrow \overline{\text{MS}}}(\mu) \end{aligned} \quad (20)$$

or, using the perturbative expansion of Eq. (6) and expanding according to the convention of Eq. (11),

$$\mathbf{P}_{ab}^{\text{FS}(0)} = \mathbf{P}_{ab}^{\overline{\text{MS}}(0)} \equiv 0 \quad (21)$$

$$\mathbf{P}_{ab}^{\text{FS}(1)} = \mathbf{P}_{ab}^{\overline{\text{MS}}(1)} + \mu^2 \frac{\partial}{\partial \mu^2} \mathbb{K}_{ab}^{\overline{\text{MS}} \rightarrow \text{FS}}(\mu) \quad (22)$$

$$\begin{aligned} \mathbf{P}_{ab}^{\text{FS}(2)} &= \mathbf{P}_{ab}^{\overline{\text{MS}}(2)} + \mu^2 \frac{\partial}{\partial \mu^2} \mathbb{K}_{ab}^{\overline{\text{MS}} \rightarrow \text{FS}(2)}(\mu) \\ &\quad - \sum_c \left(\mu^2 \frac{\partial}{\partial \mu^2} \mathbb{K}_{ac}^{\overline{\text{MS}} \rightarrow \text{FS}}(\mu) \right) \otimes \mathbb{K}_{cb}^{\overline{\text{MS}} \rightarrow \text{FS}}(\mu) \\ &\quad + \frac{\beta^{(2)}}{2\pi} \mathbb{K}_{ab}^{\overline{\text{MS}} \rightarrow \text{FS}}(\mu) \\ &\quad + \sum_c \left(\mathbb{K}_{ac}^{\overline{\text{MS}} \rightarrow \text{FS}}(\mu) \otimes \mathbf{P}_{cb}^{\overline{\text{MS}}(1)} \right. \\ &\quad \left. - \mathbf{P}_{ac}^{\overline{\text{MS}}(1)} \otimes \mathbb{K}_{cb}^{\overline{\text{MS}} \rightarrow \text{FS}}(\mu) \right). \end{aligned} \quad (23)$$

The modifications to the DGLAP kernels therefore arise in turn from any explicit scale-dependence of the transformation kernels $\mathbb{K}^{\overline{\text{MS}} \rightarrow \text{FS}}(z; \mu)$, the QCD β -function, and the $\overline{\text{MS}}$ DGLAP kernels of the input partons.

For the NLO factorisation-scheme transformations considered in our paper, in which there is no explicit dependence within \mathbb{K} on μ ,³ the PDFs in alternative schemes therefore obey a DGLAP evolution equation that is modified only at NLO and above.

Therefore, the DGLAP evolution and factorisation scheme transformation commute, up to remainder that

³Note that in Eq. (6), and elsewhere, we suppress the possible explicit μ -dependence of $\mathbb{K}_{ab}^{\overline{\text{MS}} \rightarrow \text{FS}}(z, \mu)$; the factorisation schemes we consider here have no such dependence. In general, there is no obstacle to it; such a dependence features in the DEDUCTOR shower-oriented schemes [21].

is higher-orders in perturbation theory. Specifically, a PDF evolved from its input parametrisation using the $\overline{\text{MS}}$ N^kLO evolution equations and then transformed into another scheme will not satisfy precisely the same evolution equations as a PDF transformed at its input scale and then evolved using the modified DGLAP equations.⁴ In the former case, the effective terms $P_{ab}^{\text{FS}(k+2)}$ and higher are non-zero, while in the latter case, the series expansion of the kernels is truncated at the chosen order.

2.1.4 Momentum sum rule

To compare factorisation schemes on a like-for-like basis, we consistently impose the momentum sum-rule [33]

$$\sum_a \int_0^1 \xi f_a^{\text{FS}}(\xi, \mu) d\xi = 1, \quad (24)$$

or equivalently at the level of the transformation kernels,

$$\sum_a \int_0^1 z K_{ab}^{\overline{\text{MS}} \rightarrow \text{FS}}(z) dz = 0 \quad (25)$$

for all flavours b .

Except where otherwise specified by the authors of the scheme, this is imposed through a virtual-type modification of the $\delta(1-z)$ component of the flavour-diagonal transformation kernels,

$$K_{bb}^{\overline{\text{MS}} \rightarrow \text{FS}}(z) = K_{bb}^{\overline{\text{MS}} \rightarrow \text{FS}}(z) - \delta(1-z) \sum_a \int_0^1 z' K_{ab}^{\overline{\text{MS}} \rightarrow \text{FS}}(z') dz'. \quad (26)$$

2.1.5 Flavour thresholds

Within Eq. (5) the $K_{gg}^{\overline{\text{MS}} \rightarrow \text{FS}}$ kernels act upon an input $\overline{\text{MS}}$ gluon PDF to produce a contribution to an output (FS scheme) quark PDF. Heavy quark and antiquark flavours⁵ q_f, \bar{q}_f are typically chosen to have no ‘intrinsic’ contribution to the proton PDF; that is, they are chosen to be zero below some threshold scale μ_f of the order of the quark mass m_f , and generated purely by DGLAP evolution above this scale.

⁴A recent proposal to resolve the factorisation-scheme-dependence of DGLAP evolution was advanced in [31, 32], in which the perturbative relationship between six linearly-independent DIS structure functions and the proton PDFs was inverted to derive a ‘physical’, scheme-independent DGLAP-type evolution equation for structure functions as a function of the physical (momentum-transfer) scale.

⁵For the purpose of this section, ‘heavy’ means charm and bottom, depending on the conventions adopted by the PDF-fitting group.

For such PDFs we enforce explicitly that the output, transformed, PDF is also zero below the threshold, i.e.

$$\mathbb{K}_{qfb}^{\overline{\text{MS}} \rightarrow \text{FS}}(z, \mu) = \Theta[\mu > \mu_f] \mathbb{K}_{qfb}^{\overline{\text{MS}} \rightarrow \text{FS}}(z, \mu); \quad (27)$$

this leads in general to a discontinuity at the threshold,⁶ in both f_g and f_{q_f} . The mixing from the gluon via the transformation convolution is turned on suddenly, even if the DGLAP evolution of the input $\overline{\text{MS}}$ PDF has a continuous solution (possible at NLO through the choice $\mu_f = m_f$). Similar discontinuities at the flavour thresholds occur naturally at NNLO and beyond, as a consequence of constant terms in matching conditions [34–36].

The ‘turning on’ of the transformation from the gluon at the threshold $\mu = \mu_f$ also requires n_f to be incremented by 1 to maintain momentum conservation Eq. (25). This happens because the expression on the right-hand-side of Eq. (26) contains additional non-zero kernels above the threshold; i.e.

$$n_f(\mu) = \sum_f \Theta[\mu > \mu_f]. \quad (28)$$

This is equivalent to the usual definition of the variable-flavour-number scheme (VFNS), e.g. [37–41], used for the solution of the DGLAP evolution equations.

2.2 Summary of scheme motivations

2.2.1 $\overline{\text{MS}}$ scheme

The $\overline{\text{MS}}$ scheme [2] is used for its theoretical simplicity and practical convenience. Parton distributions in the $\overline{\text{MS}}$ scheme are defined as renormalised expectation values of the partonic number operator in the hadronic state [4, 33, 42]. For partonic calculations in perturbation theory this choice is ‘minimal’ by virtue of absorbing only the ε -pole and universal numerical factors into the PDF renormalisation coefficients defining the PDF, and no finite terms.

2.2.2 DIS scheme

The DIS scheme [1] uses the freedom to choose a factorisation scheme to absorb the higher-order DIS coefficient

⁶Since we expect in general to introduce a discontinuity in the transformed PDFs at the quark-thresholds, in practice, we split the LHAPDF grids at the thresholds and compute the two limits $\lim_{\mu \rightarrow \mu_f \pm} [f_a^{\text{FS}}(x, \mu)]$ separately to store in the interpolation grids. The PDF values within each grid are therefore computed with a single value of n_f and a single set of active kernels, so represent a continuous function which may be approximated with an interpolation by standard methods. Further technical details are given in Appendix E.

functions into the PDFs, including the gluon-initiated partonic contribution, extending the leading-order relation for the structure function

$$F_2(x, \mu^2) \equiv x \sum_f Q_f^2 \left(f_{qf}^{\text{DIS}}(x, \mu) + f_{\bar{q}f}^{\text{DIS}}(x, \mu) \right) \quad (29)$$

to all orders of perturbation theory. Calculations for other processes must therefore be adjusted by the DIS matrix-elements to restore perturbative accuracy.

We follow [43] and adopt the convention in which the DIS-scheme gluon PDF is determined by the extension to all Mellin moments of the momentum conservation constraint on the second moment, which implies

$$\overline{K}_{qg}^{\overline{\text{MS}} \rightarrow \text{DIS}} = -\overline{K}_{qq}^{\overline{\text{MS}} \rightarrow \text{DIS}} \quad (30)$$

$$\overline{K}_{gg}^{\overline{\text{MS}} \rightarrow \text{DIS}} = -2n_f \overline{K}_{gq}^{\overline{\text{MS}} \rightarrow \text{DIS}}. \quad (31)$$

This is equivalent to strengthening Eq. (24) from a sum-rule that holds only upon integration to a constraint local in ξ ,⁷

$$\sum_a \xi f_a^{\text{DIS}}(\xi, \mu) = \sum_a \xi f_a^{\overline{\text{MS}}}(\xi, \mu) \quad \text{for all } \xi \in [0, 1]. \quad (32)$$

2.2.3 KRK scheme

The KRKDY scheme [16, 17] uses for its factorisation scheme transformation the collinear convolution terms arising from the integral of Catani–Seymour subtraction dipoles [44] over the unresolved phase-space for colour-singlet final states. By absorbing these collinear counterterms into the PDFs rather than including them in the hard-process, matched NLO-plus-parton-shower calculations can be implemented using only positive multiplicative weights (the KrkNLO method [16, 18, 20]).

The full KRK scheme extends the KRKDY scheme to all partonic flavours [17], defining a transformation for the gluon PDF using the gluon-gluon fusion Higgs-production process in the infinite-top-mass limit [18].

2.2.4 DPOS/POS/MPOS/MPOS δ schemes

In [15] the authors identify the origin of negativity in $\overline{\text{MS}}$ -scheme coefficient functions to be an oversubtraction within the $\overline{\text{MS}}$ scheme. This arises from a mismatch of scales for collinear emission between the hard-process and the $\overline{\text{MS}}$ subtraction term and leads to terms proportional to $\log(1-z)$ for off-diagonal splittings, which become arbitrarily negative for $z \rightarrow 1$.

In the DPOS and POS schemes the subtraction is performed at a modified scale (defined correspondingly

based on DIS and DY processes) to ensure the coefficient function remains positive. This is argued to be inadequate in [45] and the argument is refined in [46].

The MPOS scheme is a modification of the POS scheme which enforces momentum conservation by adding a choice of ‘soft’ function to the diagonal elements. In this work, we will also refer to the MPOS δ scheme, which we define to be identical to MPOS save for the imposition of momentum-conservation through a virtual-like delta-function contribution instead of a soft function (to be comparable with all other schemes).⁸

2.2.5 AVERSA scheme

The AVERSA scheme [13] aims to remove large universal logarithmic terms of kinematic origin from coefficient functions and move them instead into the PDFs (and fragmentation functions), in order to improve the perturbative convergence and scale-dependence of NLO predictions.

2.2.6 PHYS scheme

The PHYS scheme [22] aims to remove finite ε/ε contributions of IR origin which emerge in the $\overline{\text{MS}}$ scheme from long-distance interactions between massless QCD partons. Because of confinement it is argued that any terms related to long-distance QCD interactions between partons must be unphysical, and should be removed (hence ‘PHYS’).

2.2.7 Others

Finally, we do not include in our comparisons, but wish to mention, the DEDUCTOR family of ‘shower-oriented’ schemes [21, 47, 48] and the Ramalho–Sterman [8] and Sterman [9] schemes.

The DEDUCTOR family of ‘shower-oriented’ schemes [21, 47, 48] for use with parton-shower evolution in the DEDUCTOR framework [21, 47–52] is defined by a transformation from the $\overline{\text{MS}}$ scheme that is dependent on the ordering variable used within the shower, so that the DGLAP evolution of the PDFs matches that of the initial-state evolution within the shower.

The Ramalho–Sterman scheme outlined in [8] was introduced as an alternative to the DIS scheme to ensure that the Mellin moments of the Drell–Yan process were bounded in N , by absorbing terms with moments proportional to $\log^2 N$ (arising from plus-distribution factors \mathcal{D}_1 ,⁹ associated with soft-gluons) into the PDF.

⁸The significance of this change is explored in Sec. 3.3.2.

⁹See Eq. (34).

⁷The effect of this may be seen graphically in Fig. 8a.

Sterman [9] defines two factorisation schemes, for the Drell–Yan and DIS processes separately, in which the real and virtual contributions are separately finite, and all ‘threshold logarithm’ distribution terms \mathcal{D}_k are absorbed into the PDFs, curing the coefficient functions of their large- N logarithms in Mellin space. Factorisation-scheme independence then allows the identification and all-order resummation of the threshold logarithms.

2.3 Scheme definitions

Throughout we adopt the convention of decomposing convolution kernels as arise up to NLO in QCD as:

$$K(z) = \sum_{k=0}^1 a_k \mathcal{D}_k(z) + b(z) \log(1-z) + c(z) \log z \quad (33)$$

$$+ P(z) - \Delta \delta(1-z)$$

where $b(z), c(z), P(z)$ are rational functions and, concretely, for all the kernels we consider, can be expressed as Laurent series with at most simple poles at $z = 0, 1$. The distributions $\mathcal{D}_k(z)$ are defined as

$$\mathcal{D}_k(z) = \left[\frac{\log^k(1-z)}{1-z} \right]_+ \quad (34)$$

where the ‘plus-distribution’ regularisation, for functions otherwise singular at $z = 1$, is defined by its action upon integration against a smooth function f as

$$\int_x^1 dz f(z) \left[\frac{g(z)}{1-z} \right]_+ = \int_x^1 dz \frac{f(z) - f(1)}{1-z} g(z) \quad (35)$$

$$- f(1) \int_0^x dz \frac{g(z)}{1-z}.$$

Transformation kernels $K_{ab}^{\text{FS}}(x)$ for the considered schemes are introduced in Sec. 3 and listed in this convention in Tables 1 to 4. For ease of reference, the LO DGLAP splitting functions used within the tables are given in Appendix A.

3 Scheme comparisons

In this section we examine the effects of the transformations given in Tables 1 to 4. In Sec. 3.1 we simply show the transformed PDFs themselves, at ‘low’ (2 GeV) and ‘characteristic LHC’ (100 GeV) scales. In Sec. 3.2 we break down each transformation into the constituent contributions from the decomposition of Eq. (33), and further according to the flavour of the input-PDF. In Sec. 3.3 we examine the effect of the transformations on the momentum sum-rule, and in Sec. 3.4 on the number

sum-rules. Section 3.5 discusses the positivity of PDFs in different schemes. Finally, in Sec. 3.6 we examine the consequence of each of the considered factorisation schemes on the coefficient functions of the DIS, Drell–Yan and (gluon-fusion) Higgs production processes.

Throughout this section, we emphasise that there are three inequivalent methods of obtaining a PDF set in a given factorisation scheme:

- (i) by direct fitting in the desired scheme;
- (ii) by transforming a PDF fitted in another scheme at the input-scale, and performing DGLAP evolution in the new scheme, as discussed in Sec. 2.1.3;
- (iii) by transforming a PDF fitted and DGLAP-evolved in another scheme locally at each scale, using Eq. (5).

We restrict ourselves to PDFs obtained using (iii), applied to modern PDF sets in common use, fitted and DGLAP-evolved in the $\overline{\text{MS}}$ scheme.¹⁰

3.1 PDFs

In Fig. 1 we show the results of numerically transforming $\overline{\text{MS}}$ PDFs fitted by the CTEQ collaboration (CT18NLO [56]) into the discussed schemes using the kernels given in Tables 1 to 4. Similar plots produced using PDF sets fitted by other groups are given in Fig. 17 (NNPDF40MC [57]) and Fig. 18 (MSHT20nLo [58]) in Appendix B. Details of the numerical codes used to perform the convolutions are given in Appendix E.

The most dramatic difference can be seen in the low- x gluon distribution, in Fig. 1c. This is especially pronounced for the KRK and MPOS (MPOS δ) schemes at low scales, for which the low- x gluon is up to an order of magnitude larger than in the $\overline{\text{MS}}$ and other schemes. As we will show in Sec. 3.2, this effect is primarily due to the form of $K_{gg}^{\overline{\text{MS}} \rightarrow \text{FS}}$. This behaviour persists at higher scales but is substantially reduced in magnitude. An example illustrating the effect of this on phenomenology is shown in Fig. 15.

Another apparent feature is the difference in the u -valence (and d -valence) quark peak at large $x \sim 0.2$ which can be observed at low scales (see Figs. 1a and 16a). This is partly washed out at higher scales by the DGLAP evolution. The light quarks and anti-quarks (Figs. 1b and 16b to 16d) exhibit differences at low x -values which persist to large factorisation scales.

The charm quark PDF (Fig. 1d) shows a relatively large spread between the schemes and interestingly, for

¹⁰Historically, the differences between DIS-scheme PDFs obtained via the former and the latter methods motivated simultaneous independent fits in the $\overline{\text{MS}}$ and DIS schemes using the same data and methodology [53–55].

$C_F^{-1}K_{qq}^{\overline{\text{MS}}\rightarrow\text{FS}}$	\mathcal{D}_1	\mathcal{D}_0	$\log(1-z)$	$\log z$	$P(z)$	$-\delta(1-z)$
AVERSA	2	$-\frac{3}{2}$	$-(1+z)$	$-p_{qq}(z)$	$3+2z$	$\frac{\pi^2}{3} + \frac{9}{2}$
DIS	2	$-\frac{3}{2}$	$-(1+z)$	$-p_{qq}(z)$	$3+2z$	$\frac{\pi^2}{3} + \frac{9}{2}$
KRK	4		$-2(1+z)$	$-p_{qq}(z)$	$1-z$	$\frac{\pi^2}{3} + \frac{17}{4}$
KRKDY	4		$-2(1+z)$	$-p_{qq}(z)$	$1-z$	$\frac{\pi^2}{3} + \frac{11}{4}$
DPOS						
POS						
MPOS					$\frac{350}{3}z^2(1-z)^2$	
MPOS δ						$-\frac{35}{18}$
PHYS	2		$-(1+z)$		$1-z$	$\frac{11}{4}$

Table 1: Transformation kernels $K_{qq}^{\text{FS}}(x)$, in the notation of Eq. (33). Note that $K_{qq}^{\text{POS}} = K_{qq}^{\text{DPOS}} \equiv 0$.

$T_R^{-1}K_{qq}^{\overline{\text{MS}}\rightarrow\text{FS}}$	\mathcal{D}_1	\mathcal{D}_0	$\log(1-z)$	$\log z$	$P(z)$	$-\delta(1-z)$
AVERSA			$p_{qq}(z)$	$-p_{qq}(z)$		
DIS			$p_{qq}(z)$	$-p_{qq}(z)$	$-4p_{qq}(z) + 3$	
KRK			$2p_{qq}(z)$	$-p_{qq}(z)$	$-p_{qq}(z) + 1$	
KRKDY			$2p_{qq}(z)$	$-p_{qq}(z)$	$-p_{qq}(z) + 1$	
DPOS			$p_{qq}(z)$	$-p_{qq}(z)$	$-p_{qq}(z)$	
POS			$2p_{qq}(z)$	$-p_{qq}(z)$	$-p_{qq}(z)$	
MPOS			$2p_{qq}(z)$	$-p_{qq}(z)$	$-p_{qq}(z)$	
MPOS δ			$2p_{qq}(z)$	$-p_{qq}(z)$	$-p_{qq}(z)$	
PHYS			$p_{qq}(z)$		$-p_{qq}(z) + 1$	

Table 2: Transformation kernels $K_{qq}^{\text{FS}}(x)$, in the notation of Eq. (33).

$C_F^{-1}K_{gg}^{\overline{\text{MS}}\rightarrow\text{FS}}$	\mathcal{D}_1	\mathcal{D}_0	$\log(1-z)$	$\log z$	$P(z)$	$-\delta(1-z)$
AVERSA			$p_{gq}(z)$	$-p_{gq}(z)$	$-\frac{4}{3}$	
DIS	-2	$\frac{3}{2}$	$1+z$	$p_{gq}(z)$	$-3-2z$	$-\frac{\pi^2}{3} - \frac{9}{2}$
KRK			$2p_{gq}(z)$	$-p_{gq}(z)$	z	
POS			$2p_{gq}(z)$	$-p_{gq}(z)$	$-p_{gq}(z)$	
MPOS			$2p_{gq}(z)$	$-p_{gq}(z)$	$-p_{gq}(z)$	
MPOS δ			$2p_{gq}(z)$	$-p_{gq}(z)$	$-p_{gq}(z)$	
PHYS			$p_{gq}(z)$		z	

Table 3: Transformation kernels $K_{gg}^{\text{FS}}(x)$, in the notation of Eq. (33). Note that $K_{gg}^{\text{KRKDY}} = K_{gg}^{\text{DPOS}} \equiv 0$.

$C_A^{-1}K_{gg}^{\overline{\text{MS}}\rightarrow\text{FS}}$	\mathcal{D}_1	\mathcal{D}_0	$\log(1-z)$	$\log z$	$P(z)$	$-\delta(1-z)$
AVERSA	2		-2	$-2\frac{z}{1-z}$		$\frac{\pi^2}{3} + 1 - \frac{5}{6}\frac{T_R n_f}{C_A}$
$(-2n_f T_R)^{-1}K_{gg}^{\overline{\text{MS}}\rightarrow\text{DIS}}$			$p_{gq}(z)$	$-p_{gq}(z)$	$-4p_{gq}(z) + 3$	
KRK	4		$4(\frac{1}{z} - 2 + z(1-z))$	$-2p_{gq}(z)$		$\frac{\pi^2}{3} + \frac{341}{72} - \frac{59}{36}\frac{T_R n_f}{C_A}$
MPOS					$\frac{475}{3}\frac{T_R n_f}{C_A}z^2(1-z)^2$	
MPOS δ						$-\frac{95}{36}\frac{T_R n_f}{C_A}$
PHYS	2		$2(\frac{1}{z} - 2 + z(1-z))$			$\frac{203}{72} - \frac{29}{36}\frac{T_R n_f}{C_A}$

Table 4: Transformation kernels $K_{gg}^{\text{FS}}(x)$, in the notation of Eq. (33). Note that $K_{gg}^{\text{KRKDY}} = K_{gg}^{\text{POS}} = K_{gg}^{\text{DPOS}} \equiv 0$.

$C_F^{-1}C_q^{(1)FS}$	\mathcal{D}_1	\mathcal{D}_0	$\log(1-z)$	$\log z$	$P(z)$	$-\delta(1-z)$
$\overline{\text{MS}}$	2	$-\frac{3}{2}$	$-(1+z)$	$-p_{qq}(z)$	$3+2z$	$\frac{\pi^2}{3} + \frac{9}{2}$
DIS, AVERSA						
KRK	-2	$-\frac{3}{2}$	$1+z$		$2+3z$	$\frac{1}{4}$
KRKDY	-2	$-\frac{3}{2}$	$1+z$		$2+3z$	$\frac{7}{4}$
POS, DPOS	2	$-\frac{3}{2}$	$-(1+z)$	$-p_{qq}(z)$	$3+2z$	$\frac{\pi^2}{3} + \frac{9}{2}$
MPOS	2	$-\frac{3}{2}$	$-(1+z)$	$-p_{qq}(z)$	$3+2z - \frac{350}{3}z^2(1-z)^2$	$\frac{\pi^2}{3} + \frac{9}{2}$
MPOS δ	2	$-\frac{3}{2}$	$-(1+z)$	$-p_{qq}(z)$	$3+2z$	$\frac{\pi^2}{3} + \frac{9}{2} + \frac{35}{18}$
PHYS		$-\frac{3}{2}$		$-p_{qq}(z)$	$2+3z$	$\frac{\pi^2}{3} + \frac{7}{4}$
$T_R^{-1}C_g^{(1)FS}$	\mathcal{D}_1	\mathcal{D}_0	$\log(1-z)$	$\log z$	$P(z)$	$-\delta(1-z)$
$\overline{\text{MS}}$			$p_{qg}(z)$	$-p_{qg}(z)$	$-4p_{qg}(z) + 3$	
DIS						
AVERSA					$-4p_{qg}(z) + 3$	
KRK, KRKDY			$-p_{qg}(z)$		$-3p_{qg}(z) + 2$	
POS			$-p_{qg}(z)$		$-3p_{qg}(z) + 3$	
DPOS					$-3p_{qg}(z) + 3$	
MPOS			$-p_{qg}(z)$		$-3p_{qg}(z) + 3$	
PHYS				$-p_{qg}(z)$	$-3p_{qg}(z) + 2$	

Table 5: DIS coefficient functions for each factorisation scheme, in the notation of Eq. (33).

$C_F^{-1}D_{q\bar{q}}^{(1)FS}$	\mathcal{D}_1	\mathcal{D}_0	$\log(1-z)$	$\log z$	$P(z)$	$-\delta(1-z)$
$\overline{\text{MS}}$	8		$-4(1+z)$	$-2p_{qq}(z)$		$-\frac{2\pi^2}{3} + 8$
AVERSA	4	3	$-2(1+z)$		$-6-4z$	$-\frac{4\pi^2}{3} - 1$
DIS	4	3	$-2(1+z)$		$-6-4z$	$-\frac{4\pi^2}{3} - 1$
KRK					$-2+2z$	$-\frac{4\pi^2}{3} - \frac{1}{2}$
KRKDY					$-2+2z$	$-\frac{4\pi^2}{3} + \frac{5}{2}$
POS, DPOS	8		$-4(1+z)$	$-2p_{qq}(z)$		$-\frac{2\pi^2}{3} + 8$
MPOS	8		$-4(1+z)$	$-2p_{qq}(z)$	$-\frac{700}{3}z^2(1-z)^2$	$-\frac{2\pi^2}{3} + 8$
PHYS	4		$-2(1+z)$	$-2p_{qq}(z)$	$-2+2z$	$-\frac{2\pi^2}{3} + \frac{5}{2}$
$T_R^{-1}D_{gg}^{(1)FS}$	\mathcal{D}_1	\mathcal{D}_0	$\log(1-z)$	$\log z$	$P(z)$	$-\delta(1-z)$
$\overline{\text{MS}}$			$2p_{qg}(z)$	$-p_{qg}(z)$	$\frac{1}{2} + 3z - \frac{7}{2}z^2$	
AVERSA			$p_{qg}(z)$		$\frac{1}{2} + 3z - \frac{7}{2}z^2$	
DIS			$p_{qg}(z)$		$\frac{3}{2} - 5z + \frac{9}{2}z^2$	
KRK, KRKDY					$\frac{1}{2} + z - \frac{3}{2}z^2$	
DPOS			$p_{qg}(z)$		$\frac{3}{2} + z - \frac{3}{2}z^2$	
POS					$\frac{3}{2} + z - \frac{3}{2}z^2$	
MPOS					$\frac{3}{2} + z - \frac{3}{2}z^2$	
PHYS			$p_{qg}(z)$	$-p_{qg}(z)$	$\frac{1}{2} + z - \frac{3}{2}z^2$	

Table 6: Drell-Yan coefficient functions for each factorisation scheme, in the notation of Eq. (33).

$C_F^{-1}C_{gg}^{(1)\text{FS}}$	\mathcal{D}_1	\mathcal{D}_0	$\log(1-z)$	$\log z$	$P(z)$	$-\delta(1-z)$
$\overline{\text{MS}}$			$2p_{gq}(z)$	$-p_{gq}(z)$	$-\frac{3}{2}\frac{1}{z} + 3 - \frac{1}{2}z$	
AVERSA			$p_{gq}(z)$		$-\frac{3}{2}\frac{1}{z} + \frac{13}{3} - \frac{1}{2}z$	
Dis	2	$-\frac{3}{2}$	$2p_{gq}(z) - 1 - z$	$-p_{gq}(z) - p_{qq}(z)$	$-\frac{3}{2}\frac{1}{z} + 6 + \frac{3}{2}z$	$\frac{\pi^2}{3} + \frac{9}{2}$
KRK					$-\frac{3}{2}\frac{1}{z} + 3 - \frac{3}{2}z$	
Pos					$\frac{(z+1)^2}{2z} = \frac{1}{2}\frac{1}{z} + 1 + \frac{1}{2}z$	
MPOS					$\frac{1}{2}\frac{1}{z} + 1 + \frac{1}{2}z$	
PHYS			$p_{gq}(z)$	$-p_{gq}(z)$	$-\frac{3}{2}\frac{1}{z} + 3 - \frac{3}{2}z$	
$C_A^{-1}C_{gg}^{(1)\text{FS}}$	\mathcal{D}_1	\mathcal{D}_0	$\log(1-z)$	$\log z$	$P(z)$	$-\delta(1-z)$
$\overline{\text{MS}}$	8		$8\left(\frac{1}{z} - 2 + z(1-z)\right)$	$-4p_{gg}(z)$	$-\frac{11}{3}\frac{(1-z)^3}{z}$	$-\frac{2\pi^2}{3} - \frac{11}{3}$
AVERSA	4		$8\left(\frac{1}{z} - \frac{3}{2} + z(1-z)\right)$	$-4\left(\frac{1}{z} - 1 + z(1-z)\right)$	$-\frac{11}{3}\frac{(1-z)^3}{z}$	$-\frac{4\pi^2}{3} - \frac{17}{3} + \frac{5}{3}\frac{T_{R}^{nf}}{C_A}$
Dis	8		$8\left(\frac{1}{z} - 2 + z(1-z)\right) + 4\frac{T_{R}^{nf}}{C_A}p_{qg}(z)$	$-4p_{gg}(z) - 4\frac{T_{R}^{nf}}{C_A}p_{qq}(z)$	$-\frac{11}{3}\frac{(1-z)^3}{z} + 32\frac{T_{R}^{nf}}{C_A}z(1-z) - 4\frac{T_{R}^{nf}}{C_A}$	$-\frac{2\pi^2}{3} - \frac{11}{3}$
KRK					$-\frac{11}{3}\frac{(1-z)^3}{z}$	$-\frac{4\pi^2}{3} - \frac{473}{3} + \frac{59}{18}\frac{T_{R}^{nf}}{C_A}$
DPOS	8		$8\left(\frac{1}{z} - 2 + z(1-z)\right)$	$-4p_{gg}(z)$	$-\frac{11}{3}\frac{(1-z)^3}{z}$	$-\frac{2\pi^2}{3} - \frac{11}{3}$
Pos	8		$8\left(\frac{1}{z} - 2 + z(1-z)\right)$	$-4p_{gg}(z)$	$-\frac{11}{3}\frac{(1-z)^3}{z}$	$-\frac{2\pi^2}{3} - \frac{11}{3}$
MPOS	8		$8\left(\frac{1}{z} - 2 + z(1-z)\right)$	$-4p_{gg}(z)$	$-\frac{11}{3}\frac{(1-z)^3}{z} - \frac{950}{3}\frac{T_{R}^{nf}}{C_A}z^2(1-z)^2$	$-\frac{2\pi^2}{3} - \frac{11}{3}$
PHYS	4		$4\left(\frac{1}{z} - 2 + z(1-z)\right)$	$-4p_{gg}(z)$	$-\frac{11}{3}\frac{(1-z)^3}{z}$	$-\frac{2\pi^2}{3} - \frac{335}{3} + \frac{29}{18}\frac{T_{R}^{nf}}{C_A}$

Table 7: Higgs coefficient functions for each factorisation scheme, in the notation of Eq. (33).

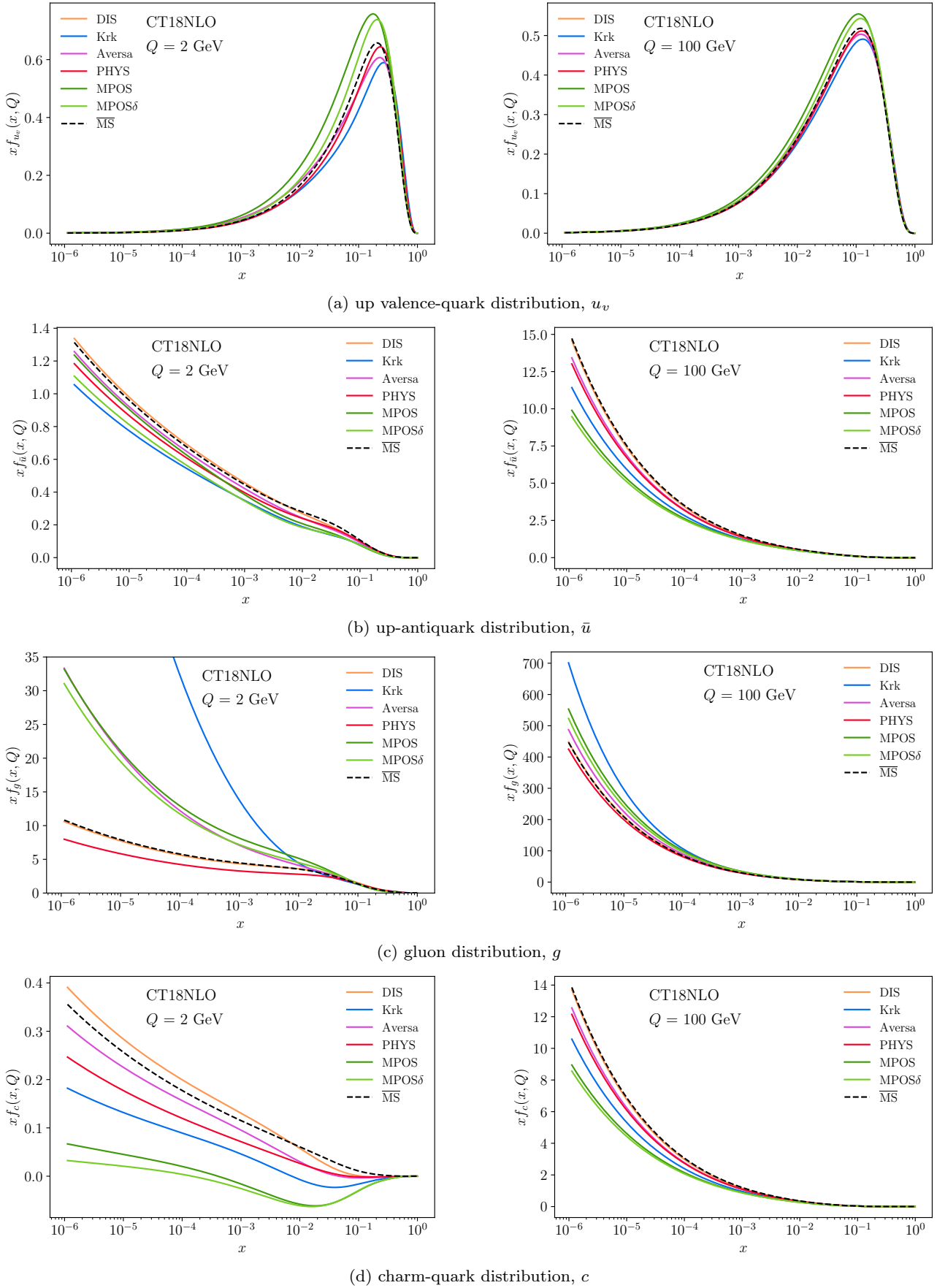


Fig. 1: Comparison of transformed CT18NLO PDFs in different schemes for u -valence, \bar{u} , gluon and charm, at $Q = 2$ GeV (left) and 100 GeV (right). The remaining flavours are presented in Fig. 16 in Appendix B.

some schemes is negative. This will be discussed further in Sec. 3.5. These features are however washed out by the evolution and at large scales, the charm PDF resembles the PDFs of the light sea quarks, cf. Fig. 1b.

For completeness, we provide the remaining flavours for the transformed CT18NLO PDFs in Fig. 16 in Appendix B. As a general comment, for all flavours, we observe that the differences between the schemes decline as the factorisation scale Q increases. This follows naturally from the fact that the PDF factorisation-scheme transformations of Eq. (5) modify the PDFs at $\mathcal{O}(\alpha_s)$, and $\alpha_s(Q)$ decreases by a factor of approximately 2.5 between $Q = 2$ GeV and $Q = 100$ GeV. This effect continues at higher scales, where the schemes converge.

In general, the observations summarised above for CT18NLO also hold for the NNPDF40MC and MSHT20nlo PDF sets, shown in Fig. 17 and Fig. 18 respectively. At high-scales, the differences between the discussed PDF-sets are modest. This is to be expected, as the DGLAP evolution ‘forgets’ initial conditions with the rising scale. However, at low- Q we observe several differences, especially prominent between MSHT20nlo and CT18NLO at $x \lesssim 10^{-4}$. These are particularly visible in the charm, gluon, and light sea distributions. In particular, for the MPOS, MPOS δ and KRK schemes, the MSHT20nlo charm PDF is decreasing rather than increasing as $x \rightarrow 0$, and becomes significantly negative. These features are driven by the much larger MSHT20nlo $\overline{\text{MS}}$ gluon distribution at scales close to the input scale $Q_0 \sim 1$ GeV (shown in Figs. 1c and 18c). The dependence of the transformed PDFs on the features of the input PDFs is discussed in further detail in Sec. 3.2.

3.2 Anatomy of transformed PDFs

We can look in more detail at how the PDFs in different schemes are assembled from the input PDFs by the transformation of Eq. (5).

To illuminate the effect of the different factorisation-scheme transformations on proton PDFs, we consider a simultaneous decomposition by flavour and by contribution type. Separating Eq. (5) into the contributions to each (output) flavour according to the input flavours we get, for quarks of flavour f ,

$$f_{q_f}^{\text{FS}}(x, \mu_F) = f_{q_f}^{\overline{\text{MS}}}(x, \mu_F) + \frac{\alpha_s}{2\pi} \left[K_{qg}^{\overline{\text{MS}} \rightarrow \text{FS}} \otimes f_g^{\overline{\text{MS}}} + K_{qq}^{\overline{\text{MS}} \rightarrow \text{FS}} \otimes f_{q_f}^{\overline{\text{MS}}} \right], \quad (36)$$

and for the gluon,

$$f_g^{\text{FS}}(x, \mu_F) = f_g^{\overline{\text{MS}}}(x, \mu_F) + \frac{\alpha_s}{2\pi} \left[K_{gg}^{\overline{\text{MS}} \rightarrow \text{FS}} \otimes f_g^{\overline{\text{MS}}} + K_{gq}^{\overline{\text{MS}} \rightarrow \text{FS}} \otimes \sum_f (f_{q_f}^{\overline{\text{MS}}} + f_{\bar{q}_f}^{\overline{\text{MS}}}) \right]. \quad (37)$$

In Figs. 2 to 5 we show a decomposition of the transformed PDFs based on the terms from Tables 1 to 4. To simplify the plots, the terms of the decomposition of Eq. (33) used in Tables 1 to 4 are recombined according to their asymptotic behaviour as $z \rightarrow 0, 1$:

$$K(z) = \sum_{k=0}^1 a_k \mathcal{D}_k(z) + b(z) \log(1-z) \quad \cdots \cdots \quad (38) \\ + c(z) \log z + P(z) \quad \text{---} \text{---} \text{---} \\ - \Delta \delta(1-z) \quad \cdots \cdots \cdots$$

The leading-order contribution to the transformed PDF is simply the input $\overline{\text{MS}}$ PDF itself (from Eq. (6)), and is plotted separately, either as a solid grey line, or combined with the NLO δ -function contribution as

$$\left(1 - \frac{\alpha_s}{2\pi} \Delta\right) \delta(1-z). \quad \cdots \text{---} \text{---} \quad (39)$$

This combination is shown separately to demonstrate that in many cases the LO term in Eqs. (36) and (37) is mostly cancelled by the $\delta(1-z)$ terms responsible for momentum conservation.

To see more clearly how the new PDFs are built, in each plot, the contributions to the transformed PDF are plotted in aggregate (left-hand panel), as well as decomposed according to those from input quark-type PDFs (central panel), and the input gluon PDF (right-hand panel).

For quark PDFs, the only quark-type contribution is from the corresponding $\overline{\text{MS}}$ PDF of the same flavour, while for gluon PDFs the quark-type contribution is that of the transformed quark singlet PDF. In each panel, the relevant contributions are again decomposed according to Eqs. (38) and (39).

The sum of contributions from each kernel is plotted in black, both to give the total NLO contribution arising from each input flavour (central/right-hand panels), and to give the total overall PDF (left-hand panel).¹¹

¹¹Note that in order to obtain the full transformed ‘output’ PDF (black line in left-hand panel), we can either sum all the curves from the left-hand panel apart from the blue one (which is a combination of green and grey), or sum the combined NLO contributions from input quarks (black line in central panel) and gluons (black line in right-hand panel) together with the LO contribution from the input $\overline{\text{MS}}$ PDF (grey line in left-hand panel).

3.2.1 Valence quark PDFs

In Fig. 2 we show the decomposition of the transformed up-quark valence PDF u_v ,

$$f_{u_v}(x, Q) = f_u(x, Q) - f_{\bar{u}}(x, Q), \quad (40)$$

in the KRK (1st row), MPOS (2nd row), and PHYS (3rd row) schemes at factorisation scale $\mu = 2$ GeV. The remaining schemes are presented in Fig. 19 in Appendix C. The same transformed u_v PDFs were previously shown in Fig. 1a, using a linear scale for the y -axis.

It follows from Eq. (36) that for quark valence PDFs the contribution from the gluon cancels,

$$f_{u_v}^{\text{FS}}(x, \mu_F) = f_{u_v}^{\overline{\text{MS}}}(x, \mu_F) + \frac{\alpha_s}{2\pi} \left[K_{qq}^{\overline{\text{MS}} \rightarrow \text{FS}} \otimes f_{u_v}^{\overline{\text{MS}}} \right]. \quad (41)$$

The gluon contribution to the valence quark distribution can indeed be seen to be zero in the right-hand panels of Figs. 2 and 19.

As is expected from a perturbative transformation, in all schemes the dominant contribution to the total PDF (black line in left-hand panel) is given by the leading order (input) $\overline{\text{MS}}$ contribution (grey line). This remains true at higher scales and for the schemes not shown here (see Appendix C). The net NLO contribution to the transformed PDF is visible as the black line in the central panels.

For the KRK, DIS and AVERSA schemes there is a large cancellation between the input $\overline{\text{MS}}$ distribution (the LO contribution to the transformed PDF) and the NLO $\delta(1-z)$ contribution (compare blue and grey lines in the decomposition figures). This is responsible in part for the vertical shifts in the valence peak visible in Figs. 1a and 16a, and can be attributed to the large $\delta(1-z)$ coefficients in Table 1.¹² The $\delta(1-z)$ terms also dominate the vertical shift in other schemes where they are partially mitigated by the positive contribution from the \mathcal{D}_k distribution and $\log(1-z)$ -terms. MPOS δ is the only scheme with opposite (positive) sign of $\delta(1-z)$ coefficient which causes the upwards vertical shift of the valence peak visible in Fig. 1a. For the MPOS scheme, the $P(z)$ contribution fulfils the same role of restoring momentum-conservation and shifts the peak in the same upward vertical direction, but the shape-effect of the soft-function shifts the valence peak towards lower x (this will be further discussed in Sec. 3.3.2).

For the AVERSA, DIS, PHYS, and KRK schemes the convolution with the \mathcal{D}_k distribution and $\log(1-z)$ terms shifts the valence peak horizontally to higher x

values, and is the dominant NLO contribution at high- x (red line in central panel). This shift is largest for the KRK scheme due to the distribution contribution (coefficients a_1 and b) being exactly twice as large as for the PHYS and AVERSA/DIS schemes.

The difference in $c(z) \log z + P(z)$ between PHYS and KRK schemes is driven by the absence of the $-p_{qq}(z) \log z$ contribution cf. Table 1; this has a noticeable shape effect at large- x . The effect of the specific choice of $P(z)$ is significant and can be seen comparing the KRK scheme shown in Fig. 2 to AVERSA/DIS, shown in Fig. 19 (yellow lines).

At $Q = 100$ GeV the contributions and conclusions are very similar (see Fig. 23).

In this section we focused on u -valence PDFs, but similar observations hold for d -valence PDFs (Fig. 16a).

3.2.2 Sea quark PDFs

In Fig. 3 we show the decomposition of the transformed \bar{u} PDFs; the remaining schemes are shown in Fig. 20. Unlike the valence-quark PDFs, this receives contributions from the $\overline{\text{MS}}$ gluon PDF through the qg kernel, in addition to those from the $\overline{\text{MS}}$ \bar{u} PDF through the $q\bar{q}$ kernel.

At high- x , the contributions from the gluon are dominated by the $\log(1-z)$ contribution (red line in the right panel), which is negative, and is either equal to $p_{qg}(z) \log(1-z)$ (AVERSA, DIS, PHYS) or $2p_{qg}(z) \log(1-z)$ (KRK, MPOS, MPOS δ) as shown in Table 2; the gluon contribution to the transformed PDFs is therefore qualitatively very similar. At low- x , the $-p_{qg}(z) \log z$ contribution common to all schemes is positive and can be seen directly in the AVERSA scheme plot in Fig. 20 (yellow line in right panel). With the exception of the AVERSA scheme (for which $P(z) \equiv 0$) there is a common $-p_{qg}(z)$ contribution to $P(z)$ in all schemes (scaled by a factor of 4 for DIS). This is negative and largely cancels with the $-p_{qg}(z) \log z$ contribution to give a residual (smaller) negative contribution (visible in the MPOS and MPOS δ schemes). This reduction in magnitude leads the overall contribution from the gluon PDF (black line in right panel) to closely match the $\log(1-z)$ contribution for MPOS/MPOS δ . The addition of 1 in $P(z) = -p_{qg}(z) + 1$ in the KRK and PHYS schemes is sufficient to turn the $P(z)$ and $P(z) + c(z) \log z$ contributions positive (visible in the PHYS and KRK schemes respectively; yellow line in right panel).

The contributions from the input sea-quark PDFs are qualitatively similar for the KRK, PHYS, AVERSA and DIS schemes (see Table 1 and black line in the middle panel of Figs. 3 and 20). The MPOS-type schemes are off-diagonal transformations (K_{qg} vanishes), apart

¹²Note the minus-sign in the heading of the $\delta(1-z)$ column (equivalently in front of Δ in Eq. (33)).

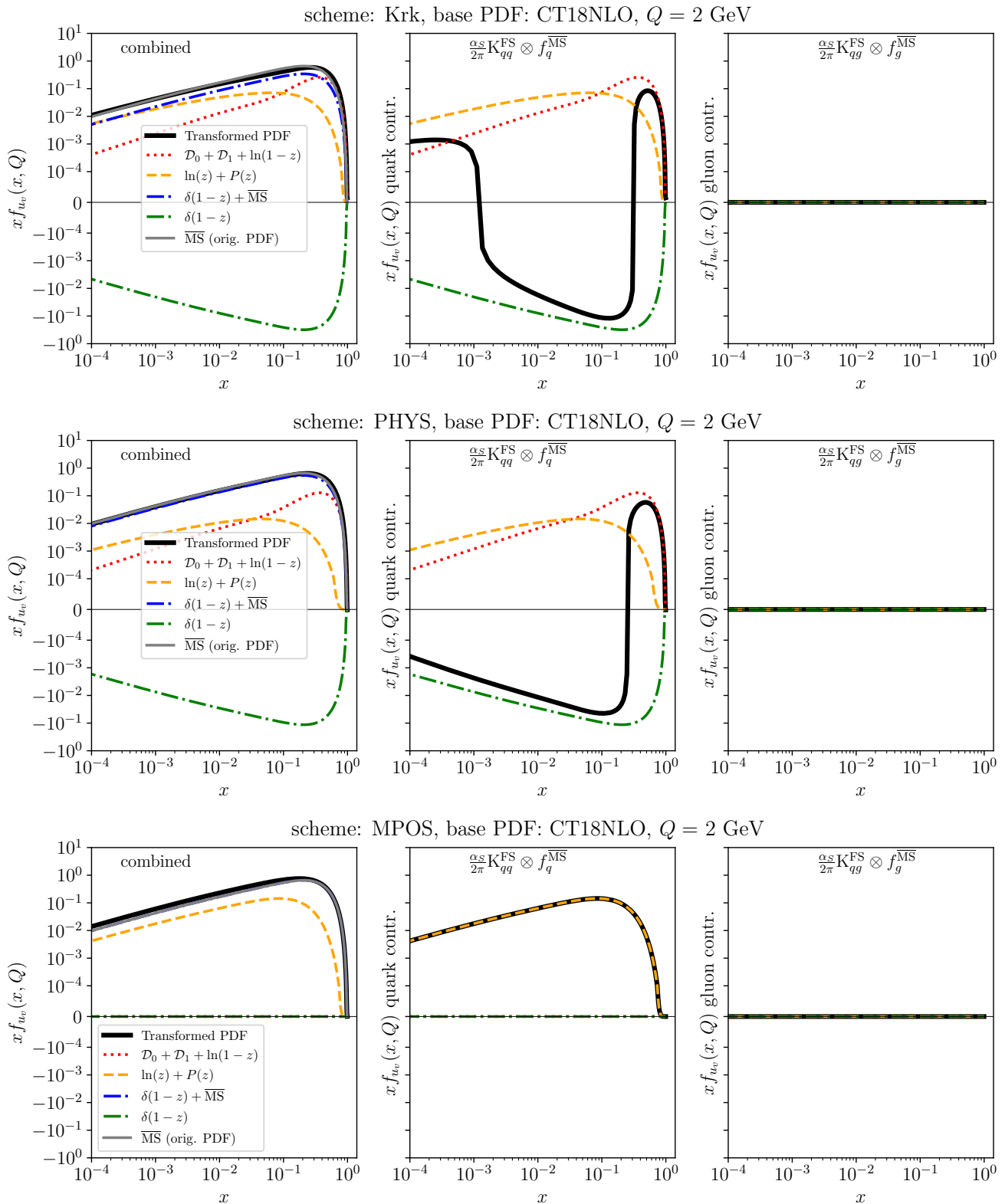


Fig. 2: Decomposition of transformed u_v -quark PDF in the KRK, MPOS, and PHYS schemes at factorisation scale $Q = 2$ GeV, as described in Sec. 3.2.

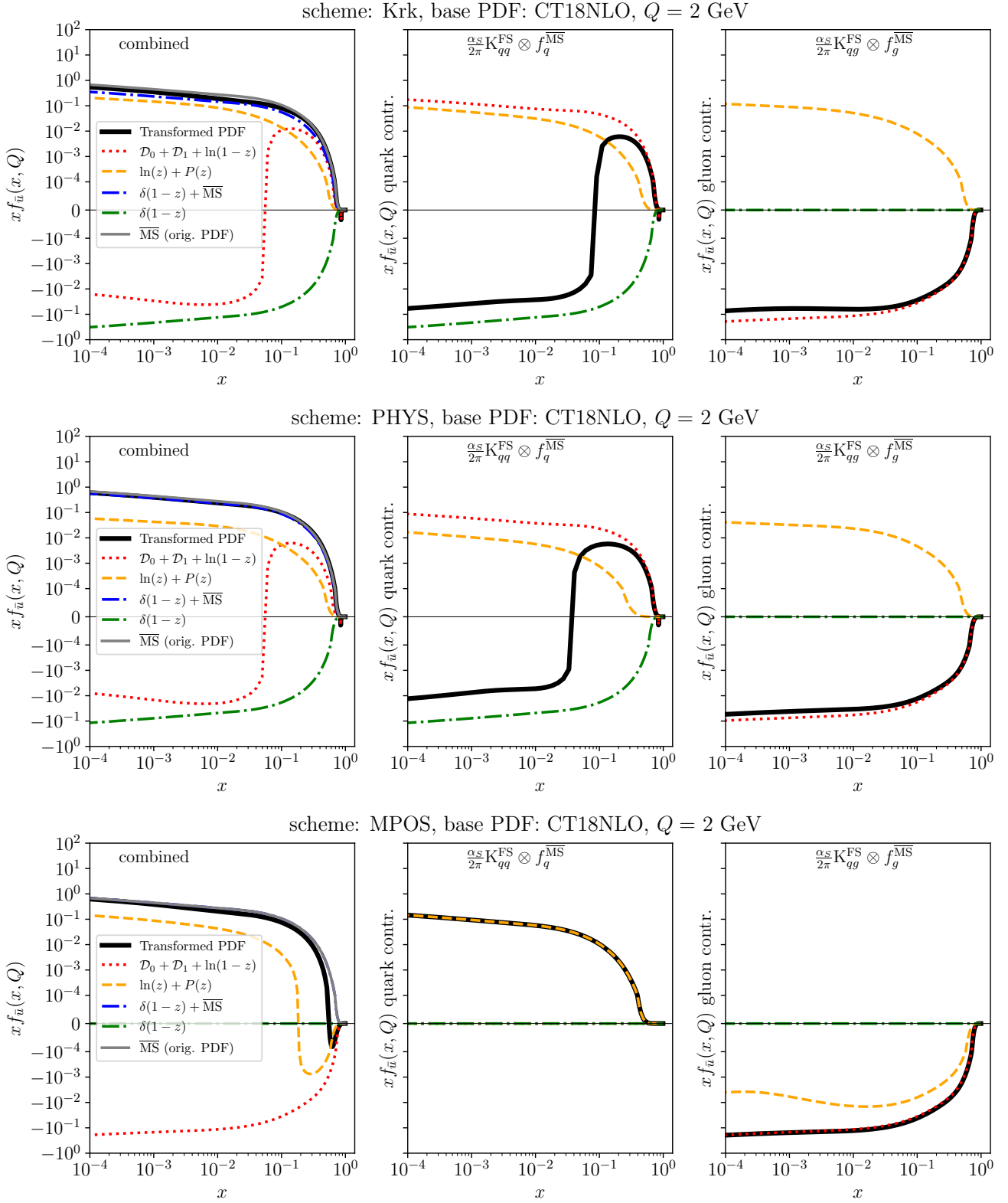


Fig. 3: Decomposition of transformed u -antiquark PDF in the KRK, MPOS, and PHYS schemes at factorisation scale $Q = 2$ GeV, as described in Sec. 3.2.

from the terms responsible for momentum-conservation via a soft function or $\delta(1-z)$. At high- x , the quark contributions are governed by the \mathcal{D}_k distribution terms as well as by the large $\delta(1-z)$ term in the case of AVERSA/DIS/KRK; \mathcal{D}_0 can be seen to contribute a characteristic bump in AVERSA/DIS. At low- x , there is a large cancellation between the sum of contributions from the $\mathcal{D}_k + \log(1-z)$ and polynomial terms (red and yellow lines) which are positive and the negative delta-function contributions (green line). The net effect of the qq -kernels at low- x is an overall-negative contribution, which for the AVERSA, KRK, PHYS schemes is similar in magnitude and direction to that of the qg -kernels, leading to the overall suppression visible in Fig. 1b.

At $Q = 100$ GeV (see Fig. 24) the individual contributions are qualitatively similar, especially from the input sea-quark, but the negative off-diagonal contribution from the gluon is much larger due to the growth of the gluon PDF. This contribution grows faster than the reduction in α_s leading to the larger relative spread of transformed PDFs than at $Q = 2$ GeV, visible in Figs. 1b and 24.

In this section we focused on the \bar{u} PDF; similar observations hold for the remaining sea-quark flavours (see also Figs. 16c and 16d).

3.2.3 Gluon PDFs

We show the decomposition of the transformed gluon PDFs in in Fig. 4; the remaining schemes are shown in Fig. 21.

At low- x , the NLO contribution becomes comparable in magnitude to LO for the KRK, MPOS, AVERSA and MPOS δ schemes (compare grey and black lines in the left panel), indicating a breakdown of perturbation theory. This is not the case for the DIS or PHYS schemes. The behaviour at low- x may be seen to be dominated by the $\log z$ contribution of Tables 3 and 4 (i.e. the choice of $c(z)$ in Eq. (33)). The DIS scheme behaves markedly different in this respect due to the appearance of the $p_{qq}(z)$ splitting function in the K_{gq}^{DIS} kernel in Table 3;¹³ other schemes have either $c(z) \equiv 0$ (PHYS), or $c(z) = p_{qq}(z)$ (all other schemes). In the flavour-diagonal contribution from the input-gluon PDF, the large difference between the KRK scheme and the others, evident in Fig. 1c, can be traced back to the $c(z) = -2p_{gg}(z)$ coefficient of $\log z$ in K_{gg}^{KRK} (Table 4), which contributes a divergent low- z term proportional to $\log(z)/z$.

At large- x the shape is governed by the distribution terms \mathcal{D}_k , where present. For the K_{gg} kernels, this

contribution (red line) is exactly twice as large for the KRK scheme as for PHYS, and approximately twice as large as for AVERSA. For the K_{gq} kernels, the only non-zero contribution relevant at high- x is proportional to $p_{gq}(z) \log(1-z)$ with coefficient C_F (AVERSA, PHYS) or $2C_F$ (KRK, POS-type), with the exception of the DIS scheme which uniquely contains $\mathcal{D}_{0,1}$ terms originating from the C_q DIS coefficient function.¹³ This leads to a region of negativity for $x \gtrsim 0.55$.

At $Q = 100$ GeV (shown in Figs. 4 and 25) the effect of the contributions is qualitatively similar, but reduced in magnitude; only the KRK scheme PDF is shifted significantly from the leading-order contribution given by the input $\overline{\text{MS}}$ PDF, due again to the $\log(z)/z$ contribution.

3.2.4 Heavy quark PDFs

In this section we use the example of charm-quark PDF to examine how heavy-quark PDFs are constructed in the different schemes. As discussed in Sec. 2.1.5, since modern PDFs use variable-flavour-number schemes (VFNS), heavy-quark PDFs are non-zero only above the flavour thresholds, at scales $\mu_f \gtrsim m_f$. The behaviour at these thresholds will be discussed here and also later in Sec. 3.5.

As before, we show the decomposition of the transformed charm-quark PDF at $\mu = 2$ GeV for the KRK, MPOS, and PHYS schemes in Fig. 5, and for the remaining schemes in Fig. 22 in Appendix C. These can be also compared with Fig. 1d showing the transformed charm PDFs (using a linear scale for the y -axis).

Relative to the sea-quark PDFs previously discussed in Sec. 3.2.2, the contributions from the input gluon PDF are identical, while the contributions from the input heavy quark PDF are suppressed by approximately an order of magnitude, due to the proximity to the flavour threshold.

At high- x , all of the schemes exhibit negativity (see black line in the left panels). This is driven by the $\log(1-z)$ terms within the K_{gq} kernels of Table 2 (red line in right panels). The coefficient of these terms in the KRK and POS-type schemes is double that of the others. In the KRK and PHYS schemes, this negative contribution is partially mitigated with respect to the POS-type schemes by the inclusion of +1 in the $P(z)$ contribution (see yellow line in right-hand panels). This generates a positive contribution from the gluon input PDF which is of a similar order of magnitude to (though smaller than) the negative contribution from the $\log(1-z)$ terms. For the MPOS scheme the $P(z)$ contribution is itself negative and suppressed by an order of magnitude, so provides no such mitigation. As a result the region of negativity for the MPOS scheme

¹³ This is due to the way momentum conservation is enforced in the DIS scheme, Eq. (32).

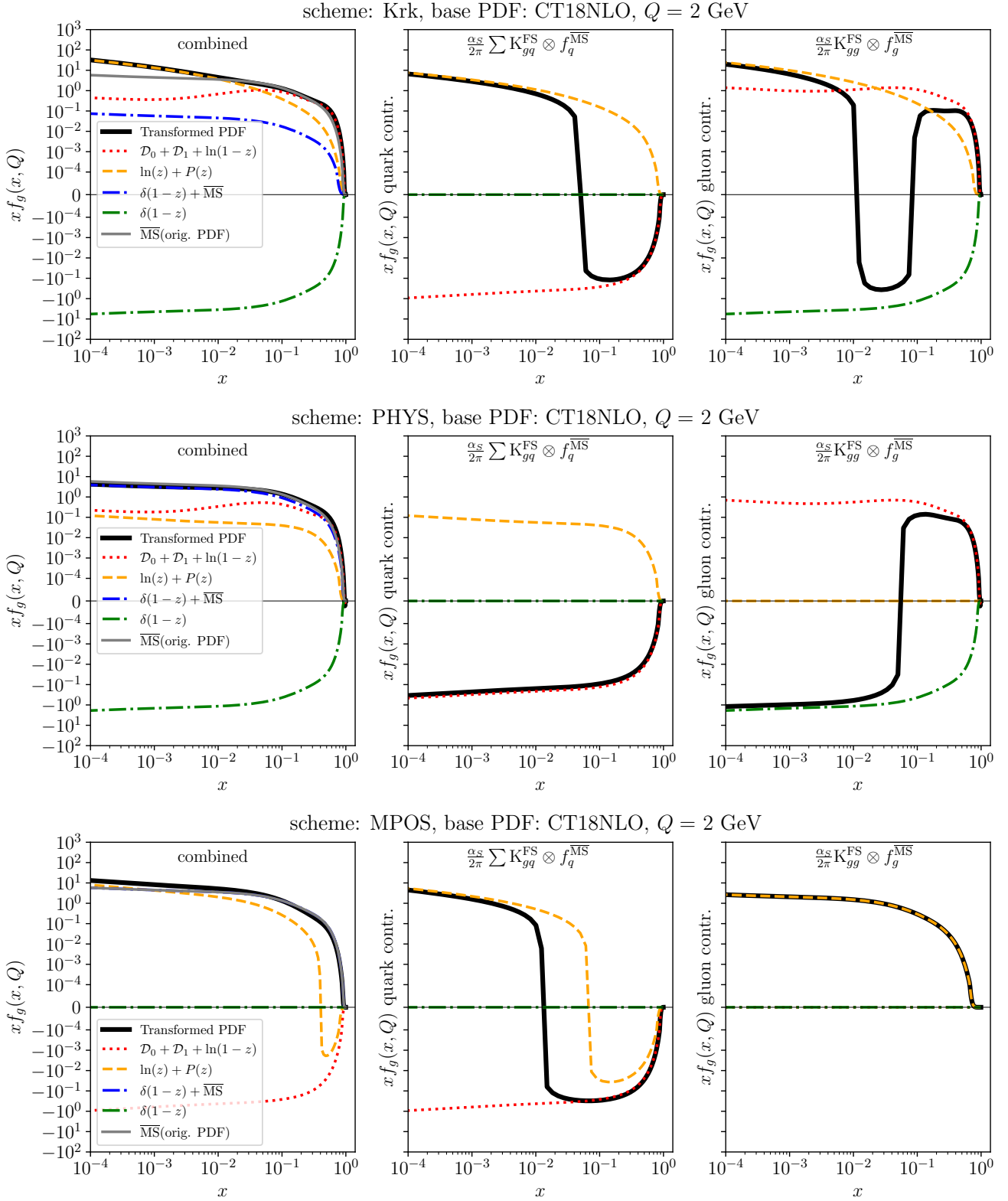


Fig. 4: Decomposition of transformed gluon PDF in the KRK, MPOS, and PHYS schemes at factorisation scale $Q = 2$ GeV, as described in Sec. 3.2.

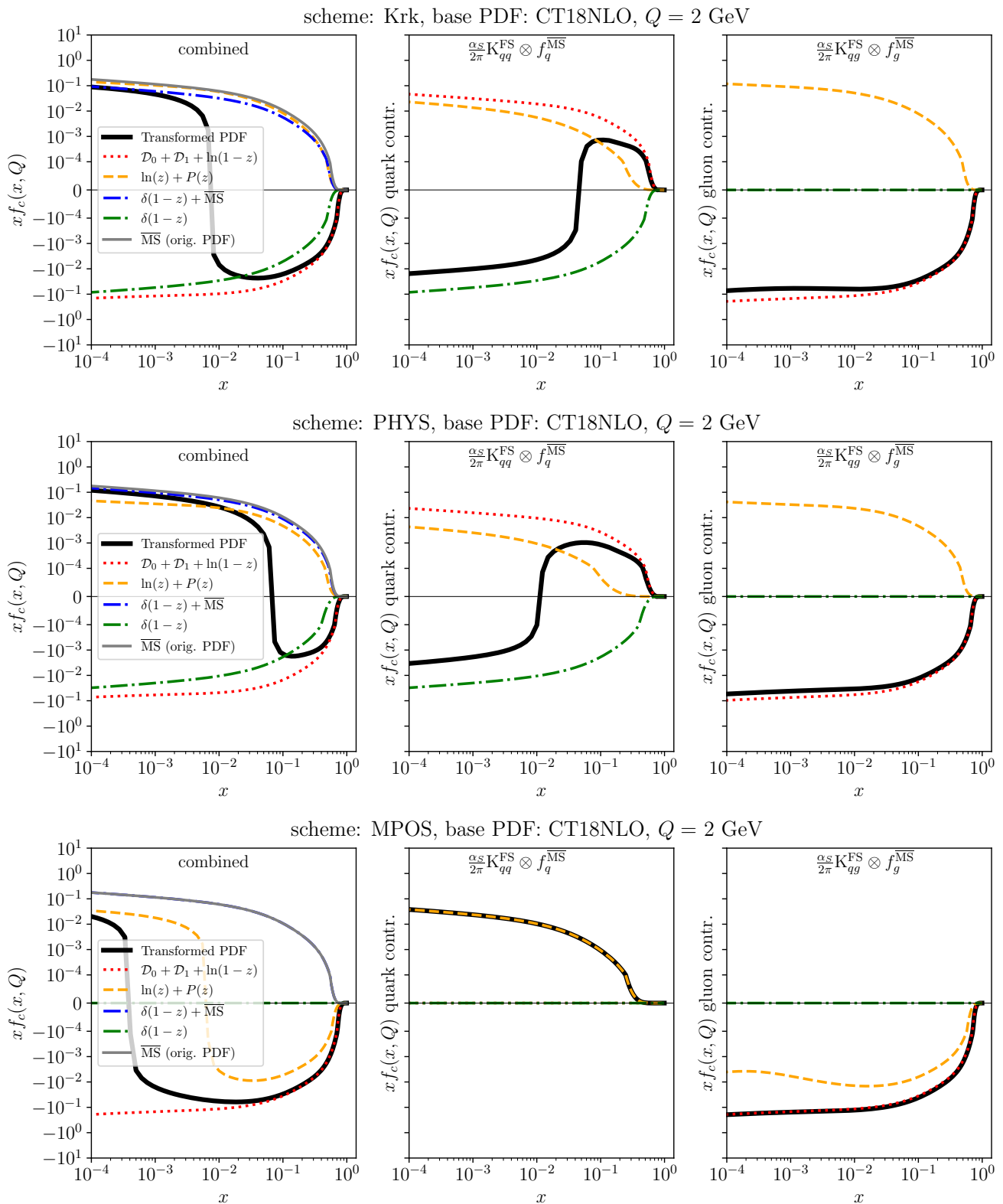


Fig. 5: Decomposition of transformed charm-quark PDF in the KRK, MPOS, and PHYS schemes at factorisation scale $Q = 2$ GeV, as described in Sec. 3.2.

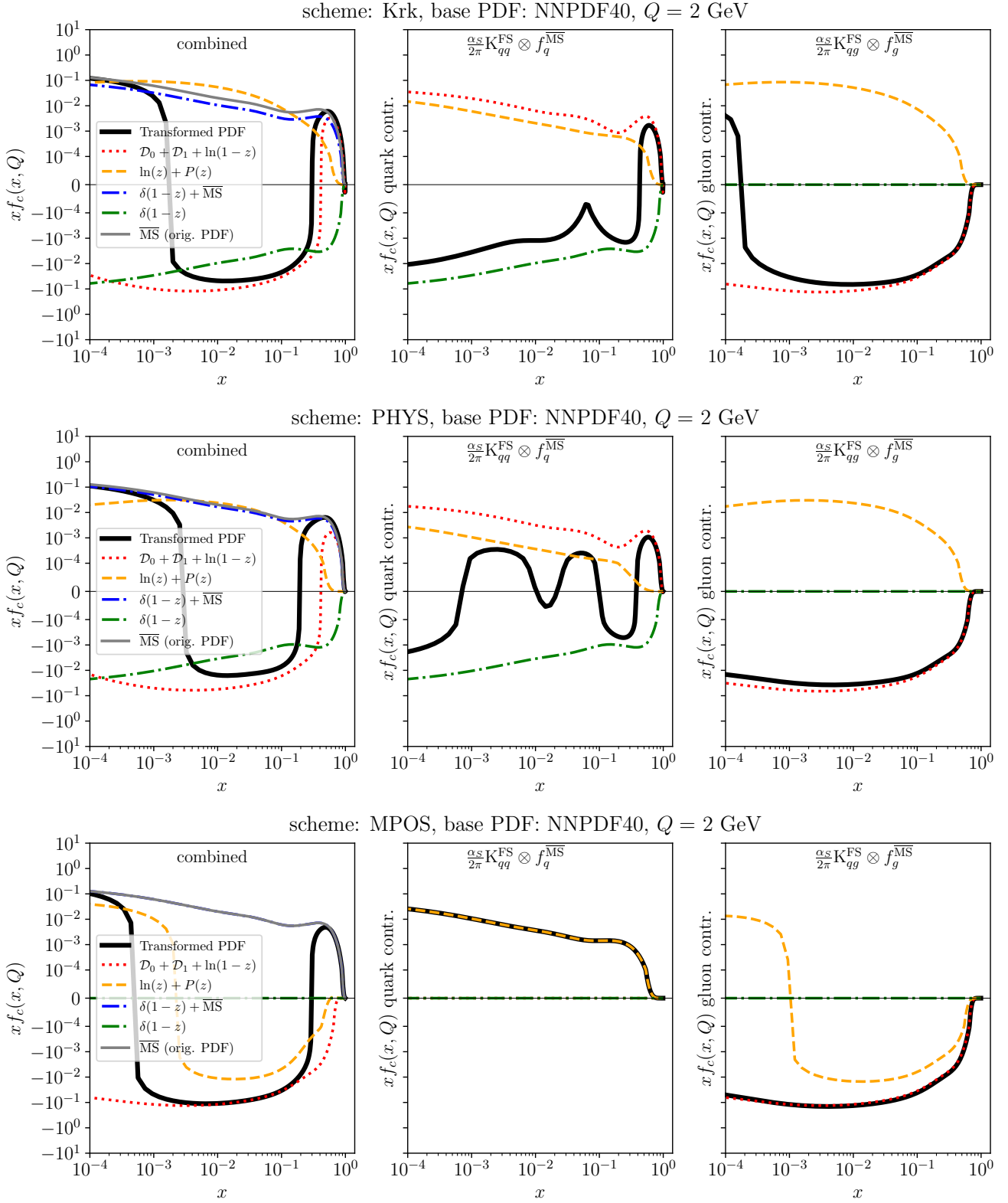


Fig. 6: Decomposition of transformed charm-quark PDF in the KRK, MPOS, and PHYS schemes at factorisation scale $Q = 2$ GeV, as described in Sec. 3.2, based on NNPDF40 $\overline{\text{MS}}$ PDFs. Note that in contrast with Fig. 5, the NNPDF40 PDF set includes an intrinsic charm contribution.

stretches an order of magnitude further than for the KRK scheme, to $x \gtrsim 4 \cdot 10^{-4}$.

At low- x , the leading-order contribution dominates except for the MPOS-type schemes and, to a lesser extent, the KRK scheme, due to the large negative contributions summarised above.

At $Q = 100$ GeV, the transformed c -quark PDF resembles that of the sea-quarks (see Figs. 1 and 26).

In Fig. 6 we show the same decomposition plots as in Fig. 5 using the NNPDF40 PDF set, which includes an intrinsic charm-quark contribution. The intrinsic contribution restores positivity at high- x through the distribution contributions, while the negativity at intermediate- x persists.

The negativity of the heavy-quark PDFs is discussed further in Sec. 3.5.

3.3 Momentum sum-rule

As discussed in Sec. 2.1.4, PDFs in the $\overline{\text{MS}}$ scheme are constrained to satisfy the momentum sum-rule of Eq. (24), for all factorisation-scales μ ; that is, the average momentum fractions carried by each parton must sum to 1 (the total momentum fraction of the hadron; here, proton).

To compare factorisation schemes on a like-for-like basis, this has been imposed by the modification of the Δ coefficient in Tables 1 to 4 according to Eq. (26), to satisfy momentum conservation at the level of the transformation kernels Eq. (25). The situation is different for MPOS where it is imposed through a ‘soft-function’ rather than a δ -function, and for DPOS and POS where the sum rule is not fulfilled.

In this section, we directly test the sum rule of the transformed PDFs in Sec. 3.3.1, and compare the different methods for imposing it, focusing on the MPOS and MPOS δ schemes, in Sec. 3.3.2.

3.3.1 Numerical momentum conservation

In Fig. 7 we show the total momentum carried by all active flavours as a function of factorisation scale, i.e. we evaluate numerically the left-hand-side of Eq. (24) and compare it to 1. In addition to being of theoretical interest, this is a test of the numerical accuracy of the implemented PDF transformations and convolutions. We also compare it to the results for the input $\overline{\text{MS}}$ CT18NLO PDF set [56].

In Fig. 7a we show the schemes for which momentum conservation is imposed on the kernels. We find that the modifications restore the sum-rule to well within the target LHAPDF interpolation accuracy (10^{-3}); for

the MPOS and DIS schemes the deviation is approximately 10^{-6} .

In Fig. 7b we show the effect of the POS and DPOS transformations on the momentum sum-rule; that is, for the schemes in which momentum conservation is not explicitly imposed. We can deduce the magnitude of the required momentum-conservation-restoring terms from the deviations shown here. We see that for the POS scheme, the deviation from the sum-rule is approximately 20% at the input-scale $Q_0 \sim 1$ GeV, reducing to approximately 5% at high scales. For the DPOS scheme, the sensitivity of the sum-rule to the scale is smaller but qualitatively has the same relationship with scale, reducing from approximately 6% to approximately 2%.

3.3.2 Alternative methods for imposing momentum conservation

In Fig. 8 we illustrate the momentum sum-rule graphically: the left-hand-side of Eq. (24) corresponds to the shaded area, divided into valence quarks (purple), sea quarks (red), and gluons (blue).

Fig. 8a shows the effect of the strengthened momentum sum-rule of Eq. (32) used to define the DIS-scheme gluon PDF. As a direct consequence, the overall distribution of constituent momentum fractions (top line/total shaded area) is unchanged despite the relative momentum fractions changing under the scheme-transformation.

The MPOS and MPOS δ schemes differ only in their method for restoring the momentum sum-rule; this is an arbitrary choice, by convention imposed by modifying Δ as in Eq. (26). Imposing momentum-conservation then induces a modification of only the virtual contribution to the coefficient function. Any other function normalised with respect to the second Mellin moment,

$$\mathcal{M}[f^{\text{MOM}}](2) \equiv \int_0^1 dz z^1 f^{\text{MOM}}(z) = 1, \quad (42)$$

may be used with the same coefficient.

In [15] a ‘soft-function’ was chosen, a quartic polynomial vanishing in the $z \rightarrow 0, 1$ limits, and normalised to satisfy $\mathcal{M}[f](2) = 1$,

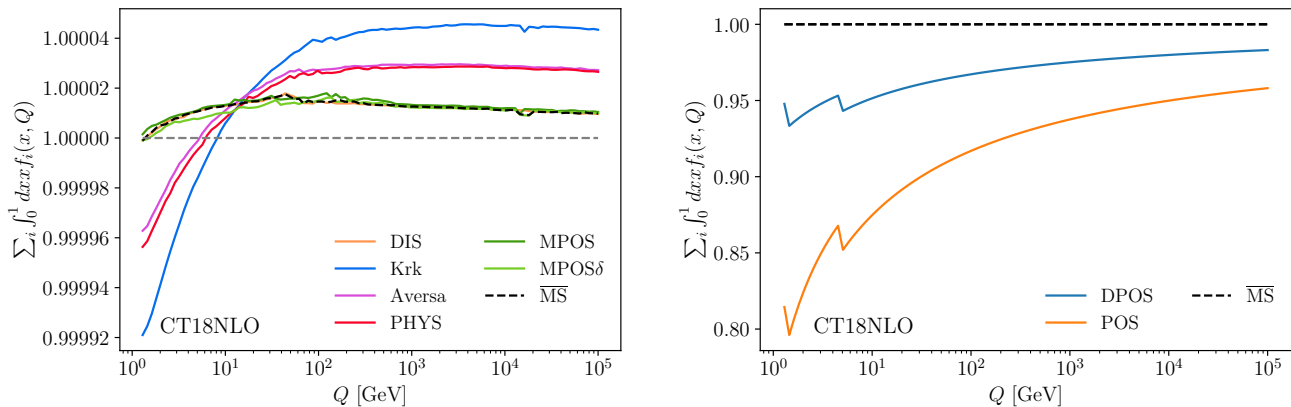
$$f^{\text{MOM}}(z) = 60 z^2 (1-z)^2, \quad (43)$$

for the MPOS scheme.¹⁴

¹⁴This is a special case of a two-parameter family of possible such choices,

$$f^{(m,n)\text{MOM}}(z) = \frac{(m+n)!}{m!(n-1)!} z^{m-1} (1-z)^{n-1}, \quad (44)$$

with $m = n = 3$.



(a) Factorisation schemes for which momentum-conservation is imposed.

(b) Pos-type schemes without momentum-conservation imposed.

Fig. 7: Numerical calculation of the momentum sum-rule, Eq. (24), as a function of the factorisation scale Q , for CT18NLO PDFs transformed into the considered factorisation schemes.

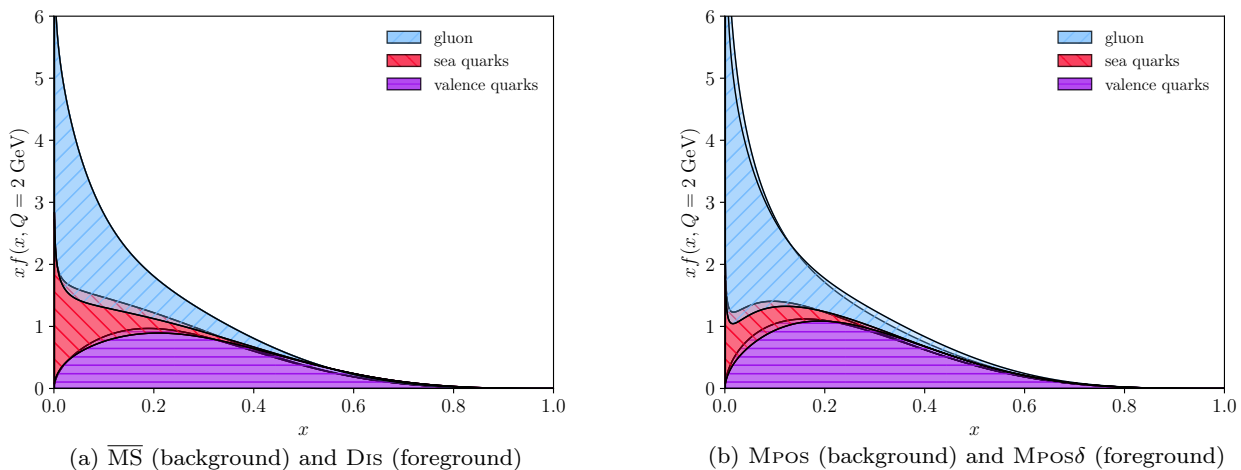
(a) $\overline{\text{MS}}$ (background) and DIS (foreground)(b) MPOS (background) and MPOS δ (foreground)

Fig. 8: Graphical illustration of the momentum sum-rule; carried momentum here corresponds to shaded area. The momentum sum-rule Eq. (24) implies that the total shaded area is 1.

Here, for MPOS and MPOS δ , we compare the effect of the respective choices. As can be seen from Tables 1 to 4, the off-diagonal kernels are identical in both schemes, while the diagonal kernels are non-zero only due to the inclusion of the momentum-conservation-restoring terms. As a result, the schemes differ only in the quark (input) contribution to the quark (output) PDF, and the gluon (input) contribution to the gluon (output) PDF. These are illustrated in Figs. 2 to 5 for the MPOS scheme, and in Figs. 19 to 22 for the MPOS δ scheme.

The MPOS and MPOS δ schemes are compared in Fig. 8b, illustrating the effect on the partonic momentum-fraction distributions of the choice of delta- or soft-function. We see that the choice has an effect both on

the overall distribution of constituent momentum fractions within the proton, with MPOS shifting the overall distribution lower in x , and on the relative momentum fractions of each flavour.

The change in the valence-quark distributions is entirely due to the flavour-diagonal kernels, which in the MPOS and MPOS δ schemes are entirely determined by the chosen momentum-conservation method. For MPOS and MPOS δ this has a positive coefficient, so increases the fractional composition of valence quarks relative to sea quarks.

The sea-quark distributions are also affected by the off-diagonal qg kernels; as a consequence, within the overall distribution, the MPOS and MPOS δ gluon PDFs take momentum directly from the sea quarks at low- x ,

significantly changing the qualitative shape of the overall quark distribution within the proton (cf. Fig. 8a). As a consequence the expected fraction of the proton's momentum carried by the valence quarks relative to sea quarks is seen to be sensitive to the choice of factorisation scheme.

3.4 Number sum-rules

In the $\overline{\text{MS}}$ scheme we know that the valence-quark number sum rules are fulfilled in the following way:

$$\int_0^1 dx \left[f_q^{\overline{\text{MS}}}(x; \mu_F) - f_{\bar{q}}^{\overline{\text{MS}}}(x; \mu_F) \right] = N_q^{\overline{\text{MS}}}, \quad (45)$$

where $N_q^{\overline{\text{MS}}} = \{2, 1, 0\}$ for u , d , and any other quark flavour (assuming there is no asymmetric intrinsic contributions, e.g. for charm). There is however, no guarantee that the same sum rule holds in a different factorisation scheme. In an alternative factorisation scheme, the same integral can be computed to give

$$\begin{aligned} N_q^{\text{FS}} &= \int_0^1 dx \left[f_q^{\text{FS}}(x; \mu_F) - f_{\bar{q}}^{\text{FS}}(x; \mu_F) \right] \\ &= \int_0^1 dx \left[f_q^{\overline{\text{MS}}}(x; \mu_F) - f_{\bar{q}}^{\overline{\text{MS}}}(x; \mu_F) \right. \\ &\quad + \frac{\alpha_s(\mu)}{2\pi} \sum_b \int_x^1 \frac{dz}{z} K_{qb}^{\overline{\text{MS}} \rightarrow \text{FS}}(z) f_b^{\overline{\text{MS}}}\left(\frac{x}{z}; \mu_F\right) \\ &\quad \left. - \frac{\alpha_s(\mu)}{2\pi} \sum_b \int_x^1 \frac{dz}{z} K_{\bar{q}b}^{\overline{\text{MS}} \rightarrow \text{FS}}(z) f_b^{\overline{\text{MS}}}\left(\frac{x}{z}; \mu_F\right) \right]. \end{aligned} \quad (46)$$

Using the definitions and properties of the kernels $K_{ab}^{\overline{\text{MS}} \rightarrow \text{FS}}$ and performing some algebra we get:

$$N_q^{\text{FS}} = N_q^{\overline{\text{MS}}} \left\{ 1 + \frac{\alpha_s(\mu)}{2\pi} \int_0^1 dz K_{qq}^{\overline{\text{MS}} \rightarrow \text{FS}}(z) \right\}. \quad (47)$$

This means that the number sum rule is modified when changing the scheme by terms of order $\mathcal{O}(\alpha_s)$. Note that it will not be altered relative to the $\overline{\text{MS}}$ scheme (at $\mathcal{O}(\alpha_s)$) if K_{qq} integrates to 0, including when K_{qq} is given by a plus distribution. This is the case, e.g. for the DIS scheme.

Since the modification is proportional to $\alpha_s(\mu)$, the sum-rule integral is in general scale-dependent (unless the $\mathcal{O}(\alpha_s)$ correction vanishes).

We can compute this change analytically which is given by the integral of K_{qq} kernel, see Table 8. At NLO the modification will only affect u and d quarks for which, in Fig. 9, we show the numerical value of the number sum rule for selected schemes. We can clearly see the deviation from the $\overline{\text{MS}}$ result, as well as the scale-dependence. In Fig. 9 we also compare the values

of Eq. (47) with those obtained directly from CT18NLO PDFs transformed into the different schemes, and see perfect agreement.

We should note that the modified form of the number sum rules for different factorisation schemes does not make them ‘less physical’ than the $\overline{\text{MS}}$ scheme or the DIS scheme for which the usual sum rules are fulfilled. The values of the sum rules are perturbative quantities which receive corrections at each perturbative order. A special property of the $\overline{\text{MS}}$ scheme is that these corrections are zero [59, 60].

This can have practical consequences for the determination of PDFs in phenomenological fits to data. In the $\overline{\text{MS}}$ or DIS scheme, in which the value of the sum-rule integral is constant, the usual practice is to enforce the sum rules during the fit. Alternatively, one can allow the fitting process to extract them from the data, and use the consistency of the sum-rules with their expected values as a test of the quality of the fit.¹⁵ Although it would be possible to impose the modified sum-rules as constraints on phenomenological fits of PDFs to data in alternative factorisation schemes with $N_q^{\text{FS}} \neq N_q^{\overline{\text{MS}}}$ in which the value is scale-dependent, a more natural approach might be to leave the PDFs unconstrained and use the sum-rules as a test of the consistency of the extracted PDFs with their expected properties.

3.5 Positivity

Phenomenological determinations of PDFs have been found to give negative distributions, typically for gluon or sea quarks at low scales and small x [62–65]. Recently this possibility attracted theoretical attention, with efforts to establish whether PDFs in the $\overline{\text{MS}}$ scheme must in fact be positive [15, 45, 46].¹⁶ Imposing positivity as a constraint on PDF fits leads to reduced uncertainties [63, 66–68], and so if theoretically justified, in the $\overline{\text{MS}}$ or any other scheme, could be a valuable tool in the path towards the precision determination of PDFs.

We approach the question of positivity from two complementary perspectives. First, we adapt the theoretical argument of [46] and apply it to the factorisation schemes considered here. Secondly, we describe the positivity of the PDFs obtained as a result of our transformations of $\overline{\text{MS}}$ PDFs into alternative factorisation schemes.

¹⁵This kind of check has been performed for the momentum sum rule, e.g. [61], but not in case of the number sum rules. The obtained value of the momentum sum rule was consistent with 1 both at NLO and NNLO.

¹⁶The MPOS scheme discussed here was introduced in [15] for this purpose.

	AVERSA	DIS	KRK	KRKDY	DPOS	POS	MPOS	MPOS δ	PHYS
$C_F^{-1} \int_0^1 K_{qq}^{\text{FS}}(z) dz$	0	0	$-\frac{3}{2}$	0	0	0	$\frac{35}{9}$	$\frac{35}{18}$	$-\frac{1}{2}$

Table 8: Integral of the $K_{qq}^{\text{FS}}(z)$ kernel entering the number sum rule for N_q^{FS} .

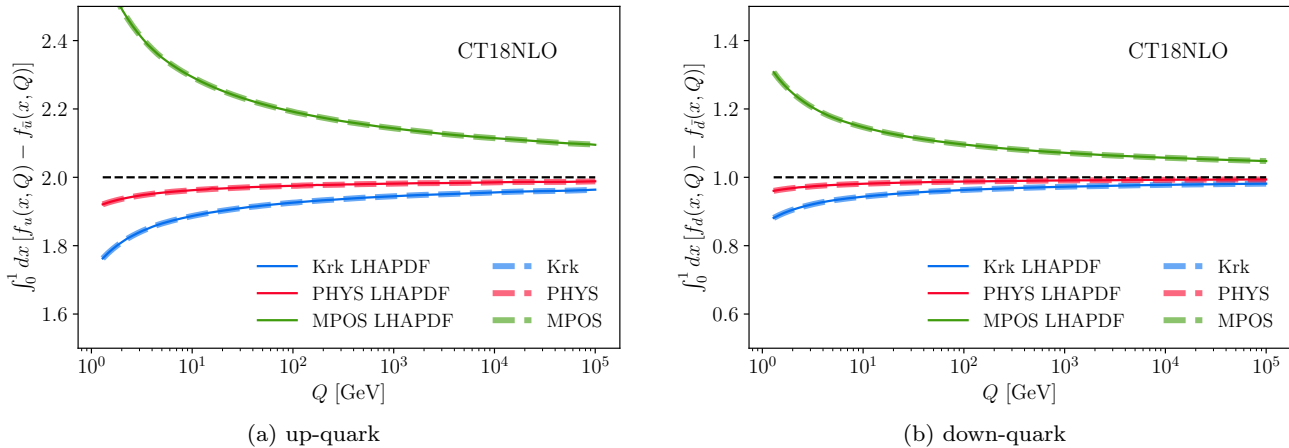


Fig. 9: Number sum rule as a function of the factorisation/renormalisation scale for (a) u -quark, and (b) d -quark. Compared are integrals obtained from LHAPDF files of the transformed PDFs and analytic integrals coming from Eq. (47).

3.5.1 Theoretical positivity

In [46] an argument is advanced, building on [15, 64], that the positivity of $\overline{\text{MS}}$ PDFs can be guaranteed by theoretical arguments based on properties of the implicit transformation from a basis of physical observables to a set of PDFs.

For a given convolution kernel K in the notation of Eq. (33), we adopt the terminology of [46] and define its ‘finite piece’ as

$$\text{fin}[K](z) = b(z) \log(1-z) + c(z) \log z + P(z), \quad (48)$$

that is, the functional part which remains with the distribution contributions (\mathcal{D}_k and Dirac-delta) subtracted.¹⁷ From the finite piece we define the ‘cumulant’ of the kernel as¹⁸

$$c[K](x) = \int_x^1 |\text{fin}[K](z)| \frac{dz}{z}. \quad (49)$$

¹⁷This is exactly analogous to the finite-piece defined in [46] and there denoted with subscript ‘ F ’, i.e. K_F . For the transformations and coefficient-functions considered here it can immediately be extracted from the central three columns of Tables 1 to 7.

¹⁸Note that in contrast to [46], we apply the absolute-value to the integrand rather than the integral. This leads to a strengthened condition below.

The argument of [46] concludes that the transformation given by the finite-piece is perturbative, i.e. the magnitude of the NLO modification is smaller than that of the input, provided that

$$\frac{\alpha_s(\mu)}{2\pi} \sum_b c [K_{ab}^{\text{FS}_1 \rightarrow \text{FS}_2}] \leq 1, \quad (50)$$

and the input-distribution is a positive, decreasing function. Clearly if the transformation is perturbative in this sense, and the input distribution is positive, the transformation gives a positive result.

The cumulants applied in [46] are calculated from the DIS and Higgs-production coefficient functions (in the $\overline{\text{MS}}$ scheme), i.e. precisely the content of Tables 5 and 7:

$$\tilde{C}_{qb}^{\text{FS}}(x) = c[C_b^{(1)\text{FS}}], \quad \tilde{C}_{gb}^{\text{FS}}(x) = c[C_{gb}^{(1)\text{FS}}]. \quad (51)$$

These are considered as transformation kernels applied to a ‘physical’ factorisation scheme argued to comprise measurements which are assumed to be positive and decreasing. We adapt the analysis of [46] and apply it to the factorisation schemes considered here, focusing explicitly on the role of the finite-part cumulant relied upon in the quantitative conclusions of [46].¹⁹

¹⁹We defer consideration of the δ - and distributional components, which differ between schemes, and of the applica-

These cumulants, summed over flavours, are shown in Fig. 10, together with illustrative values of $2\pi/\alpha_s(\mu)$ at relevant choices of μ to indicate the scale and x -values above which the criterion of [46], summarised in Eq. (50), indicates positivity.

Although this is a preliminary analysis, the modified criterion applied (as in [46]) at $x = 0.8$ leads to a similar conclusion as reached there, of 5 GeV as a scale above which positivity is indicated in this region for the $\overline{\text{MS}}$ scheme. The DIS scheme is similar, while the MPOS, MPOS δ and PHYS schemes lead²⁰ to a scale of 2 GeV, and the KRK and AVERSA scheme to 1 GeV.²¹

3.5.2 Empirical positivity

In contrast to the approach referred to in the previous section, which attempts to derive universal bounds on PDFs from first principles, here we summarise our observations about the positivity of proton PDFs in different factorisation schemes according to the transformations we have performed. This is naturally sensitive to the choice of PDF set used, and potentially to any positivity constraints imposed by the fitting group on the input $\overline{\text{MS}}$ PDFs. We consider PDF sets fitted using different methods and both with, and without positivity explicitly imposed upon the fit, concretely the CT18NLO PDF set in which goodness-of-fit function χ^2 is directly minimised over a chosen parameter space; the NNPDF40 PDF set fitted using neural-network replicas with positivity imposed on non-heavy flavours above $\sqrt{5}$ GeV, and the NNPDF40MC PDF set which resembles NNPDF40 except for the absence of intrinsic charm and the global imposition of positivity.

In this section we use ‘positive’ to mean ‘not definitely negative’, i.e.

$$xf(x) > -\varepsilon, \quad (52)$$

for tolerance parameter $\varepsilon > 0$ representing the target numerical precision for the numerical interpolation of the input PDF grids. We choose $\varepsilon \approx 10^{-4}$ (for comparison the LHAPDF 6 target (relative) interpolation uncertainty is 10^{-3} [26]). Negative PDFs values which are within ε of 0 could therefore be set to zero without perturbing the resulting PDF by more than the target interpolation uncertainty, and we disregard them.

tion of the argument to transformations between factorisation schemes, to future work.

²⁰Note that the omission of the δ contributions from the analysis here is especially relevant to any comparison between the MPOS and MPOS δ schemes.

²¹Note that at scales close to the flavour-threshold of the heavy quarks, the argument may need further refinement to include quark-mass effects in the coefficient functions used for the definition of the cumulants.

In general, we find that PDFs for all flavours in all schemes become positive at sufficiently large Q . More precisely, for all schemes the valence-quark-flavour PDFs are positive at all scales, while in some schemes the remaining light sea PDFs show slight negativity at very low scales and high- x . The gluon PDF is positive at all scales in all schemes but the DIS scheme, where for scales as large as 50 GeV the gluon PDF is negative for $x > 0.5$.

The heavy quarks, however, are negative close to their mass-thresholds, in all the schemes. This is due to the transformed quark PDFs receiving a negative contribution from the gluon input-PDF (shown in the decomposition plots of Figs. 5 and 22). Where the input quark distribution is small (as is the case for perturbatively-generated heavy quarks close to their mass-thresholds), this is sufficient to turn the resulting PDF negative.

For the c -quark, this is effectively overcome by the DGLAP evolution, to restore a positive output PDF, at around 10 GeV. In the case of the b -quark, scale required to restore positivity can be as high as 30 GeV. Plots illustrating this through the signed magnitude of the c - and b -quark PDFs in (x, Q) -space, in the MPOS scheme, are shown in Fig. 11.

Since this behaviour is due to the perturbatively-generated charm being small close to its flavour-threshold, we examine the effect of the inclusion of intrinsic charm in Fig. 12, comparing the NNPDF40 PDF set [69], which contains intrinsic charm, to the closely-related NNPDF40MC set [57] which contains only perturbatively-generated charm. This is sufficient to restrict the region in which negativity emerges, and its magnitude, to intermediate- x and low- Q (as shown in Fig. 6).

The intrinsic charm included in the NNPDF40 set thus ‘solves’ the problem of negativity at low- Q and high- x , which is common to all of the PDF sets in which the charm PDF is purely perturbative.

This cannot, however, resolve the problem of the b -quark PDF, which (as shown in Fig. 11d) is very negative, with negativity extending up to scales significantly above the mass threshold. This invites the possibility to define the factorisation-scheme transition kernels differently for heavy flavours, to include quark-mass effects.

The different low- x behaviour of the gluon PDFs at low scales in the different PDF sets (see Figs. 1, 17 and 18), due to the lack of constraints from data, drives the differences observed between the heavy-flavour PDFs at low- x and Q .

3.5.3 Conclusions

We observe a tension between the conclusions of the argument set out in [46] and our numerical calculations.

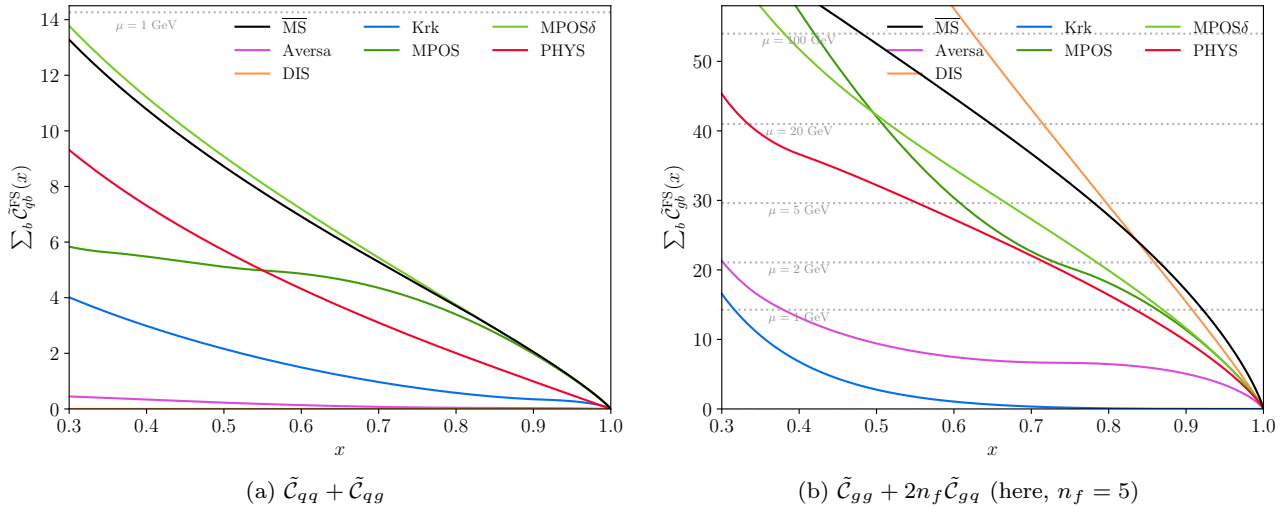


Fig. 10: Cumulants, as defined in Eq. (51), adapted from the positivity argument of [46]. The dotted grey lines show $2\pi/\alpha_s(\mu)$ at the labelled value of μ .

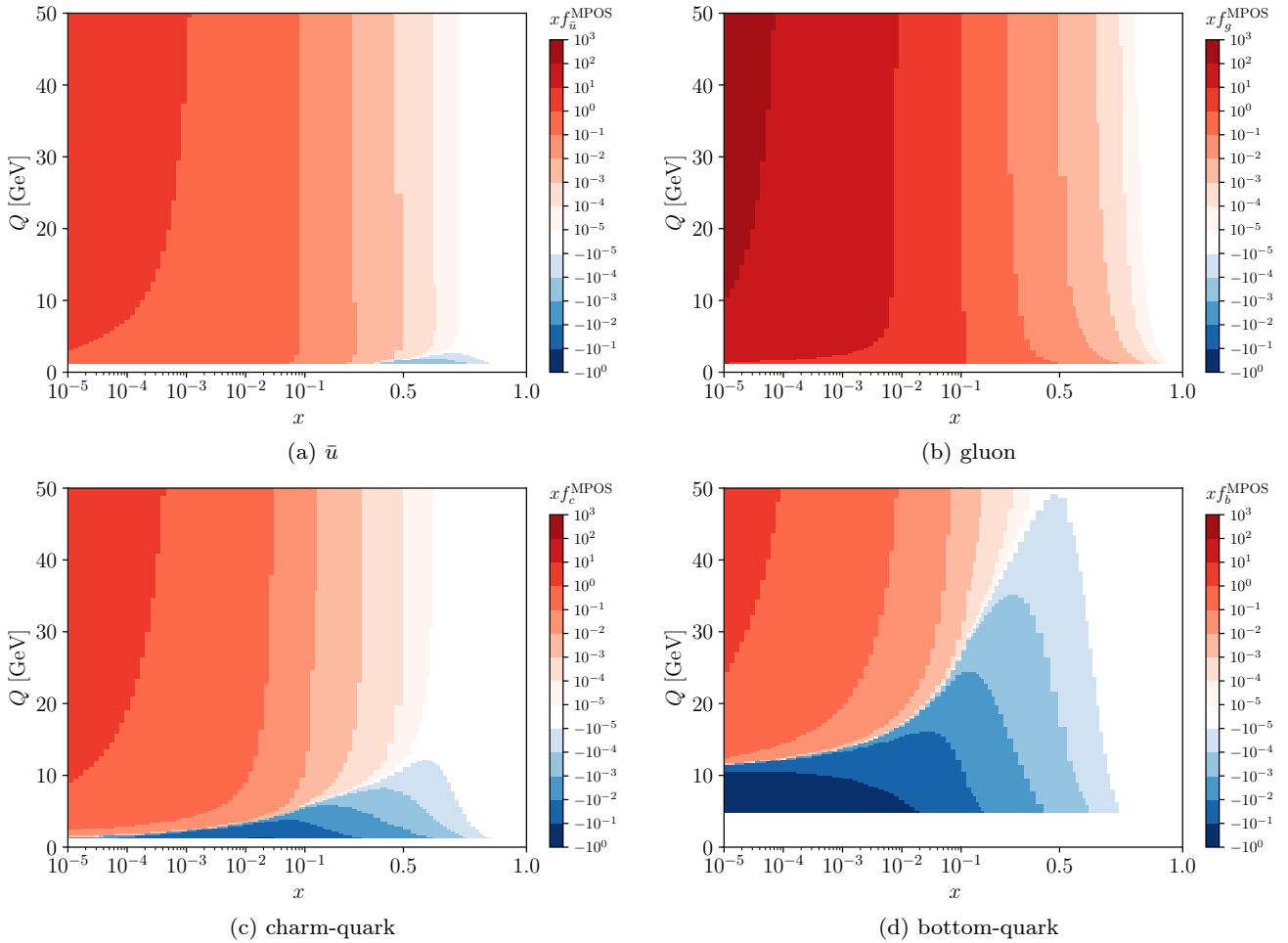


Fig. 11: Heatmap showing the sign and order-of-magnitude of heavy-quark CT18NLO PDFs $f_{b,c}^{\text{MPOS}}(x, Q)$ in the MPOS scheme as a function of momentum-fraction x and scale Q . Note that for the purposes of the discussion of Sec. 3.5.2 the lightest blue band shown here is treated as negligible.

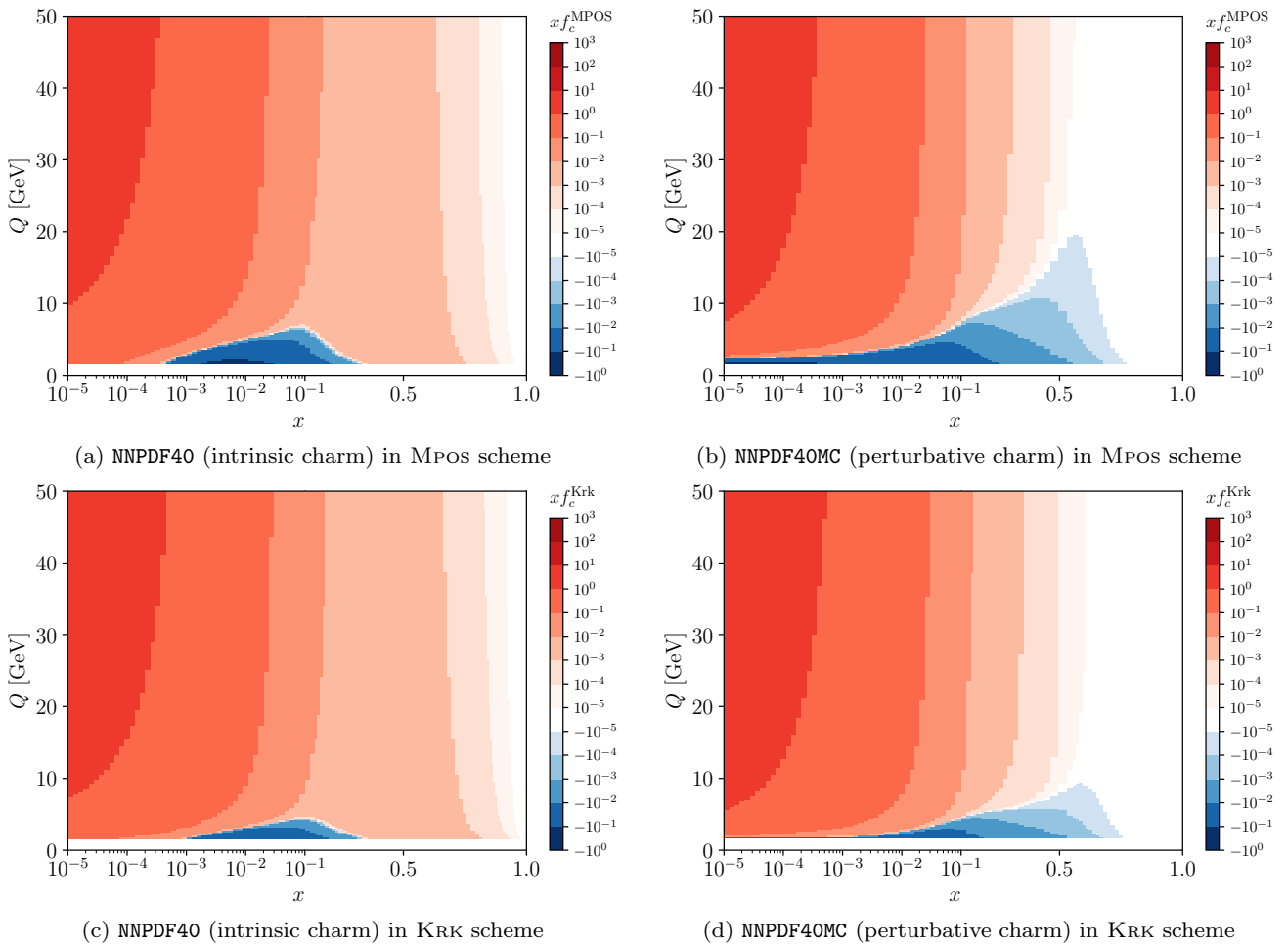


Fig. 12: Heatmap showing the sign and order-of-magnitude of charm-quark PDFs $f_c^{\text{KRK}, \text{MPOS}}(x, Q)$ in the KRK and MPOS schemes as a function of momentum-fraction x and scale Q , from the NNP40 [69] and NNP40MC [57] PDF sets. The key relevant difference is the inclusion of an intrinsic charm component in the NNP40 PDF set. Note that for the purposes of the discussion of Sec. 3.5.2 the lightest blue band shown here is treated as negligible.

Amongst other things, this could be due to the distributional \mathcal{D}_k or δ contributions, which differ between the schemes and which we neglect here. Additionally, at the low scales which emerge from the argument, it may not be justified to neglect the effect of the heavy quark masses in the coefficient functions used for the definition of the cumulants.

Since we observe significant negativity above the scales predicted by the argument of Sec. 3.5.1, imposing positivity on PDFs in these schemes across all flavours on the basis of this argument would be expected to substantially change the resulting PDFs.

Excluding the possibility of intrinsic c/b content, making the heavy-quark PDFs positive close to their mass-thresholds in all schemes would seem to require a significant modification to the gluon PDF.

Alternatively, another approach could be to use a ‘hybrid’ variable flavour number scheme, where the number of flavours changes not at the mass threshold but at a higher scale, e.g., at twice the heavy-quark mass [70, 71], which should mitigate the problem.

In principle, as hinted at in [46], the argument given there could be adapted to isolate constraints on individual flavours; one approach would be to use flavour-sensitive observables, such as F_2^c [72, 73] or tagged jet measurements [74–77], for the positive input ‘physical-scheme’ distributions.

3.6 Coefficient functions

As discussed in Sec. 2.1.2, a factorisation-scheme transformation induces a change to the coefficient functions compensating the corresponding modification of PDFs.

This mechanism restores the factorisation-scheme independence for observable quantities order-by-order in the coupling constant (up to the operative order in perturbation theory). This allows us to choose a scheme at our convenience, according to any desirable properties it exhibits, including those arising due to the effect of this compensating term on the partonic cross-sections (here represented by the coefficient functions).

In this section we consider the effect of this transformation on the coefficient functions of three illustrative processes: deep inelastic scattering (DIS), the Drell–Yan process (DY) and Higgs boson production via gluon fusion (in the large top quark mass limit).

In addition to the NLO contributions to the coefficient functions themselves, tabulated in Tables 5 to 7, we present plots of their Mellin transforms in Mellin-moment space, defined as

$$\mathcal{M}[f](N) := \int_0^1 z^{N-1} f(z) dz \quad (53)$$

for $N > 0$. These are collected in Fig. 13.

Under the Mellin transform, convolutions of functions as defined in Eq. (3), factorise into products of their Mellin transforms. The degree of singularity of functions and distributions in the $z \rightarrow 1$ limit is then made manifest in the $N \rightarrow \infty$ limit in Mellin-space.

Note that for a bounded function on $[0, 1]$ the N^{th} Mellin-moment is also bounded and decays as $N \rightarrow \infty$,

$$|\mathcal{M}[f](N)| \leq \frac{1}{N} \max_{[0,1]} |f| \quad (54)$$

whilst a distribution divergent at $z = 1$ may give a constant Mellin-transform,

$$\mathcal{M}[\delta(1-z)](N) = 1, \quad (55)$$

single logarithms of N ,

$$\mathcal{M}[\mathcal{D}_0(z)](N) \sim \log N \quad (56)$$

or double-logarithms of N ,

$$\mathcal{M}[\mathcal{D}_1(z)](N) \sim \frac{1}{2} \log^2 N. \quad (57)$$

The coefficients of Eq. (33) governing the asymptotic large- N behaviour of the Mellin moments of coefficient functions, and thus the degree of divergence as $z \rightarrow 1$, are therefore a_0 , a_1 and Δ .²³

²²Explicit expressions for the Mellin transforms of the remaining terms used within the decomposition of Eq. (33) are given in Appendix A.

²³As a consequence, the choice of method for imposing momentum conservation discussed in Sec. 3.3 can be significant for the $N \rightarrow \infty$ behaviour of the coefficient functions, and may implicitly be compared between the MPOS and MPOS δ schemes, see Fig. 13.

The \mathcal{D}_k contributions (‘threshold logarithms’) arise from a miscancellation of soft-gluon radiation between real- and virtual-diagrams, since the latter, despite regularising the former, contribute as $\delta(1-z)$, i.e. only at $z = 1$. Since the logarithms can be large, they can overcome the α_s suppression and lead to a breakdown of perturbation theory in the $z \approx 1$ region. Conventionally, this is addressed via their resummation [9, 78–88]. The differing coefficients arise from the different kinematic upper limits allowed by phase-space constraints on the transverse momentum of the radiated gluon at fixed boson mass between the DIS and Drell–Yan/Higgs processes, due to their differing kinematics [8, 81, 89].

3.6.1 DIS

Following [15] we consider the coefficient functions of the DIS structure-function F_2 ,

$$F_2(x, Q^2) = x \sum_a Q_a^2 \int_0^1 d\xi dz \delta(\xi z - x) f_a^{\text{FS}}(\xi, \mu_F) C_a^{\text{FS}}(z, Q^2; \mu_F, \mu_R), \quad (58)$$

where $Q_g^2 = \sum_{q,\bar{q}} Q_q^2$.

Following the reasoning of Sec. 2.1.2 but for a single incoming hadron,

$$C_q^{\text{FS}(0)} = \delta(1-z) \quad C_g^{\text{FS}(0)} = 0 \quad (59)$$

$$C_q^{\text{FS}(1)} = C_q^{\overline{\text{MS}}(1)} - K_{qq}^{\text{FS}} \quad C_g^{\text{FS}(1)} = C_g^{\overline{\text{MS}}(1)} - K_{gg}^{\text{FS}}. \quad (60)$$

The NLO contributions to the transformed coefficient functions are given in Table 5, and plotted in Mellin-space in Fig. 13a.

Notably, the DIS and AVERSA schemes exactly remove the distribution terms from the C_q coefficient function, as they were designed with explicit reference to the DIS process to absorb C_q into the quark PDF.²⁴ The same is true for C_g coefficient function in the case of the DIS scheme. As is evident from Table 5, in the POS-family schemes these contributions remain unaltered compared to $\overline{\text{MS}}$, while the \mathcal{D}_1 terms are removed in the PHYS scheme (but not \mathcal{D}_0). In the KRK schemes, the coefficients of these terms are all negative. In Fig. 13a we see the consequence of this: asymptotically the $\overline{\text{MS}}$ and POS-type schemes are positive at large- N ($\sim \log^2 N$), as are the PHYS scheme ($\sim \log N$); the KRK scheme is negative ($\sim -\log^2 N$). Note that, on the scale used for this plot, the Mellin-transformed LO coefficient function $\mathcal{M}[C_q^{\text{FS}(0)}](N)$ would have the constant value of $2\pi/\alpha_s \approx 53$.

²⁴Hence, the DIS and AVERSA C_q coefficient functions in Fig. 13a are identical.

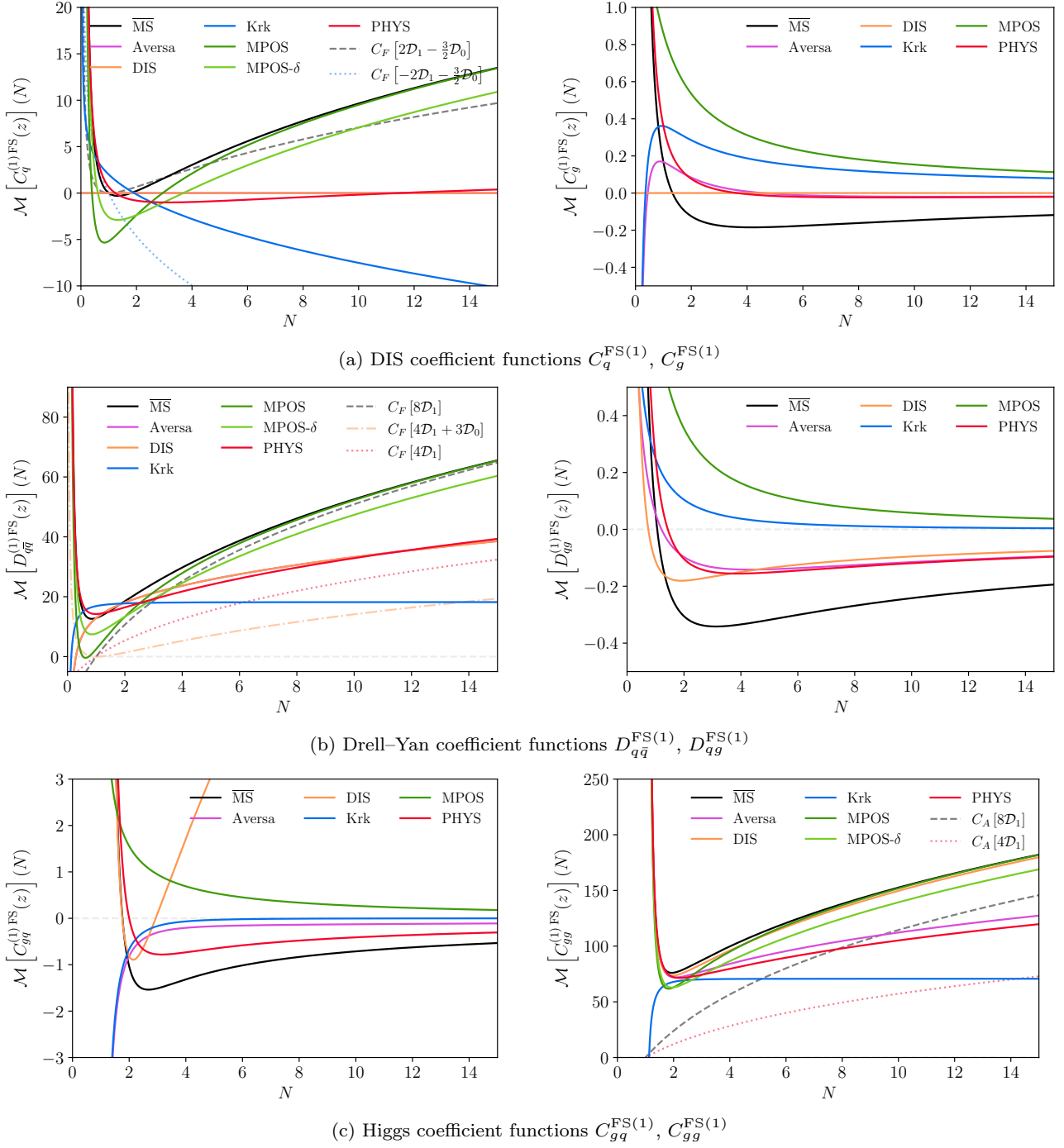


Fig. 13: The NLO contributions to coefficient functions for the DIS, Drell-Yan and Higgs production processes, in Mellin space. Where relevant, the Mellin moments of the distributions governing the asymptotic large- N behaviour have also been plotted. Note that, the LO term $\mathcal{M}[C_q^{\text{FS}(0)}](N)$, which is not plotted here, would on these plots correspond to a constant value of $2\pi/\alpha_s(\mu) \approx 53$.

For the gluon coefficient-function, where the LO contribution is zero, the AVERSA and KRK schemes are negative at small- N whereas the others are positive. At large- N all converge to zero due to the absence of a_0, a_1, Δ terms.

3.6.2 Drell–Yan

The coefficient functions for the Drell–Yan process are transformed as described in Sec. 2.1.2,

$$D_{q\bar{q}}^{\text{FS}(0)} = \delta(1-z) \quad D_{qg}^{\text{FS}(0)} = 0 \quad (61)$$

$$D_{q\bar{q}}^{\text{FS}(1)} = D_{q\bar{q}}^{\overline{\text{MS}}(1)} - 2K_{q\bar{q}}^{\text{FS}} \quad D_{qg}^{\text{FS}(1)} = D_{qg}^{\overline{\text{MS}}(1)} - K_{qg}^{\text{FS}} \quad (62)$$

and are given in Table 6 and their Mellin-transforms plotted in Fig. 13b.

In this case, the KRK scheme exactly removes the divergent \mathcal{D}_1 distribution terms from the $D_{q\bar{q}}$ coefficient function, while this contribution is partially mitigated (halved) in the AVERSA/DIS and PHYS schemes.

This can be seen in Fig. 13b, where for the $q\bar{q}$ -channel coefficient function, the large- N behaviour divides the schemes into three main groups: the KRK-scheme, which is asymptotically constant; the PHYS and AVERSA/DIS schemes, which diverge as $2C_F \log^2 N$; and the $\overline{\text{MS}}$ and POS-type schemes, which diverge as $4C_F \log^2 N$.

In this respect the KRK scheme can be seen to have a similar function for the Drell–Yan process at large- N as the DIS scheme has for DIS, removing the logarithmic terms from the coefficient function to leave it asymptotically-constant. This is due to the \mathcal{D}_1 terms being entirely removed by the choice $a_1 = 4$ in $K_{q\bar{q}}^{\text{KRK}}$.

For the qg -channel coefficient function, the MPOS and KRK schemes exhibit positivity in Mellin space, whereas the others are negative. All are asymptotically zero due to the absence of a_0, a_1 and Δ terms.

3.6.3 Higgs

The coefficient functions for the gluon-fusion Higgs-production process are again transformed as described in Sec. 2.1.2,

$$C_{gg}^{\text{FS}(0)} = \delta(1-z) \quad C_{gq}^{\text{FS}(0)} = 0 \quad (63)$$

$$C_{gg}^{\text{FS}(1)} = C_{gg}^{\overline{\text{MS}}(1)} - 2K_{gg}^{\text{FS}} \quad C_{gq}^{\text{FS}(1)} = C_{gq}^{\overline{\text{MS}}(1)} - K_{gq}^{\text{FS}}. \quad (64)$$

They are given in Table 7 and their Mellin-transforms are plotted in Fig. 13c.

As for Drell–Yan, in the flavour-diagonal channel (here gg), the KRK scheme exactly removes the distribution terms \mathcal{D}_1 from the C_{gg} coefficient function, while

the contribution is partially mitigated in the AVERSA and PHYS schemes, due to the respective choices $a_1 = 4$ and $a_1 = 2$ for K_{gg}^{FS} . This can be seen in the plots of Fig. 13c, where the KRK-scheme coefficient function is again rendered asymptotically constant, in contrast to the others which either diverge as $4C_A \log^2 N$ ($\overline{\text{MS}}$, DIS, POS-type), or $2C_A \log^2 N$ (AVERSA, PHYS).

For C_{gq} the coefficients are again asymptotically-zero at large- N for all schemes, save for the DIS scheme due to its conventional local-momentum-conserving definition in terms of the flavour-diagonal K_{qg}^{DIS} in Eq. (30), which contains \mathcal{D}_0 and \mathcal{D}_1 contributions.

4 Phenomenological impact of scheme choice

As described in Sec. 3.6, the choice of factorisation scheme for an NLO calculation is compensated to the same perturbative order by a modification of the partonic cross-section, and so induces only formally-NNLO changes to an NLO calculation, akin to factorisation- and renormalisation-scale variation.²⁵ However, some observables of phenomenological interest may only be non-zero in the real-emission kinematics, leading to an effectively-LO calculation for which the factorisation-scheme dependence is uncompensated.

The effect of the factorisation-scheme choice on these observables for an NLO calculation of $pp \rightarrow X$ is identical to their effect on an LO calculation of $pp \rightarrow X + j$. Therefore, in this section we present differential distributions corresponding to a leading-order calculation of $pp \rightarrow Z + j$ and $pp \rightarrow H^0 + j$ as an example.

This illustrates the effect of varying the factorisation scheme on the leading-jet distributions of an NLO calculation of the Drell–Yan and gluon-fusion Higgs processes. These have been chosen because they proceed via the $q\bar{q}$ and gq channels respectively at leading-order.

The general observations made may be expected to generalise to a wider range of processes, since they relate essentially to the kinematic region in (x, Q) probed within each PDF.

For the calculations in this section, we use Herwig 7 [92, 93] with the NNPDF40MC PDF set [57], transformed into the different factorisation schemes and stored in LHAPDF 6 format [26]; accordingly, we adopt $\alpha_s(M_Z) = 0.118$. All calculations are done at fixed-order without any parton shower resummation or other corrections.

²⁵This has previously been studied for the inclusive jet cross-section for a parametrised transition between the $\overline{\text{MS}}$ and DIS schemes, [90, 91] where the variation at LO was found to be 40% and at NLO 8%.

4.1 Z -plus-jet

We use a set-up appropriate for LHC Run II, with a centre-of-mass energy of 13 TeV and fiducial cuts

$$p_T^{\ell_{1,2}} > 25 \text{ GeV}, \quad |\eta^{\ell_{1,2}}| < 3.5, \quad (65a)$$

$$M_{\ell\ell} \in [66, 116] \text{ GeV}, \quad (65b)$$

similar to those used by ATLAS [94] and CMS [95]. We identify jets using the anti- k_T algorithm [96] with jet-radius $R = 0.4$ and minimum transverse momentum of 10 GeV. We use the invariant mass of the lepton pair as the dynamic renormalisation and factorisation scale,

$$\mu_R = \mu_F = M_{\ell\ell}. \quad (66)$$

The shaded uncertainty band illustrates the ($\overline{\text{MS}}$ -scheme) factorisation-scale uncertainty and corresponds to the envelope given by factorisation-scale variation by a factor of two in each direction, $\mu_F \in \{\frac{1}{2}, 1, 2\}M_{\ell\ell}$.

The results are shown in Fig. 14 for the transverse momentum of the Z -boson and the rapidity of the first jet (at LO, this is the only jet, and comprises a single parton). In addition to the total contribution from proton-proton scattering (Fig. 14a), the distributions have been further subdivided into the contributions from the quark-antiquark (Fig. 14b) and the quark-gluon channels (Fig. 14c) separately.

The uncertainty on the distributions arising from the factorisation-scheme variation is largest in the $q\bar{q}$ -channel, in which it ranges from approximately 30% at low- p_T to around 5% at high- p_T . The jet-rapidity distribution shows a modest rapidity-dependence on the factorisation-scheme uncertainty. The effect in the qg channels is in the same direction with the same scale dependence, but at most 10% at low- p_T ; the scheme-uncertainty of the rapidity distribution grows strongly with rapidity for the MPOS and MPOS δ schemes (to $\sim 20\%$) whereas for other schemes it is modestly suppressed.

Distributions calculated with factorisation schemes other than $\overline{\text{MS}}$ are consistently smaller than the $\overline{\text{MS}}$ distributions, as might be expected from the plots of the transformed quark PDFs alone. The hierarchy of schemes matches that of the PDFs for the relevant (x, Q) region; this can ultimately be traced back to the coefficient of $p_{qg}(z) \log(1-z)$ in the qg transformation kernels, which separates the schemes into three emergent groups (i) $\overline{\text{MS}}$, (ii) DIS, PHYS and AVERSA, and (iii) KRK, MPOS and MPOS δ .

As can be seen from Fig. 14a, the factorisation-scheme uncertainty here exceeds the scale-uncertainty (here both formally at relative order $\mathcal{O}(\alpha_s)$), especially at low- p_T and in the extremes of the jet-rapidity distribution.

4.2 Higgs-plus-jet

Again we use a set-up appropriate for LHC Run II, here for $pp \rightarrow H^0 \rightarrow \tau^+\tau^-$ with a centre-of-mass energy of 13 TeV and fiducial cuts

$$p_T^{\tau_{1,2}} > 25 \text{ GeV}, \quad |\eta^{\tau_{1,2}}| < 3.5, \quad (67a)$$

$$M_{\tau\tau} \in [115, 135] \text{ GeV} \quad (67b)$$

and identify jets using the anti- k_T algorithm [96] with jet-radius $R = 0.4$ and minimum transverse momentum of 10 GeV. We use the invariant mass of the tauon-pair as the dynamic renormalisation and factorisation scale,

$$\mu_R = \mu_F = M_{\tau\tau} \quad (68)$$

and work in the Higgs effective theory in the infinite top-quark-mass limit. The shaded uncertainty band again corresponds to $\overline{\text{MS}}$ -scheme factorisation-scale variation by a factor of two in each direction, $\mu_F \in \{\frac{1}{2}, 1, 2\}M_{\tau\tau}$.

The results are shown in Fig. 15 for the transverse momentum of the Higgs-boson and the rapidity of the first jet. In addition to the total result for proton-proton scattering (Fig. 15a), the distributions have been subdivided into contributions from the gluon-gluon (Fig. 15b) and the quark-gluon channels (Fig. 15c) separately.

In contrast to the $Z + j$ process we observe that all the schemes lead to higher cross-sections than that using the $\overline{\text{MS}}$ scheme; this is in accordance with the general directional effect of the scheme transformations shown in Fig. 1. The gq -channel dominates the total and hence also the scheme-uncertainty.

For MPOS and MPOS δ we observe deviations from $\overline{\text{MS}}$ of up to 20% in the central-rapidity region and at low transverse momenta. The deviation for KRK is smaller, not exceeding 10% in most of the kinematic regions. Again we see grouping of the schemes, however, slightly different from that observed for $Z + j$: (i) MPOS & MPOS δ , (ii) KRK, AVERSA, DIS, and (iii) PHYS & $\overline{\text{MS}}$. Another prominent difference compared to the $Z + j$ is related to the shape of the rapidity distribution in the qg channel. For $Z + j$ we observe single peak shape, whereas, for the $H + j$ we see a double-hump structure with a deep in the central rapidity region. This shape is present already for the $\overline{\text{MS}}$ scheme but it is further enhanced in the MPOS, MPOS δ , and KRK schemes (leading to lower minimum in the central rapidity and maxima at $y^{\text{jet}} = \pm 2.5$).

As can be seen from Fig. 15a, the factorisation-scheme uncertainty again exceeds the scale-uncertainty, especially at low- p_T and in the centre and extremes of the jet-rapidity distribution. The scale-variation uncertainty is notably smaller in magnitude here than for $Z + j$, despite the scheme-variation uncertainty being

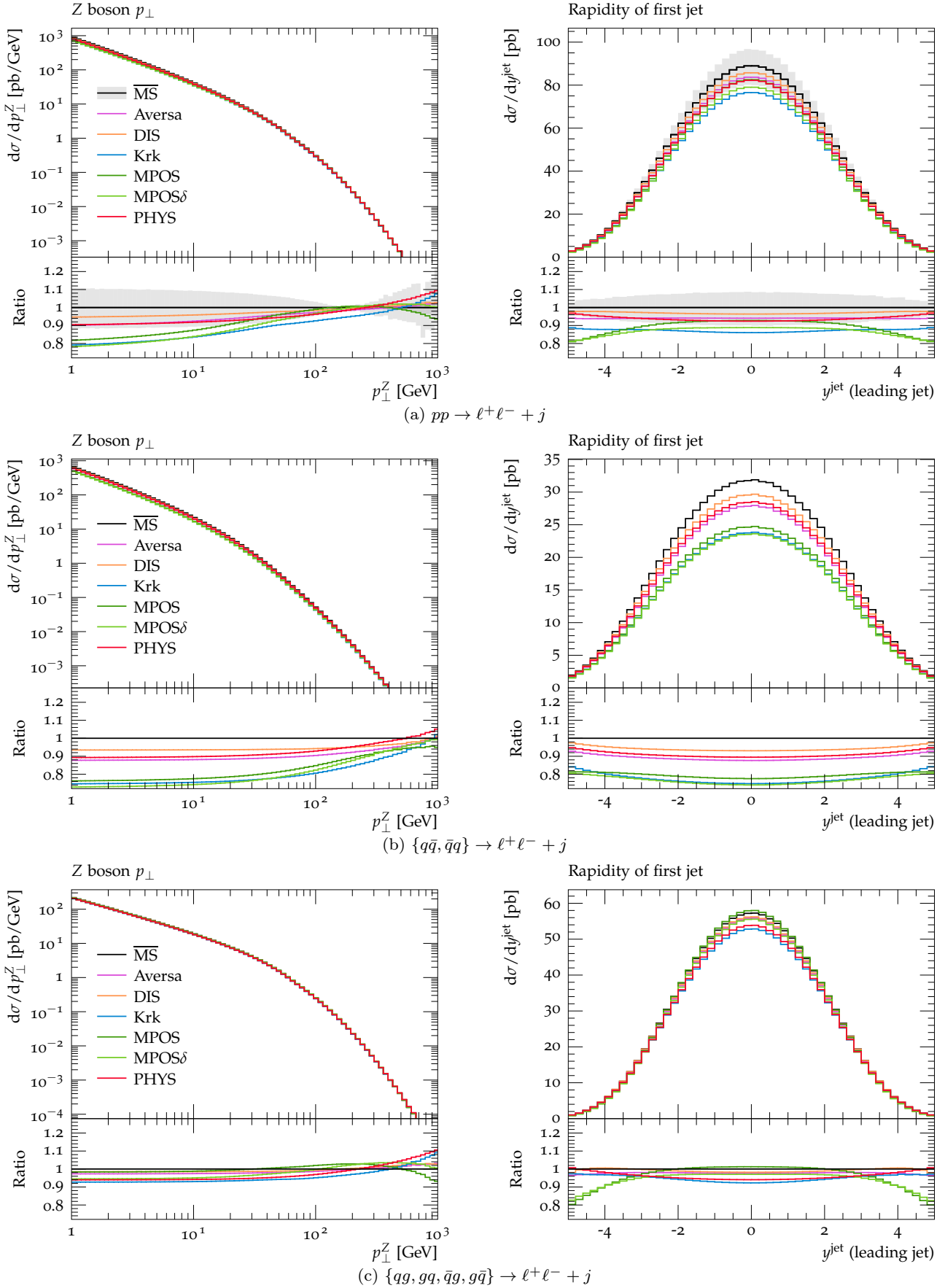


Fig. 14: Factorisation-scheme dependence of differential cross-sections for $Z + j$ production at the LHC. Leading-order predictions for these observables correspond to an NLO calculation of the Drell-Yan process.

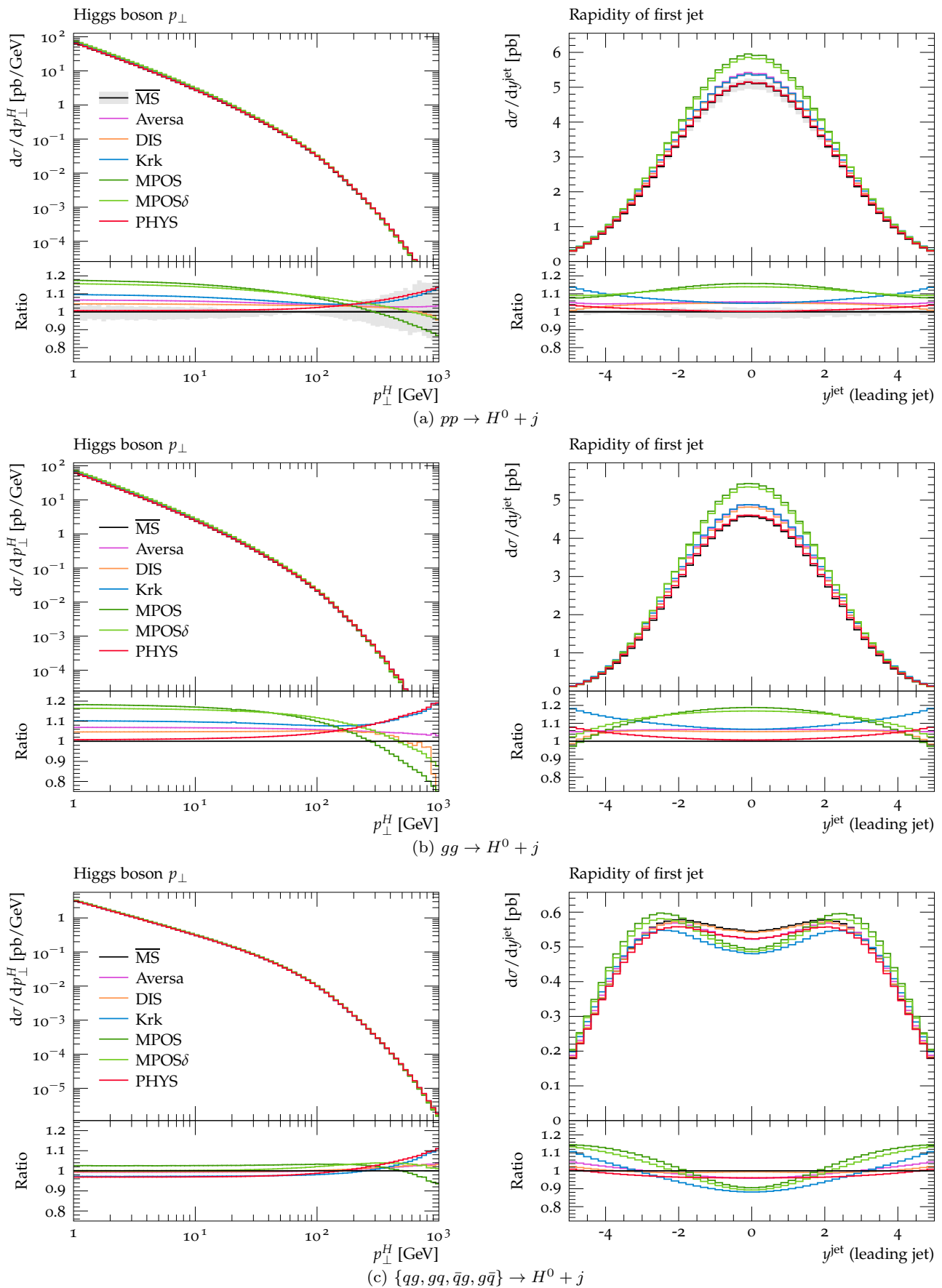


Fig. 15: Factorisation-scheme dependence of differential cross-sections for $H + j$ production at the LHC. Leading-order predictions for these observables correspond to an NLO calculation of the Higgs-production process.

comparable, implying that scale-variation uncertainty is an unreliable guide to scheme-variation uncertainty.

5 Discussion and conclusions

In this work we have investigated for the first time the relationship between many of the different factorisation schemes proposed in the literature for NLO QCD calculations. In doing so we have identified features common to all such schemes. This hints at the possibility of a consensus scheme achieving multiple objectives simultaneously.

In general the transformations are dominated by the distribution and logarithmic terms, with finer details of the polynomial piece $P(z)$ mostly numerically suppressed. Setting this to zero for convenience, the schemes discussed here may be considered special cases of the following general expressions:²⁶

$$K_{qq}^{\overline{\text{MS}} \rightarrow \text{FS}} = C_F \left[a_{qq} \left(2\mathcal{D}_1 - (1+z) \log(1-z) \right) - \frac{3}{2} b_{qq} \mathcal{D}_0 - c_{qq} p_{qq}(z) \log z - \Delta_{qq} \delta(1-z) \right] \quad (69)$$

$$K_{qq}^{\overline{\text{MS}} \rightarrow \text{FS}} = T_R \left[a_{qq} p_{qq}(z) \log(1-z) - c_{qq} p_{qq}(z) \log z \right] \quad (70)$$

$$K_{gq}^{\overline{\text{MS}} \rightarrow \text{FS}} = C_A \left[a_{gq} p_{gq}(z) \log(1-z) - c_{gq} p_{gq}(z) \log z \right] \quad (71)$$

$$K_{gg}^{\overline{\text{MS}} \rightarrow \text{FS}} = C_A \left[a_{gg} \left(2\mathcal{D}_1 + \left(\frac{1}{z} - 2 + z(1-z) \right) \times \log(1-z) \right) - 2c_{gg} p_{gg}(z) \log z - \Delta_{gg} \delta(1-z) \right] \quad (72)$$

where $a_{qq}, a_{gg} \in \{0, 1, 2\}$, $a_{qg}, a_{gq} \in \{1, 2\}$, $b_{qq} \in \{0, 1\}$, $c_{qq}, c_{qg}, c_{gq}, c_{gg} \in \{0, 1\}$, and Δ_{qq}, Δ_{gg} are fixed by the momentum sum-rule as in Eq. (26). Note that the functions appearing in the coefficients of $\log(1-z)$ in $K_{qq}^{\overline{\text{MS}} \rightarrow \text{FS}}$ and $K_{gg}^{\overline{\text{MS}} \rightarrow \text{FS}}$ correspond to the remainder after the subtraction of divergent (plus-distribution) contribution \mathcal{D}_0 from $p_{qq}(z)$ and $p_{gg}(z)$ respectively. Whilst we do not claim that all possible factorisation schemes of interest fit this pattern, it is notable that the domain of interest for factorisation-scheme variation within the

²⁶With the exception of $K_{ga}^{\overline{\text{MS}} \rightarrow \text{DIS}}$, which are unique in being determined by Eq. (32) rather than from consideration of the relevant splitting channels, and $K_{gg}^{\overline{\text{MS}} \rightarrow \text{AVERSA}}$, which uses only a single (rational) term from $p_{gg}(z)$ in its coefficient of $\log z$.

literature is much smaller than might initially be assumed and appears to be parametrised by a handful of discrete variables.

Following the Mellin-space arguments of Sec. 3.6, for the hadron–hadron Drell–Yan and Higgs coefficient functions considered there to be bounded in Mellin-space we require $a_{qq} = a_{gg} = 2$ (with the consequence that the DIS coefficient function $C_q^{\text{FS}(1)}$ is unbounded).

This inclusion of the threshold logarithms within the PDFs substantially changes them (in particular the gluon at low- x) but could in principle be extended to higher orders in QCD or adapted to use resummed expressions in the PDF transformations and their perturbative truncations in the coefficient functions.

The question of the relationship between factorisation-scheme choice and PDF positivity remains open, but we have observed empirically the extent to which it is violated for transformed $\overline{\text{MS}}$ PDFs, as well as studying the argument of [46] applied to schemes other than $\overline{\text{MS}}$. We defer a detailed consideration of the provable positivity properties of factorisation schemes to future work.

Finally, as highlighted in Sec. 3, our study considers only PDFs transformed from $\overline{\text{MS}}$ input PDFs at each scale, while PDFs in alternative factorisation schemes may also be obtained by performing the evolution, or the evolution and the fit, in the scheme of interest. The conclusions reached here may not apply to PDFs obtained by these methods. We defer consideration of this to future work.

Acknowledgements

The authors wish to thank John Collins and Jonathan Gaunt for valuable discussions about the PDF sum-rules and the significance of their scheme-dependence, and Stefano Forte and Felix Hekhorn for productive correspondence about the argument and results of [46]. We are grateful to the late Staszek Jadach for the initial discussions that prompted us to pursue this work, and to Wiesław Płaczek for comments on the manuscript.

The work of S.D. and A.K. was supported by National Science Centre Poland under the Sonata Bis grant No 2019/34/E/ST2/00186. The work of A.S. and J.W. was supported by the National Science Centre Poland grant No 2019/34/E/ST2/00457. A.S. is also supported by the Priority Research Area Digiworld under the program ‘Excellence Initiative – Research University’ at the Jagiellonian University in Krakow. We gratefully acknowledge the Polish high-performance computing infrastructure PLGrid (HPC Centre: ACK Cyfronet AGH) for providing computing facilities and support within computational grant PLG/2023/016880.

Appendix A: Notation and conventions

The leading-order colour-factor-stripped DGLAP splitting functions are given in four dimensions by²⁷

$$p_{qq}(z) = \frac{1+z^2}{1-z} \quad (\text{A.1})$$

$$p_{qg}(z) = z^2 + (1-z)^2 \quad (\text{A.2})$$

$$p_{gq}(z) = \frac{1+(1-z)^2}{z} \quad (\text{A.3})$$

$$p_{gg}(z) = \frac{1}{1-z} + \frac{1}{z} - 2 + z(1-z) \quad (\text{A.4})$$

Perturbative expansions are indexed according to the convention of Eq. (11),

$$\begin{aligned} F(\alpha_s, \mu) &= F^{(0)}(\mu) + \left(\frac{\alpha_s(\mu)}{2\pi}\right) F^{(1)}(\mu) + \dots \\ &= \sum_k \left(\frac{\alpha_s(\mu)}{2\pi}\right)^k F^{(k)}(\mu). \end{aligned} \quad (\text{A.5})$$

The leading-order expansion of the $\overline{\text{MS}}$ DGLAP kernels referred to in Sec. 2.1.3 is then

$$P_{ab}^{\overline{\text{MS}}(1)}(z) = C_F [p_{qq}(z)]_+ \quad (\text{A.6})$$

$$P_{ab}^{\overline{\text{MS}}(1)}(z) = T_R p_{qg}(z) \quad (\text{A.7})$$

$$P_{ab}^{\overline{\text{MS}}(1)}(z) = C_F p_{gq}(z) \quad (\text{A.8})$$

$$\begin{aligned} P_{ab}^{\overline{\text{MS}}(1)}(z) &= 2C_A \left(\left[\frac{1}{1-z} \right]_+ + \frac{1}{z} - 2 + z(1-z) \right) \\ &\quad - \frac{4n_f T_R - 11C_A}{6} \delta(1-z). \end{aligned} \quad (\text{A.9})$$

In the convention of Sec. 2.1.3, the QCD β -function has the perturbative expansion

$$\beta^{(0)} = 0 \quad (\text{A.10})$$

$$\beta^{(1)} = 0 \quad (\text{A.11})$$

$$\beta^{(2)} = \frac{\pi}{3} (4n_f T_R - 11C_A). \quad (\text{A.12})$$

The decomposition of a kernel in the convention of Eq. (33), as in Tables 1 to 7, allows for the direct calculation of its Mellin transform using the following results,

²⁷Note that the flavour indices are transposed here relative to a recent paper by some of the same authors [20]. The convention employed here allows Eq. (4) to be considered as matrix-multiplication without a transposition.

collected here for reference with respect to Sec. 2.1.2:

$$\mathcal{M}[\mathcal{D}_0(z)](N) = -H_{N-1} \quad (\text{A.13})$$

$$\mathcal{M}[\mathcal{D}_1(z)](N) = \frac{1}{2} \left(H_{N-1}^2 + H_{N-1}^{(2)} \right) \quad (\text{A.14})$$

$$\mathcal{M}[z^k](N) = \frac{1}{N+k} \quad (\text{A.15})$$

$$\mathcal{M}[z^k \log(1-z)](N) = -\frac{H_{N+k}}{N+k} \quad (\text{A.16})$$

$$\mathcal{M}[z^k \log z](N) = -\frac{1}{(N+k)^2} \quad (\text{A.17})$$

$$\mathcal{M}\left[z^k \frac{\log z}{1-z}\right](N) = H_{N+k-1}^{(2)} - \frac{\pi^2}{6} \quad (\text{A.18})$$

$$\mathcal{M}[\delta(1-z)](N) = 1. \quad (\text{A.19})$$

Here $H_N^{(r)}$ denotes the N^{th} generalised harmonic number of order r ,

$$H_N^{(r)} = \sum_{k=1}^N \frac{1}{k^r}; \quad (\text{A.20})$$

additionally, we omit the order for the harmonic numbers of order 1: $H_N^{(r)} \equiv H_N$. Note that

$$H_N = \log N + \gamma_E + \mathcal{O}\left(\frac{1}{n}\right). \quad (\text{A.21})$$

Appendix B: Supplementary transformed PDFs

In this section we present plots showing additional transformed PDFs to complement the selection of plots included in the main text. In Fig. 16 we show the remaining partonic flavours omitted from Fig. 1, using the CT18NLO $\overline{\text{MS}}$ PDF set. In Figs. 17 and 18 we show counterparts to the transformed PDFs presented in the main text using NNPDF40MC [57] and MSHT20n1o [58] instead of CT18NLO.

Appendix C: Supplementary transformation decompositions

In this section we present additional decomposition plots to support the discussion of Sec. 3.2. For ease of reference an overview of all included decomposition plots is given in Table 9.

In Figs. 19 to 22 we show the remaining three schemes (AVERSA, DIS and MPOS δ) omitted from the plots of Sec. 3.2, again using the CT18NLO PDF set and at $Q = 2$ GeV.

In Figs. 23 to 26 we present decomposition plots for the factorisation schemes shown in the main text (KRK, PHYS, MPOS), using the CT18NLO PDF set at

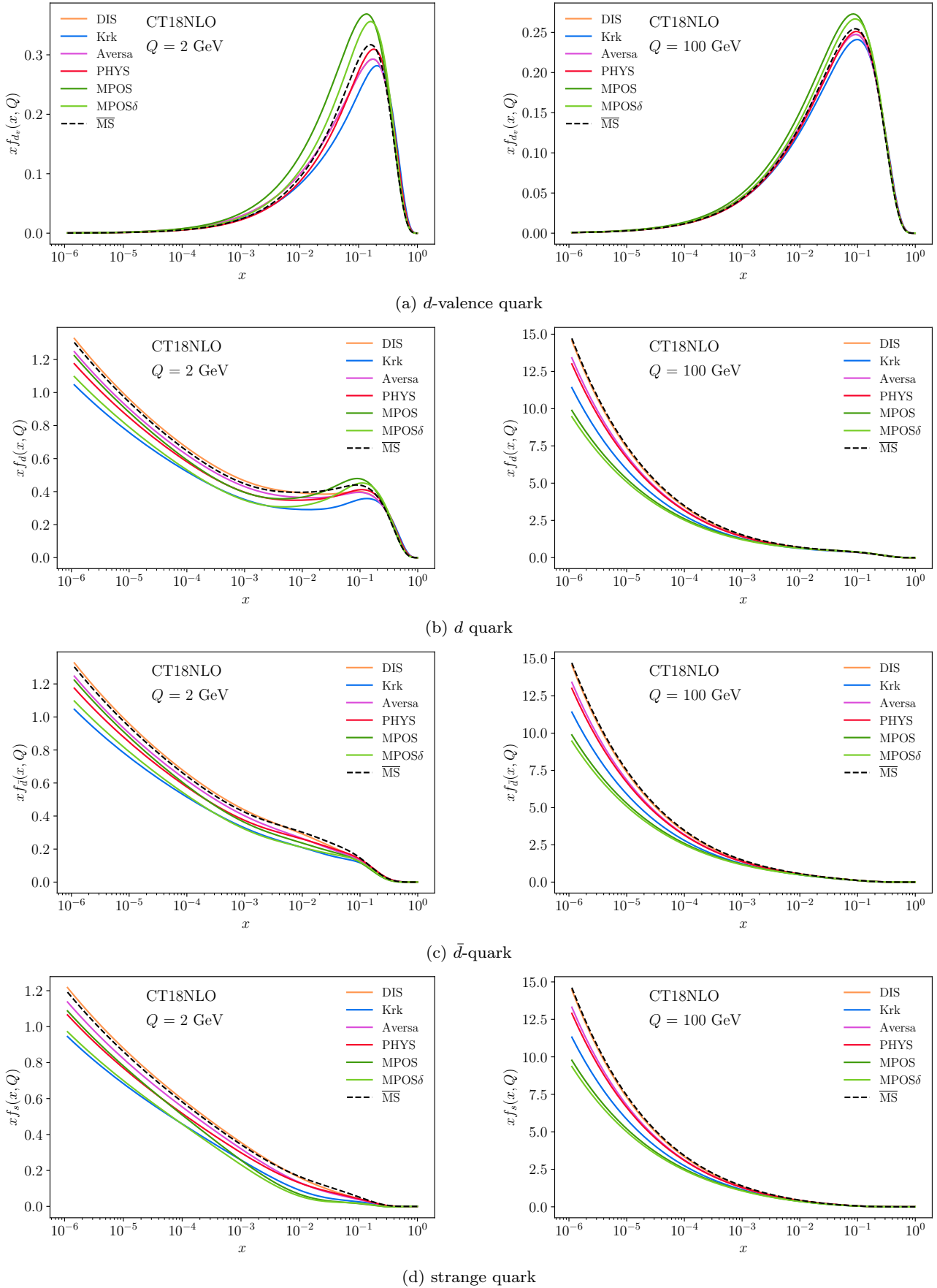


Fig. 16: Comparison of transformed CT18NLO PDFs in different schemes for d -valence, d , \bar{d} , and s , at $Q = 2$ GeV (left) and 100 GeV (right). Companion to Fig. 1.

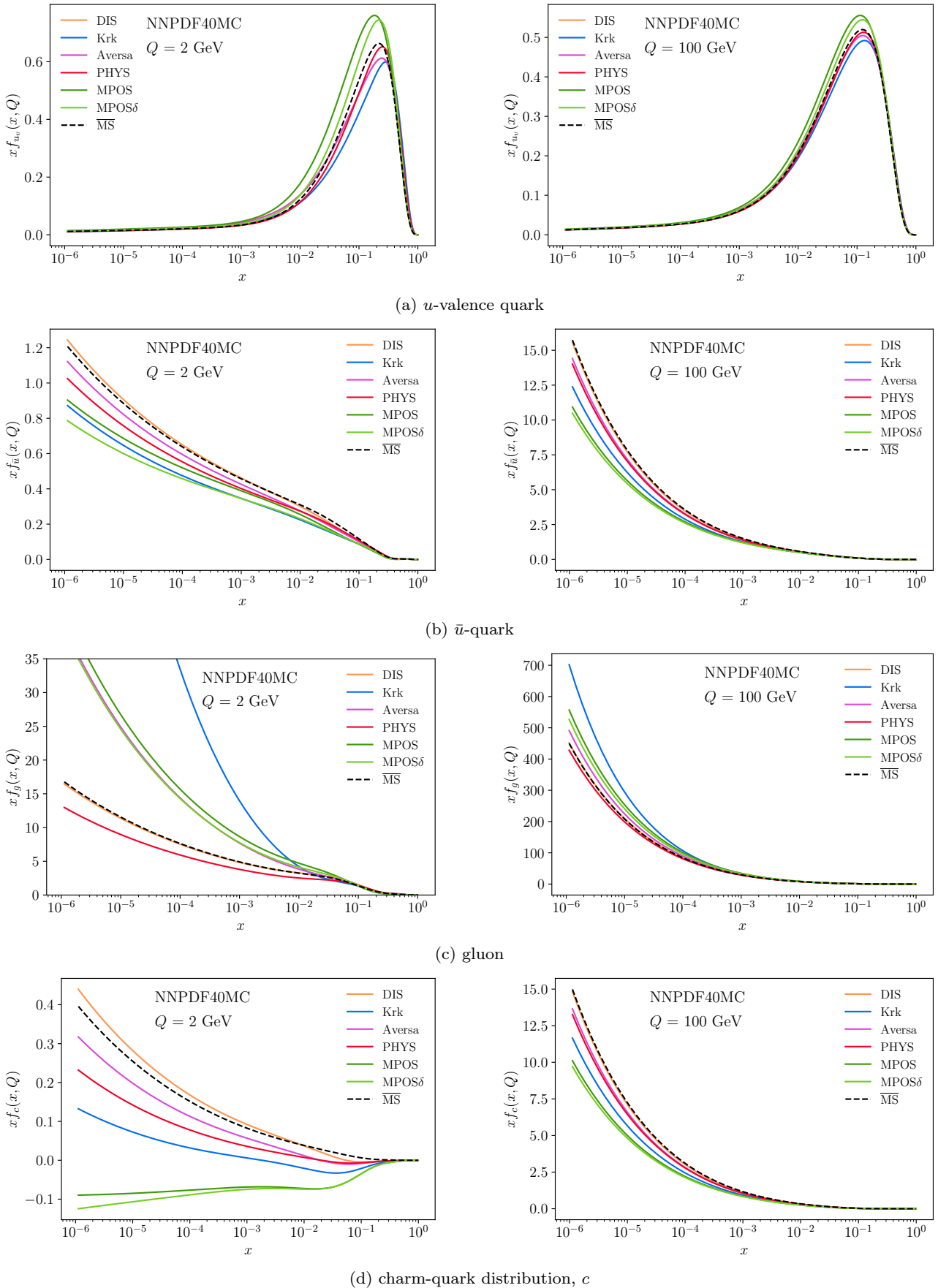


Fig. 17: Comparison of transformed NNP40MC PDFs in different schemes for u -valence, \bar{u} , gluon, and charm at $Q = 2$ GeV (left) and 100 GeV (right). Companion to Fig. 1.

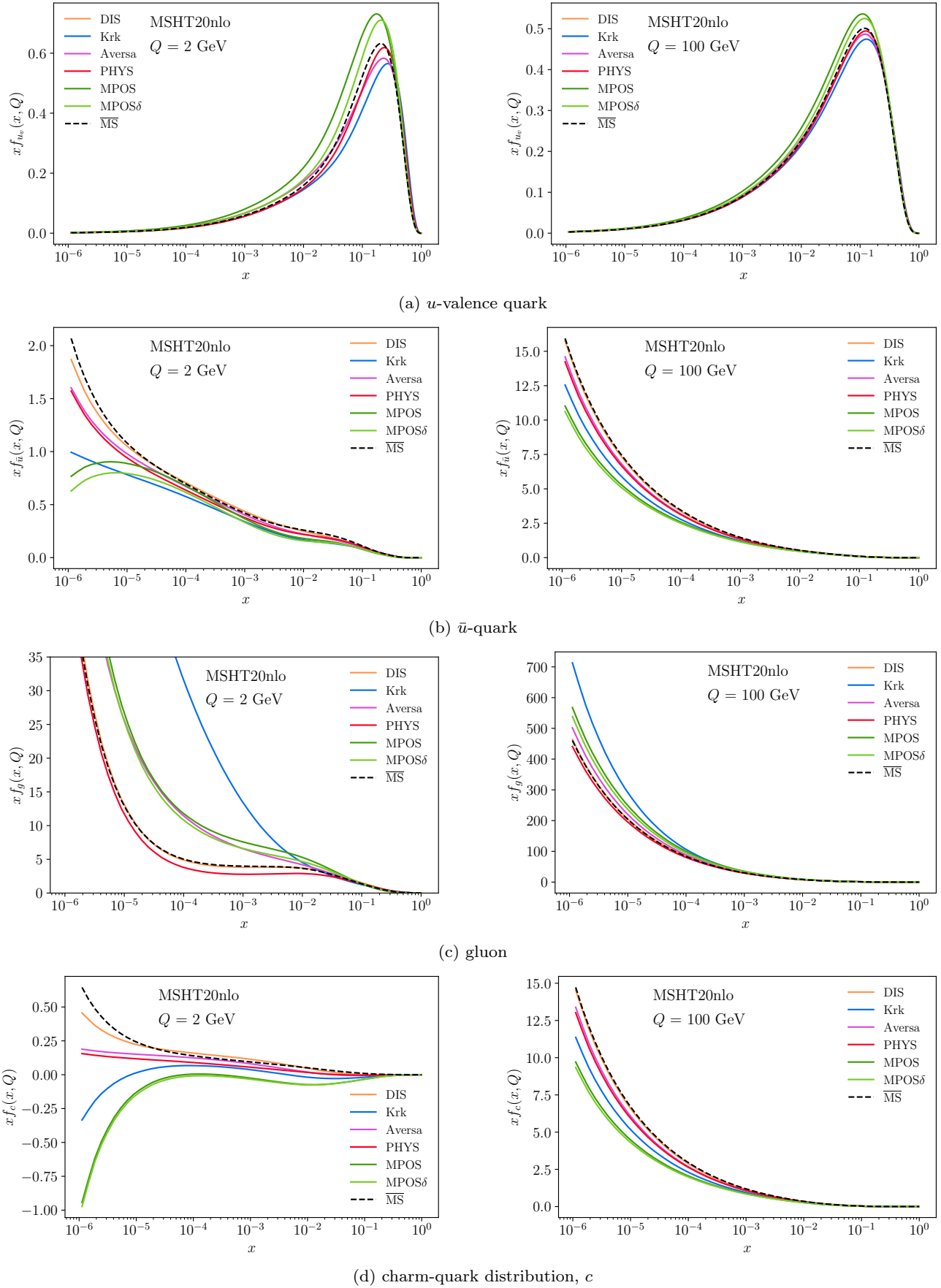


Fig. 18: Comparison of transformed MSHT20nlo PDFs in different schemes for u -valence, \bar{u} , gluon, and charm, at $Q = 2$ GeV (left) and 100 GeV (right). Companion to Fig. 1.

$Q = 100$ GeV (in contrast with $Q = 2$ GeV used in Figs. 2 to 5).

In Figs. 27 to 30 we present decomposition plots analogous to those shown in Figs. 2 to 5 in the main text, using MSHT20n1o and NNPDF40MC in place of CT18NLO, at $Q = 2$ GeV.

Appendix D: Test of perturbative inversion

In this appendix we test numerically the perturbative inversion of each transformation kernel, as summarised in Sec. 2.1.1. For each scheme, we apply the perturbative inverse transformation to the PDF obtained in that scheme by transformation from $\overline{\text{MS}}$. An exact inverse would return the input $\overline{\text{MS}}$ PDF; since we calculate the inverse perturbatively we expect to be discarding terms of order $\mathcal{O}(\alpha_s^2)$. However, the logarithmic terms in the transformation kernels are large and so may in principle not be amenable to perturbative inversion [46].

We show the relative deviation of the resulting PDFs for each of the schemes considered in Tables 1 to 4 in Fig. 31. As expected, at low scales the perturbativity of the transformation breaks down and the error of the perturbative inversion is large. At higher scales the error is within approximately 1% for all schemes.

Appendix E: Validation

In this section we summarise the technical details of the numerical codes used to produce the results presented throughout this paper. The convolution codes used to produce the PDF grids for the various factorisation schemes were written in `python`. In order to implement a robust validation strategy, two independent codes were developed, using different libraries, the first based on `numpy` [97] and `scipy` [98] for fast computation with floating-point precision, and the second using `sympy` [99] for exact symbolic algebra and `mpmath` [100] for numerical calculation with arbitrary-precision arithmetic.

The implementation using `scipy` and `numpy` computes the convolutions using the `quad` routine, with a target maximal absolute error of 10^{-4} . The integrals that appear in Eq. (5) are not computed up to 1, but rather to $1 - 10^{-8}$ to avoid numerical errors due to endpoint-singularities, which was found to give accurate results. Other values of cut-off (both lower and greater) were also tested but they lead to less accurate results.

The second implementation uses symbolic representations of the kernels within `sympy`, which may be converted automatically to `numpy` or `mpmath` functions for

numerical calculations. The symbolic manipulation of the kernels has been used to check the coefficient function results given in Tables 5 to 7, and to produce the plots of their Mellin transforms shown in Fig. 13. For numerical calculations shown here `mpmath` was used with 200 digits of targeted decimal precision, with the aim of eliminating any numerical imprecision due to ‘loss-of-significance’ cancellation errors or the imperfect convergence of numerical integration routines applied to pathological integrands. These were written into LHAPDF output files, using the interpolation knots of the input PDF,²⁸ which were used for subsequent plotting. Where input PDFs are taken from LHAPDF the interpolation of the input PDFs is performed using floating-point precision, so the result may be considered to correspond to the exact convolution to the numerical accuracy of the input (interpolated) PDF with no loss of precision introduced by the transformation.

In both implementations, the KRK-scheme transformations were checked against the original C++ code used for [16–18] which highlighted the possible sensitivity of the convolutions to the numerical integration routine. This comparison helped to benchmark the convolution codes, as well as tune the parameters in the `scipy` implementation. The convolution codes were checked against each other by comparing the outputs for the parton distribution functions, kernel convolutions and momentum sum rules. The discrepancy between the results obtained from the two different implementations were found to be of the order of 10^{-5} .

The PHYS-scheme transformations of the MSTW2008 [63] NLO PDF set displayed in [22] have been repeated using our code and the results compared graphically against the results displayed there.

References

1. G. Altarelli, R. K. Ellis, and G. Martinelli, *Nucl. Phys. B* **143** (1978) 521, [Erratum: *Nucl. Phys. B* **146** (1978) 544].
2. W. A. Bardeen, A. J. Buras, D. W. Duke, and T. Muta, *Phys. Rev. D* **18** (1978) 3998.
3. G. Altarelli, R. K. Ellis, and G. Martinelli, *Nucl. Phys. B* **157** (1979) 461–497.
4. G. Curci, W. Furmanski, and R. Petronzio, *Nucl. Phys. B* **175** (1980) 27–92.
5. W. Furmanski and R. Petronzio, *Z. Phys. C* **11** (1982) 293.
6. H. D. Politzer, *Nucl. Phys. B* **194** (1982) 493–512.
7. P. M. Stevenson and H. D. Politzer, *Nucl. Phys. B* **277** (1986) 758–763.

²⁸Where the input PDF used a single grid we have split the grid at the heavy-flavour thresholds to accommodate the anticipated discontinuities in the transformed PDFs, as outlined in Sec. 2.1.5.

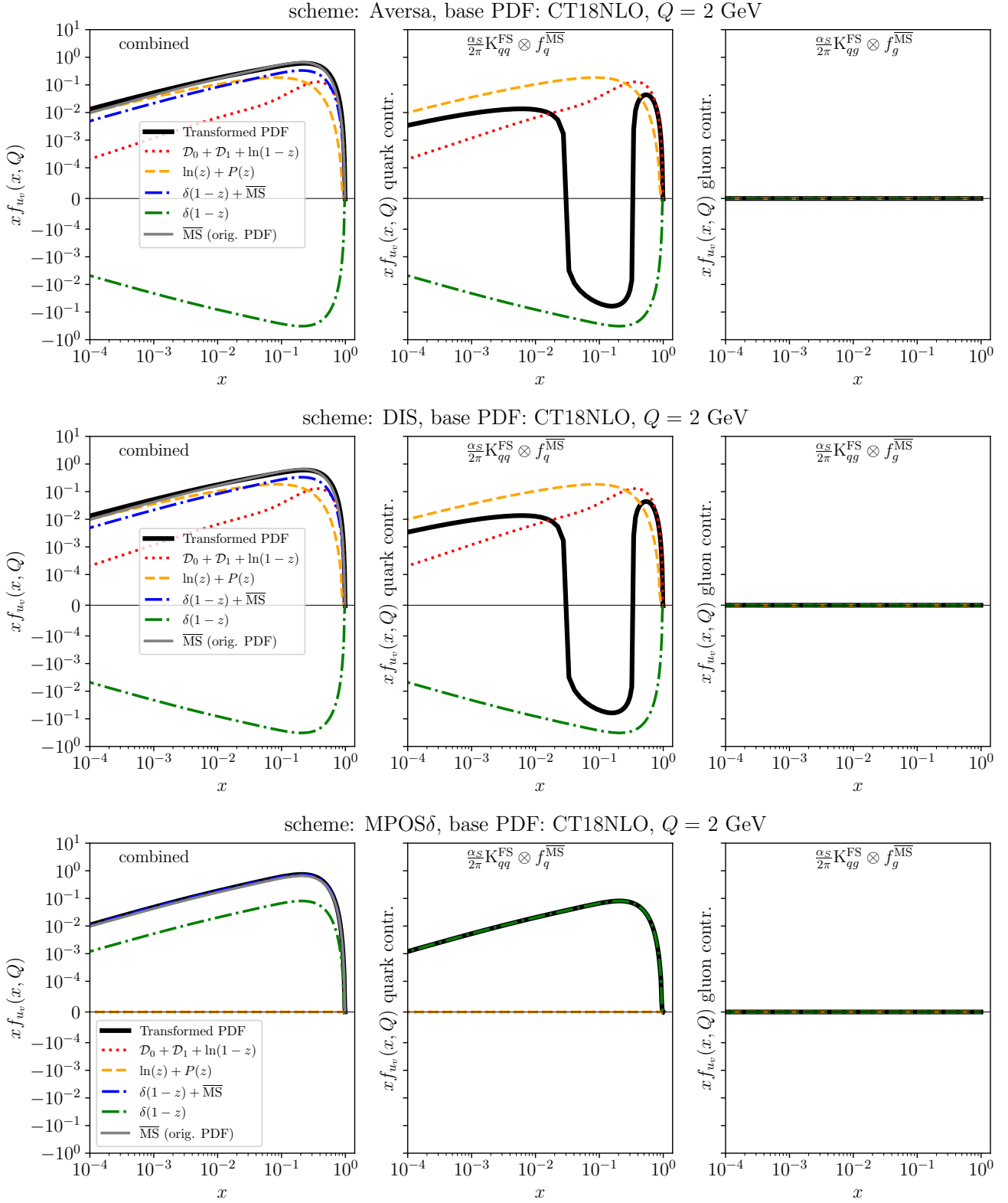


Fig. 19: Decomposition of transformed u_v -quark PDF in the AVERSA, DIS and MPOS δ schemes at factorisation scale $Q = 2$ GeV, as described in Sec. 3.2. Companion to Fig. 2.

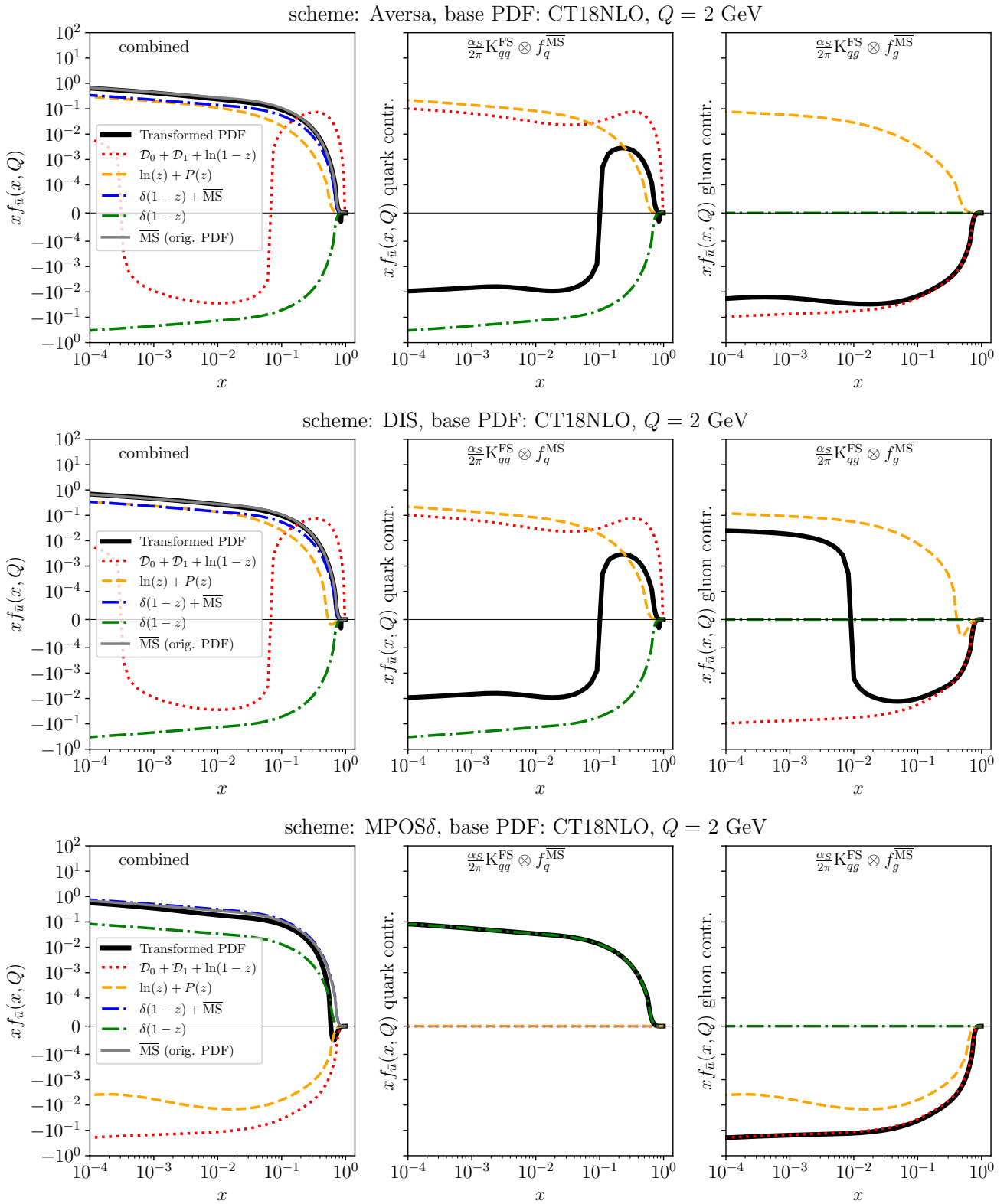


Fig. 20: Decomposition of transformed \bar{u} -quark PDF as a representative of the light sea-quark PDFs, in the AVERSA, DIS and MPOS δ schemes at factorisation scale $Q = 2$ GeV, as described in Sec. 3.2. Companion to Fig. 3.

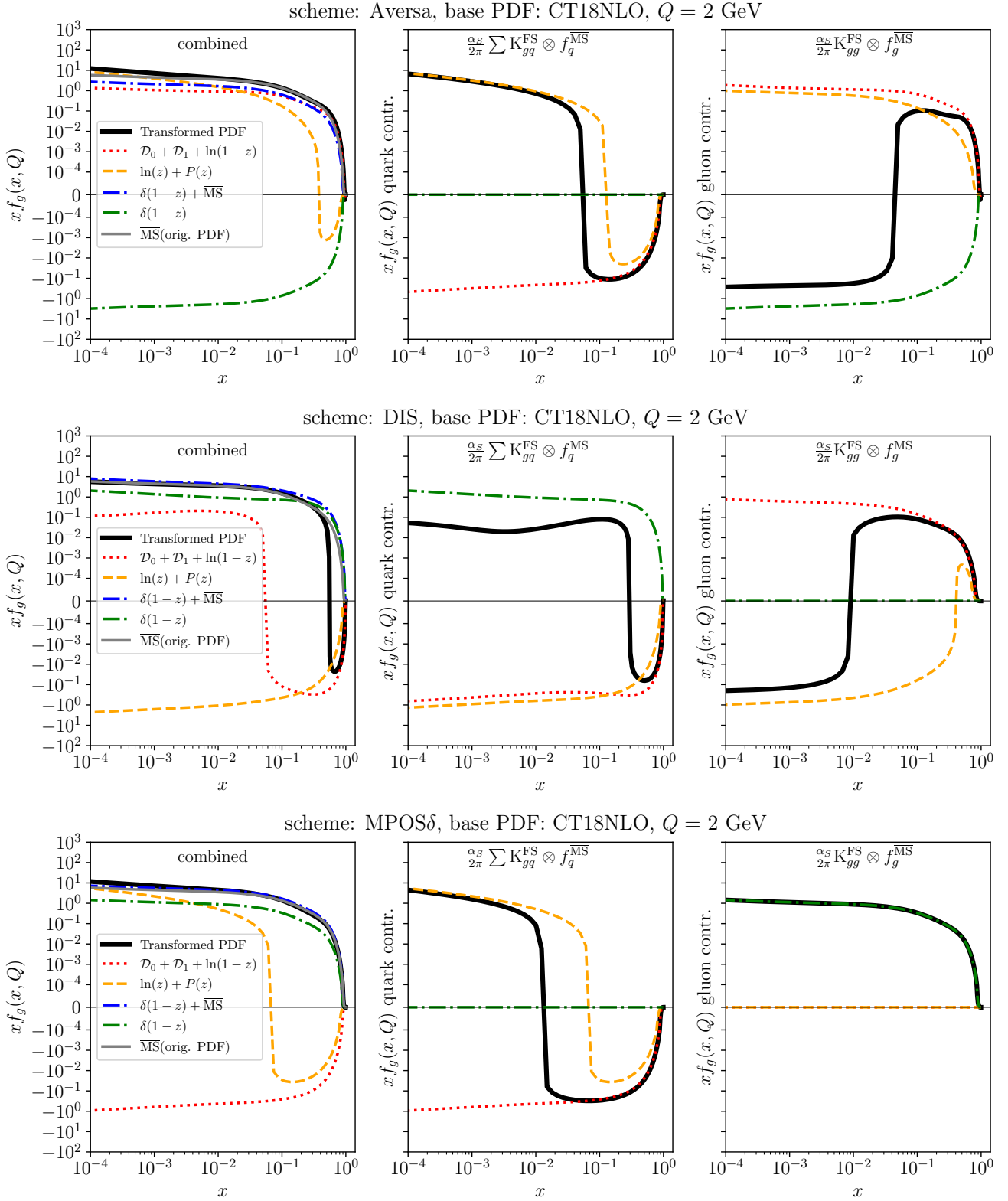


Fig. 21: Decomposition of transformed gluon PDF in the AVERSA, DIS and MPOS δ schemes at factorisation scale $Q = 2$ GeV, as described in Sec. 3.2. Companion to Fig. 4.

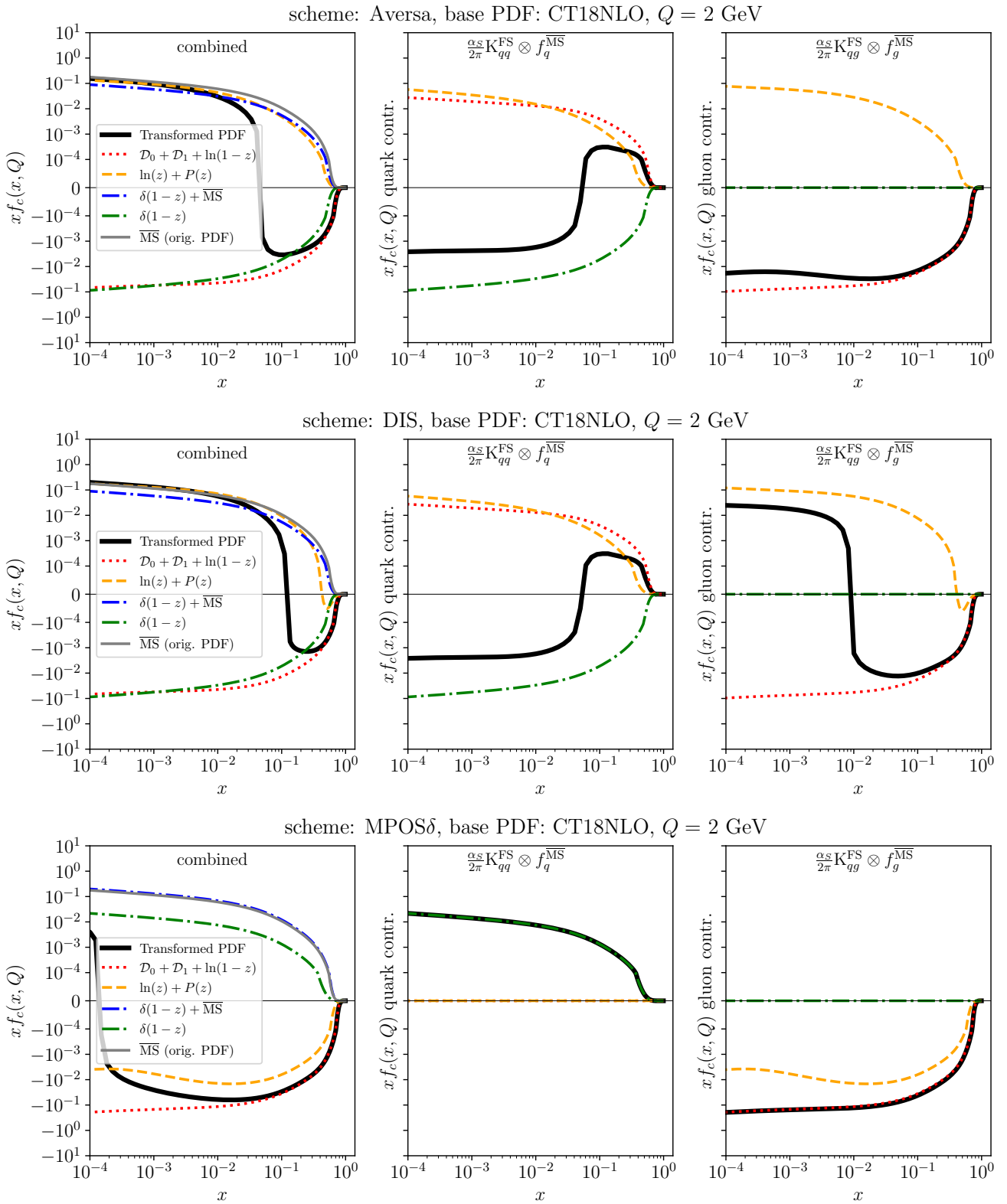


Fig. 22: Decomposition of transformed c -quark PDF as a representative of the heavy flavour PDFs, in the AVERSA, DIS and MPOS δ schemes at factorisation scale $Q = 2$ GeV, as described in Sec. 3.2. Companion to Fig. 5.

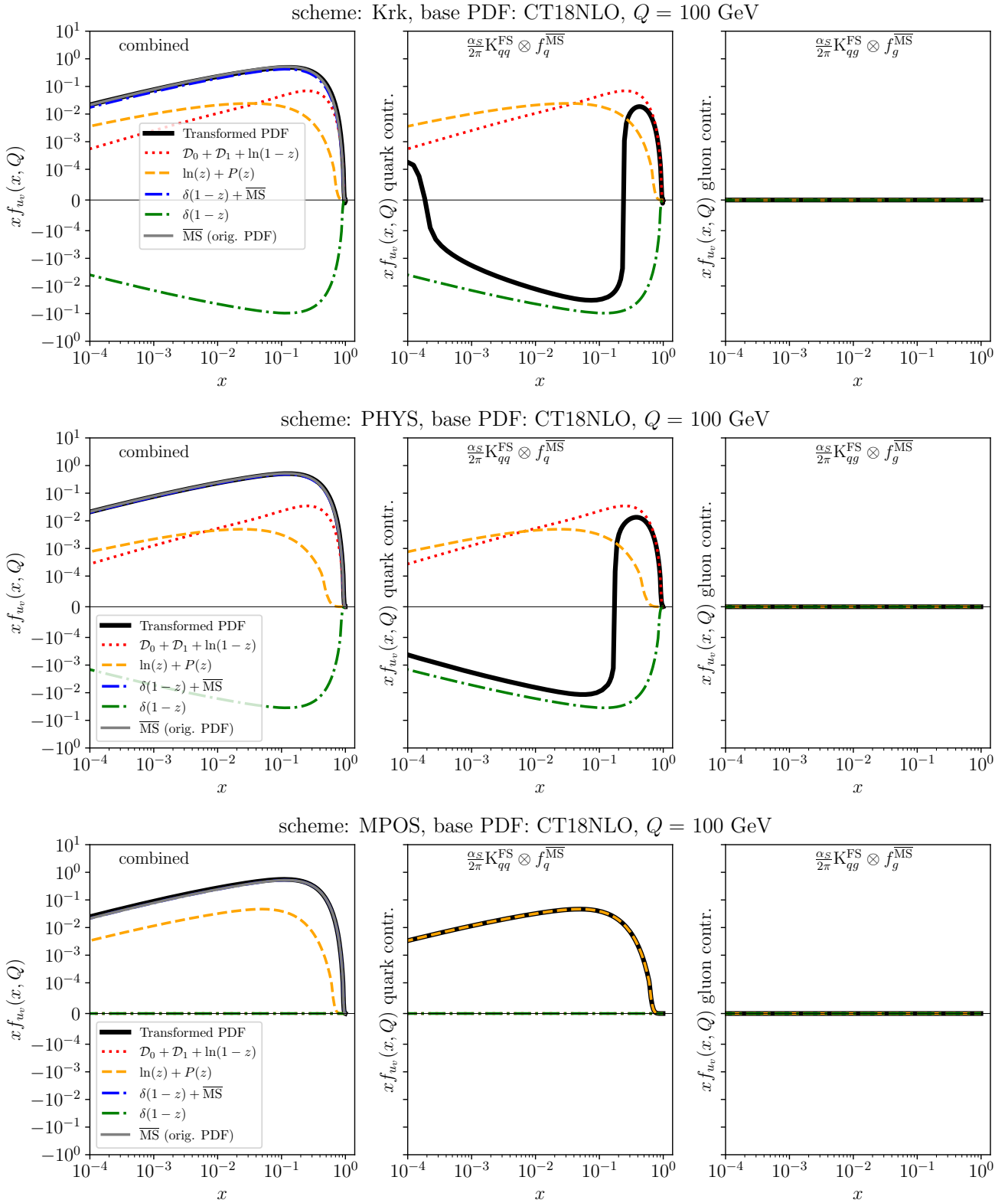


Fig. 23: Decomposition of transformed u_v -quark PDF in the AVERSA, DIS and MPOS δ schemes at factorisation scale $Q = 100$ GeV, as described in Sec. 3.2. Companion to Fig. 2.

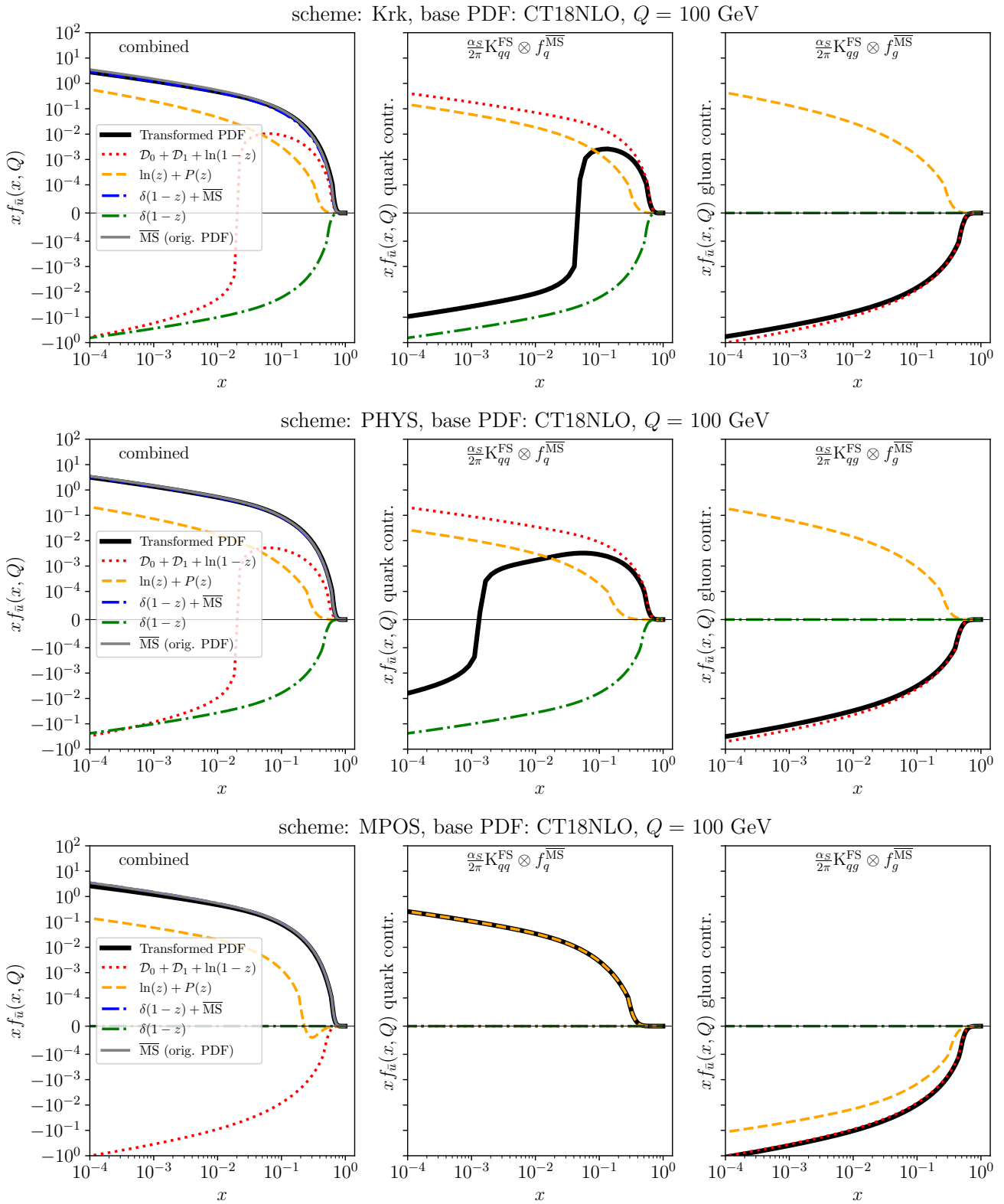


Fig. 24: Decomposition of transformed \bar{u} -quark PDF as a representative of the light sea-quark PDFs, in the AVERSA, DIS and MPOS δ schemes at factorisation scale $Q = 100$ GeV, as described in Sec. 3.2. Companion to Fig. 3.

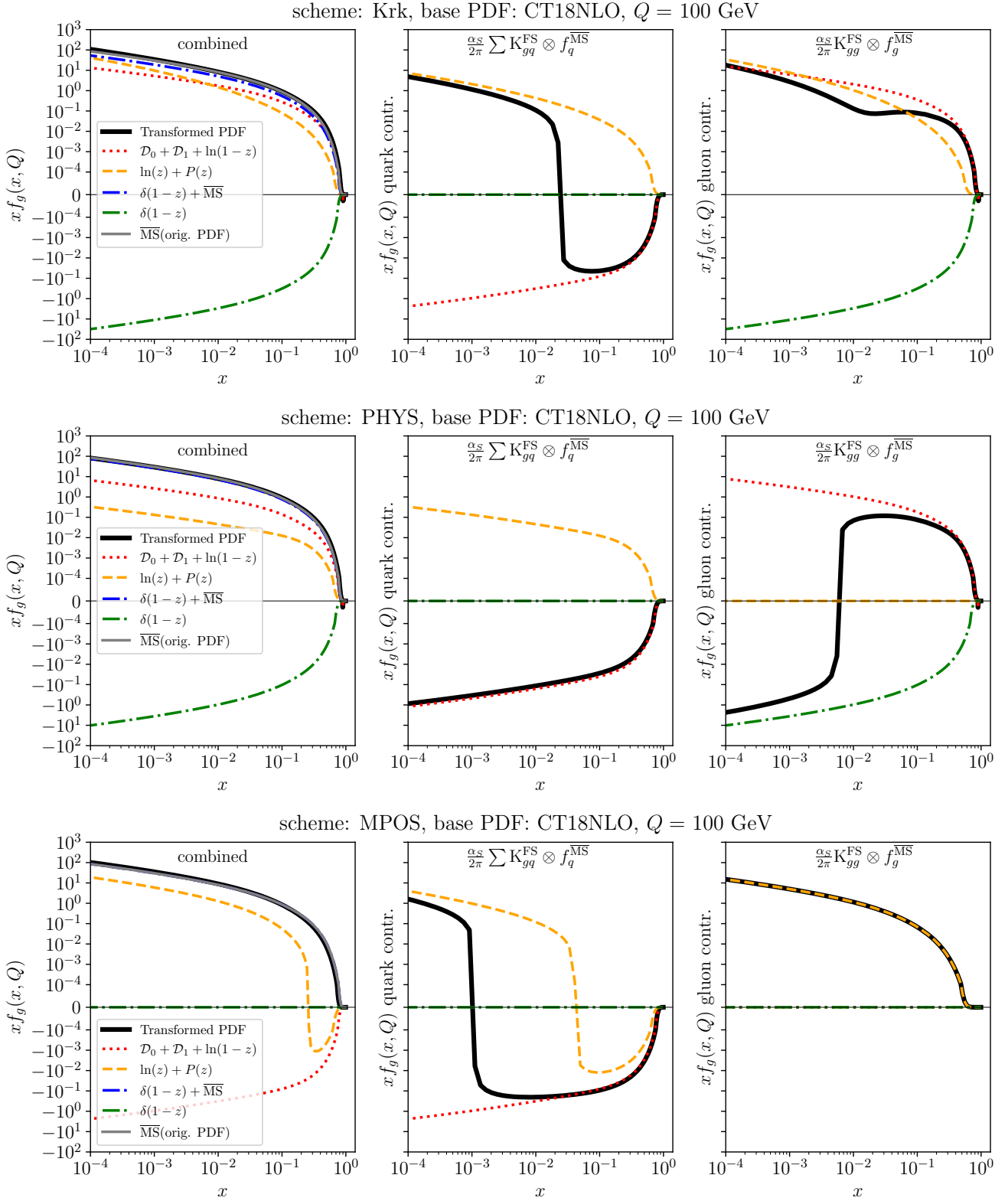


Fig. 25: Decomposition of transformed gluon PDF in the AVERSA, DIS and MPOS δ schemes at factorisation scale $Q = 100$ GeV, as described in Sec. 3.2. Companion to Fig. 4.

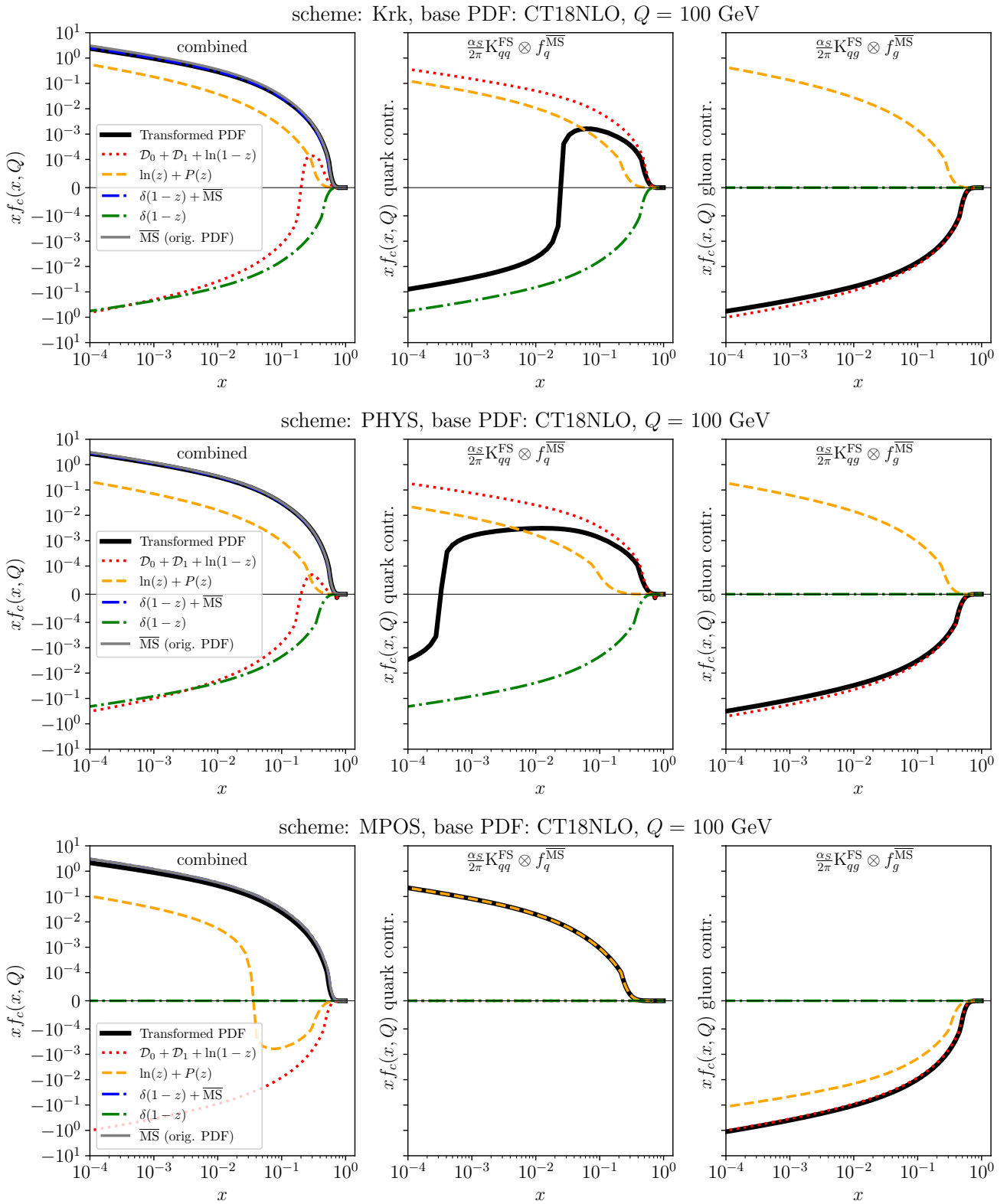


Fig. 26: Decomposition of transformed c -quark PDF as a representative of the heavy flavour PDFs, in the AVERSA, DIS and MPOS δ schemes at factorisation scale $Q = 100$ GeV, as described in Sec. 3.2. Companion to Fig. 5.

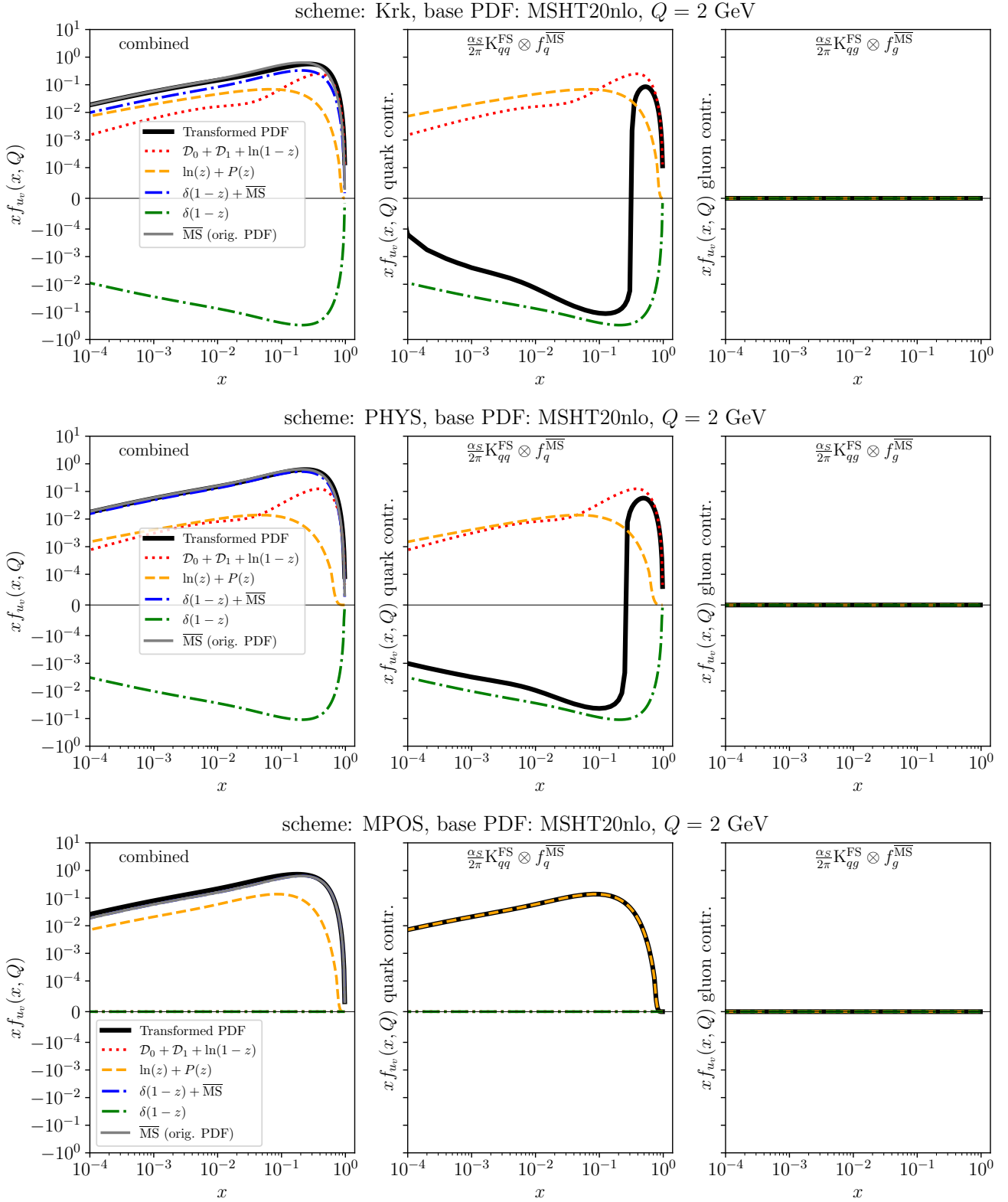


Fig. 27: Decomposition of transformed u_v -quark PDF in the KRK, MPOS, and PHYS schemes at factorisation scale $Q = 2$ GeV, as described in Sec. 3.2, based on MSHT20nlo $\overline{\text{MS}}$ PDFs. Companion to Fig. 2.

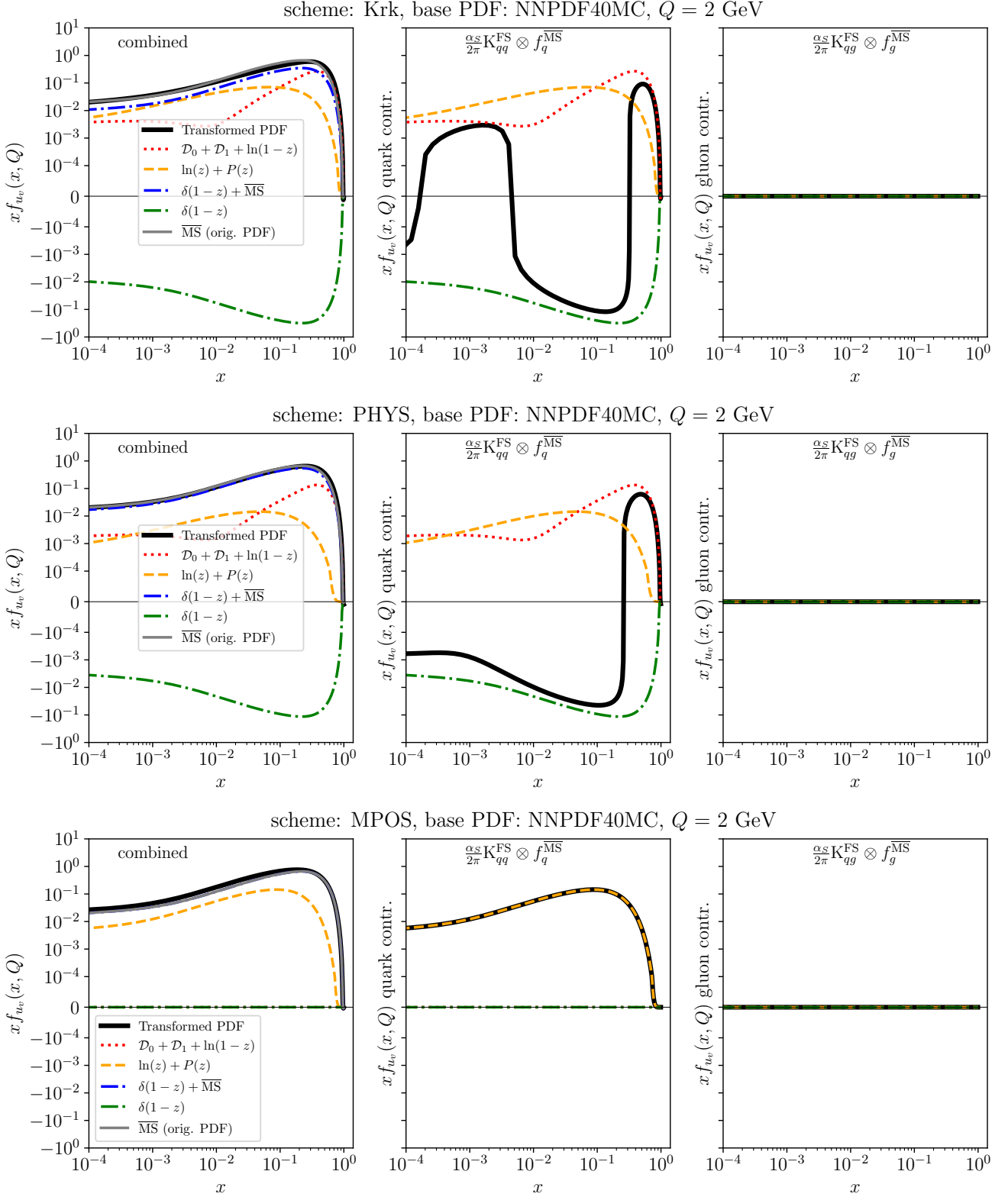


Fig. 28: Decomposition of transformed u_v -quark PDF in the KRK, MPOS, and PHYS schemes at factorisation scale $Q = 2$ GeV, as described in Sec. 3.2, based on NNPDF40MC $\overline{\text{MS}}$ PDFs. Companion to Fig. 2.

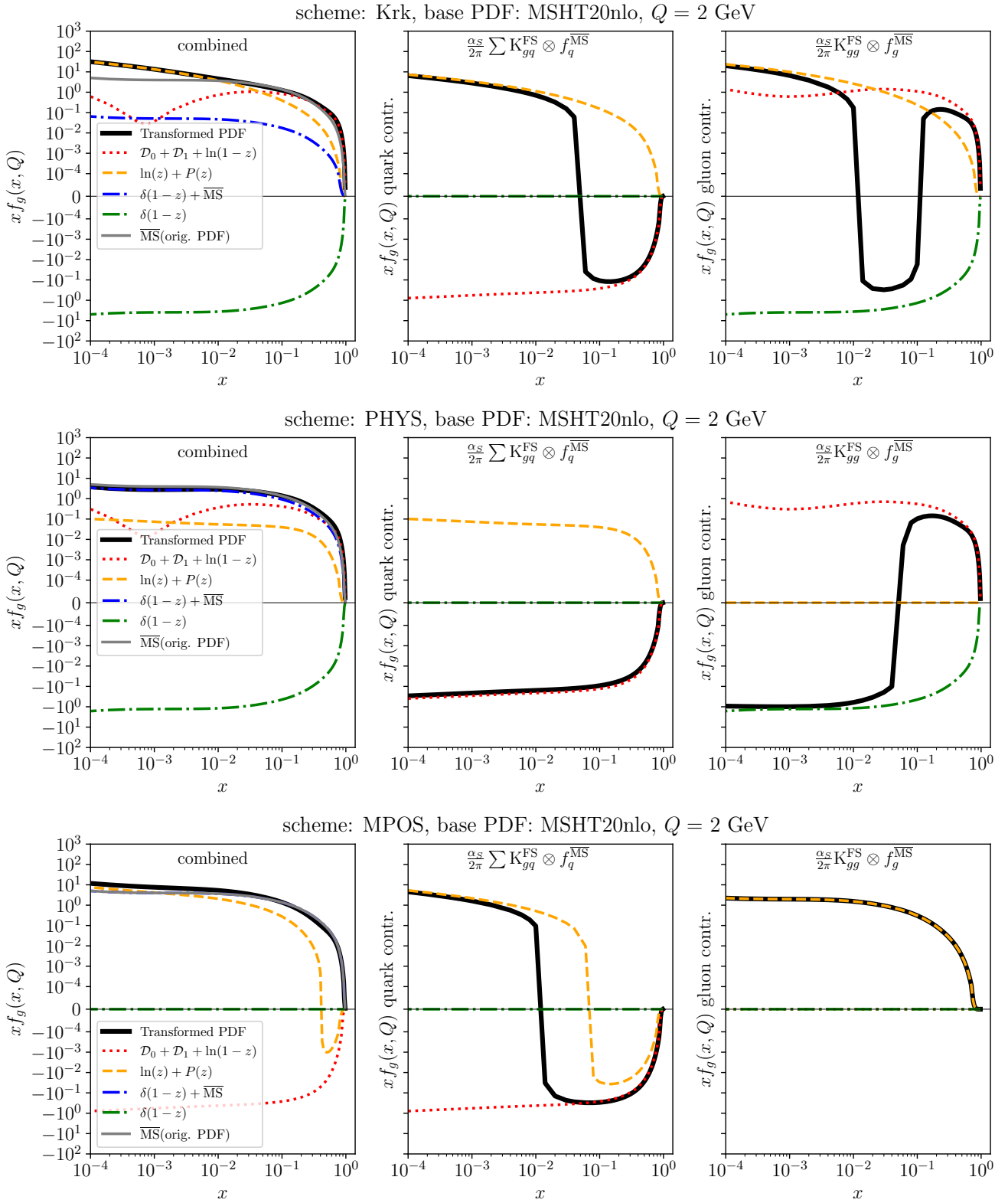


Fig. 29: Decomposition of transformed gluon PDF in the KRK, MPOS, and PHYS schemes at factorisation scale $Q = 2$ GeV, as described in Sec. 3.2, based on MSHT20nlo $\overline{\text{MS}}$ PDFs. Companion to Fig. 4.

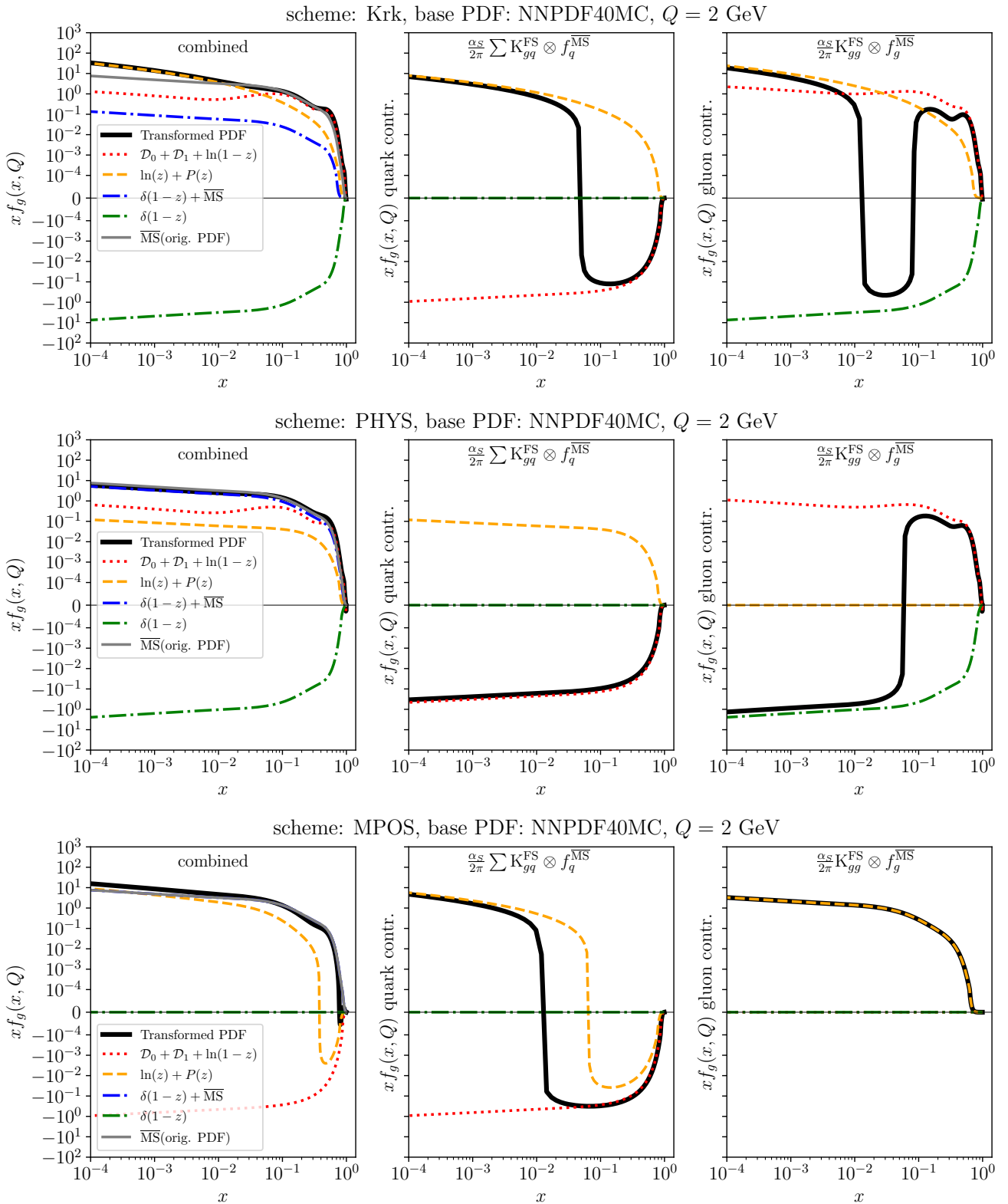


Fig. 30: Decomposition of transformed gluon PDF in the KRK, MPOS, and PHYS schemes at factorisation scale $Q = 2$ GeV, as described in Sec. 3.2, based on NNPDF40MC $\overline{\text{MS}}$ PDFs. Companion to Fig. 4.

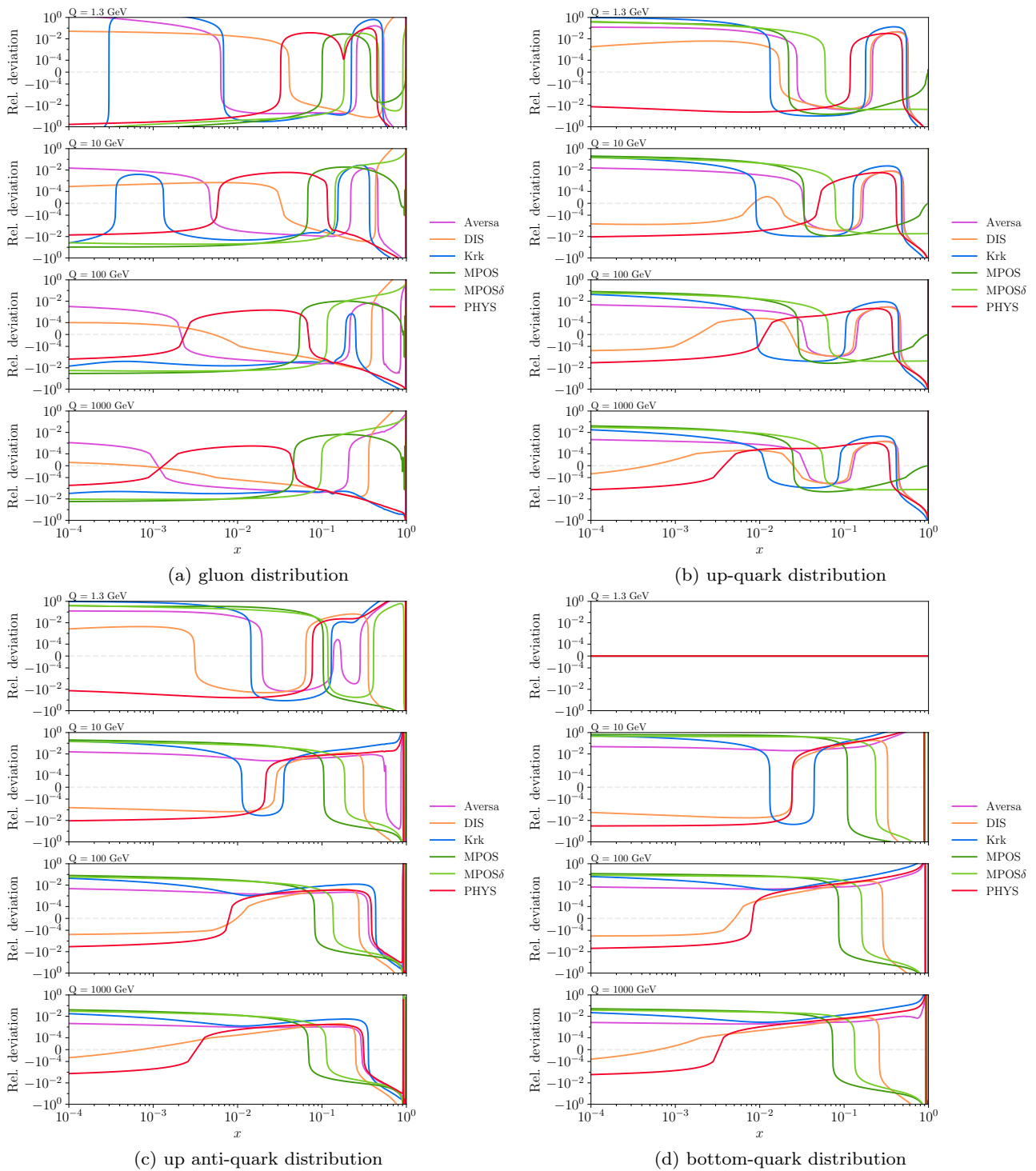


Fig. 31: Test of the perturbative invertibility of the transformation kernels as outlined in [Appendix D](#). For each scheme we plot the relative deviation from unity of the PDF obtained by performing the transformation into the displayed scheme, followed by its perturbative inverse, relative to the original $\overline{\text{MS}}$ PDF. An exact inversion would correspond to a uniform ratio of 1, so a relative deviation of 0. This plot uses the CT18NLO PDF set.

Flavour	Scale Q (GeV)	Factorisation scheme(s)	PDF set/decomposition plots
up-valence u_v (Figs. 1a, 17a and 18a)	2	K _{RK} , PHYS, M _{POS} A _{VERSA} , DIS, M _{POS} δ	CT18 (Fig. 2), MSHT20 (Fig. 27), NNPDF40MC (Fig. 28) CT18 (Fig. 19)
	100	K _{RK} , PHYS, M _{POS}	CT18 (Fig. 23)
up-antiquark \bar{u} (sea) (Figs. 1b, 17b and 18b)	2	K _{RK} , PHYS, M _{POS} A _{VERSA} , DIS, M _{POS} δ	CT18 (Fig. 3) CT18 (Fig. 20)
	100	K _{RK} , PHYS, M _{POS}	CT18 (Fig. 24)
gluon (Figs. 1c, 17c and 18c)	2	K _{RK} , PHYS, M _{POS} A _{VERSA} , DIS, M _{POS} δ	CT18 (Fig. 4), MSHT20 (Fig. 29), NNPDF40MC (Fig. 30) CT18 (Fig. 21)
	100	K _{RK} , PHYS, M _{POS}	CT18 (Fig. 25)
charm (heavy) (Figs. 1d, 17d and 18d)	2	K _{RK} , PHYS, M _{POS} A _{VERSA} , DIS, M _{POS} δ	CT18 (Fig. 5), NNPDF40 (Fig. 6) CT18 (Fig. 22)
	100	K _{RK} , PHYS, M _{POS}	CT18 (Fig. 26)

Table 9: Overview of all factorisation-scheme decomposition plots.

8. A. Ramalho and G. F. Sterman, *Phys. Rev. D* **29** (1984) 2517.
9. G. F. Sterman, *Nucl. Phys. B* **281** (1987) 310–364.
10. P. Aurenche, R. Baier, M. Fontannaz, and D. Schiff, *Nucl. Phys. B* **286** (1987) 509–552.
11. P. Aurenche, R. Baier, A. Douiri, M. Fontannaz, and D. Schiff, *Nucl. Phys. B* **286** (1987) 553–591.
12. F. Aversa, M. Greco, P. Chiappetta, and J. P. Guillet, *Phys. Lett. B* **211** (1988) 465.
13. F. Aversa, P. Chiappetta, M. Greco, and J. P. Guillet, *Nucl. Phys. B* **327** (1989) 105.
14. J. Chyla, *Nucl. Phys. B* **321** (1989) 374–386.
15. A. Candido, S. Forte, and F. Hekhorn, *JHEP* **11** (2020) 129, [2006.07377](#).
16. S. Jadach, W. Płaczek, S. Sapeta, A. Siódmok, and M. Skrzypek, *JHEP* **10** (2015) 052, [1503.06849](#).
17. S. Jadach, W. Płaczek, S. Sapeta, A. Siódmok, and M. Skrzypek, *Eur. Phys. J. C* **76** (2016), no. 12 649, [1606.00355](#).
18. S. Jadach, G. Nail, W. Płaczek, S. Sapeta, A. Siódmok, and M. Skrzypek, *Eur. Phys. J. C* **77** (2017), no. 3 164, [1607.06799](#).
19. S. Jadach, A. Kusina, W. Płaczek, M. Skrzypek, and M. Slawinska, *Phys. Rev. D* **87** (2013), no. 3 034029, [1103.5015](#).
20. P. Sarmah, A. Siódmok, and J. Whitehead, *JHEP* **01** (2025) 062, [2409.16417](#).
21. Z. Nagy and D. E. Soper, *Phys. Rev. D* **106** (2022), no. 1 014024, [2204.05631](#).
22. E. G. Oliveira, A. D. Martin, and M. G. Ryskin, *JHEP* **11** (2013) 156, [1310.8289](#).
23. G. T. Bodwin, *Phys. Rev. D* **31** (1985) 2616, [Erratum: *Phys. Rev. D* **34** (1986) 3932].
24. J. C. Collins, D. E. Soper, and G. F. Sterman, *Nucl. Phys. B* **261** (1985) 104–142.
25. J. C. Collins, *Phys. Rev. D* **58** (1998) 094002, [hep-ph/9806259](#).
26. A. Buckley, J. Ferrando, S. Lloyd, K. Nordström, B. Page, M. Rüfenacht, M. Schönherr, and G. Watt, *Eur. Phys. J. C* **75** (2015) 132, [1412.7420](#).
27. G. Altarelli and G. Parisi, *Nucl. Phys. B* **126** (1977) 298–318.
28. V. N. Gribov and L. N. Lipatov, *Sov. J. Nucl. Phys.* **15** (1972) 438–450.
29. Y. L. Dokshitzer, *Sov. Phys. JETP* **46** (1977) 641–653.
30. C. D. White and R. S. Thorne, *Eur. Phys. J. C* **45** (2006) 179–192, [hep-ph/0507244](#).
31. T. Lappi, H. Mäntysaari, H. Paukkunen, and M. Tevio, *Eur. Phys. J. C* **84** (2024), no. 1 84, [2304.06998](#).
32. T. Lappi, H. Mäntysaari, H. Paukkunen, and M. Tevio, [2412.09589](#).
33. J. C. Collins and D. E. Soper, *Nucl. Phys. B* **194** (1982) 445–492.
34. M. Buza, Y. Matiounine, J. Smith, and W. L. van Neerven, *Eur. Phys. J. C* **1** (1998) 301–320, [hep-ph/9612398](#).
35. T. Stavreva, F. I. Olness, I. Schienbein, T. Jezo, A. Kusina, K. Kovarik, and J. Y. Yu, *Phys. Rev. D* **85** (2012) 114014, [1203.0282](#).
36. V. Bertone, A. Glazov, A. Mitov, A. Papanastasiou, and M. Ubiali, *JHEP* **04** (2018) 046, [1711.03355](#).
37. M. A. G. Aivazis, F. I. Olness, and W.-K. Tung, *Phys. Rev. D* **50** (1994) 3085–3101, [hep-ph/9312318](#).
38. M. A. G. Aivazis, J. C. Collins, F. I. Olness, and W.-K. Tung, *Phys. Rev. D* **50** (1994) 3102–3118, [hep-ph/9312319](#).
39. R. S. Thorne and R. G. Roberts, *Phys. Rev. D* **57** (1998) 6871–6898, [hep-ph/9709442](#).
40. R. S. Thorne, *Phys. Rev. D* **73** (2006) 054019, [hep-ph/0601245](#).
41. M. Cacciari, M. Greco, and P. Nason, *JHEP* **05** (1998) 007, [hep-ph/9803400](#).
42. CTEQ Collaboration, R. Brock *et al.*, *Rev. Mod. Phys.* **67** (1995) 157–248.
43. A. D. Martin, R. G. Roberts, W. J. Stirling, and R. S. Thorne, *Phys. Lett. B* **443** (1998) 301–307, [hep-ph/9808371](#).
44. S. Catani and M. H. Seymour, *Nucl. Phys. B* **485** (1997) 291–419, [Erratum: *Nucl. Phys. B* **510** (1998) 503], [hep-ph/9605323](#).
45. J. Collins, T. C. Rogers, and N. Sato, *Phys. Rev. D* **105** (2022), no. 7 076010, [2111.01170](#).
46. A. Candido, S. Forte, T. Gani, and F. Hekhorn, *Eur. Phys. J. C* **84** (2024), no. 3 335, [2308.00025](#).
47. Z. Nagy and D. E. Soper, *JHEP* **10** (2016) 019, [1605.05845](#).

48. Z. Nagy and D. E. Soper, *Phys. Rev. D* **98** (2018), no. 1 014034, [1705.08093](#).
49. Z. Nagy and D. E. Soper, *JHEP* **06** (2014) 097, [1401.6364](#).
50. Z. Nagy and D. E. Soper, *JHEP* **07** (2015) 119, [1501.00778](#).
51. Z. Nagy and D. E. Soper, *Phys. Rev. D* **99** (2019), no. 5 054009, [1902.02105](#).
52. Z. Nagy and D. E. Soper, *Phys. Rev. D* **105** (2022), no. 5 054012, [2201.08056](#).
53. H. L. Lai, J. Botts, J. Huston, J. G. Morfin, J. F. Owens, J.-W. Qiu, W. K. Tung, and H. Weerts, *Phys. Rev. D* **51** (1995) 4763–4782, [hep-ph/9410404](#).
54. H. L. Lai, J. Huston, S. Kuhlmann, F. I. Olness, J. F. Owens, D. E. Soper, W. K. Tung, and H. Weerts, *Phys. Rev. D* **55** (1997) 1280–1296, [hep-ph/9606399](#).
55. CTEQ Collaboration, H. L. Lai, J. Huston, S. Kuhlmann, J. Morfin, F. I. Olness, J. F. Owens, J. Pumplin, and W. K. Tung, *Eur. Phys. J. C* **12** (2000) 375–392, [hep-ph/9903282](#).
56. T.-J. Hou *et al.*, *Phys. Rev. D* **103** (2021), no. 1 014013, [1912.10053](#).
57. J. Cruz-Martinez, S. Forte, N. Laurenti, T. R. Rabe-mananjara, and J. Rojo, *JHEP* **09** (2024) 088, [2406.12961](#).
58. S. Bailey, T. Cridge, L. A. Harland-Lang, A. D. Martin, and R. S. Thorne, *Eur. Phys. J. C* **81** (2021), no. 4 341, [2012.04684](#).
59. J. Collins, *Foundations of Perturbative QCD*, vol. 32 of *Cambridge Monographs on Particle Physics, Nuclear Physics and Cosmology*. Cambridge University Press, 2011.
60. Private communication with John Collins.
61. NNPDF Collaboration, R. D. Ball, V. Bertone, F. Cerutti, L. Del Debbio, S. Forte, A. Guffanti, J. I. Latorre, J. Rojo, and M. Ubiali, *Nucl. Phys. B* **855** (2012) 153–221, [1107.2652](#).
62. M. Diehl and P. Stienemeier, *Eur. Phys. J. Plus* **135** (2020), no. 2 211, [1904.10722](#).
63. A. D. Martin, W. J. Stirling, R. S. Thorne, and G. Watt, *Eur. Phys. J. C* **63** (2009) 189–285, [0901.0002](#).
64. G. Altarelli, S. Forte, and G. Ridolfi, *Nucl. Phys. B* **534** (1998) 277–296, [hep-ph/9806345](#).
65. H1, ZEUS Collaboration, H. Abramowicz *et al.*, *Eur. Phys. J. C* **75** (2015), no. 12 580, [1506.06042](#).
66. R. D. Ball, L. Del Debbio, S. Forte, A. Guffanti, J. I. Latorre, J. Rojo, and M. Ubiali, *Nucl. Phys. B* **838** (2010) 136–206, [1002.4407](#).
67. NNPDF Collaboration, R. D. Ball, L. Del Debbio, S. Forte, A. Guffanti, J. I. Latorre, A. Piccione, J. Rojo, and M. Ubiali, *Nucl. Phys. B* **809** (2009) 1–63, [Erratum: *Nucl. Phys. B* **816** (2009) 293], [0808.1231](#).
68. J. Pumplin, D. R. Stump, J. Huston, H. L. Lai, P. M. Nadolsky, and W. K. Tung, *JHEP* **07** (2002) 012, [hep-ph/0201195](#).
69. NNPDF Collaboration, R. D. Ball *et al.*, *Eur. Phys. J. C* **82** (2022), no. 5 428, [2109.02653](#).
70. A. Kusina, F. I. Olness, I. Schienbein, T. Jezo, K. Kovarik, T. Stavreva, and J. Y. Yu, *Phys. Rev. D* **88** (2013), no. 7 074032, [1306.6553](#).
71. xFitter Developers Team Collaboration, V. Bertone *et al.*, *Eur. Phys. J. C* **77** (2017), no. 12 837, [1707.05343](#).
72. H1, ZEUS Collaboration, H. Abramowicz *et al.*, *Eur. Phys. J. C* **73** (2013), no. 2 2311, [1211.1182](#).
73. A. M. Cooper-Sarkar, *PoS DIS2010* (2010) 023, [1006.4471](#).
74. R. Gauld, A. Huss, and G. Stagnitto, *Phys. Rev. Lett.* **130** (2023), no. 16 161901, [Erratum: *Phys. Rev. Lett.* **132**, 159901 (2024)], [2208.11138](#).
75. S. Caletti, A. J. Larkoski, S. Marzani, and D. Reichelt, *Eur. Phys. J. C* **82** (2022), no. 7 632, [2205.01109](#).
76. M. Czakon, A. Mitov, and R. Poncelet, *JHEP* **04** (2023) 138, [2205.11879](#).
77. F. Caola, R. Grabarczyk, M. L. Hutt, G. P. Salam, L. Scyboz, and J. Thaler, *Phys. Rev. D* **108** (2023), no. 9 094010, [2306.07314](#).
78. S. Catani and L. Trentadue, *Nucl. Phys. B* **327** (1989) 323–352.
79. S. Catani, M. L. Mangano, P. Nason, and L. Trentadue, *Nucl. Phys. B* **478** (1996) 273–310, [hep-ph/9604351](#).
80. H. Contopanagos, E. Laenen, and G. F. Sterman, *Nucl. Phys. B* **484** (1997) 303–330, [hep-ph/9604313](#).
81. S. Forte and G. Ridolfi, *Nucl. Phys. B* **650** (2003) 229–270, [hep-ph/0209154](#).
82. A. V. Manohar, *Phys. Rev. D* **68** (2003) 114019, [hep-ph/0309176](#).
83. A. Idilbi and X.-d. Ji, *Phys. Rev. D* **72** (2005) 054016, [hep-ph/0501006](#).
84. T. Becher and M. Neubert, *Phys. Rev. Lett.* **97** (2006) 082001, [hep-ph/0605050](#).
85. T. Becher, M. Neubert, and G. Xu, *JHEP* **07** (2008) 030, [0710.0680](#).
86. M. Bonvini, S. Forte, and G. Ridolfi, *Nucl. Phys. B* **847** (2011) 93–159, [1009.5691](#).
87. M. Bonvini, S. Forte, M. Ghezzi, and G. Ridolfi, *Nucl. Phys. B* **861** (2012) 337–360, [1201.6364](#).
88. S. Forte, G. Ridolfi, and S. Rota, *JHEP* **08** (2021) 110, [2106.11321](#).
89. G. Curci and M. Greco, *Phys. Lett. B* **92** (1980) 175–178.
90. P. Anandam and D. E. Soper, *Phys. Rev. D* **61** (2000) 094003, [hep-ph/9912327](#).
91. M. Klasen and G. Kramer, *Phys. Lett. B* **386** (1996) 384–388, [hep-ph/9605210](#).
92. J. Bellm *et al.*, *Eur. Phys. J. C* **76** (2016), no. 4 196, [1512.01178](#).
93. G. Bewick *et al.*, *Eur. Phys. J. C* **84** (2024), no. 10 1053, [2312.05175](#).
94. ATLAS Collaboration, M. Aaboud *et al.*, *Eur. Phys. J. C* **77** (2017), no. 6 361, [1702.05725](#).
95. CMS Collaboration, A. M. Sirunyan *et al.*, *Eur. Phys. J. C* **78** (2018), no. 11 965, [1804.05252](#).
96. M. Cacciari, G. P. Salam, and G. Soyez, *JHEP* **04** (2008) 063, [0802.1189](#).
97. C. R. Harris, K. J. Millman, S. J. van der Walt, R. Gommers, P. Virtanen, D. Cournapeau, E. Wieser, J. Taylor, S. Berg, N. J. Smith, R. Kern, M. Picus, S. Hoyer, M. H. van Kerkwijk, M. Brett, A. Haldane, J. F. del Río, M. Wiebe, P. Peterson, P. Gérard-Marchant, K. Sheppard, T. Reddy, W. Weckesser, H. Abbasi, C. Gohlke, and T. E. Oliphant, *Nature* **585** (Sept., 2020) 357–362.
98. P. Virtanen, R. Gommers, T. E. Oliphant, M. Haberland, T. Reddy, D. Cournapeau, E. Burovski, P. Peterson, W. Weckesser, J. Bright, S. J. van der Walt, M. Brett, J. Wilson, K. J. Millman, N. Mayorov, A. R. J. Nelson, E. Jones, R. Kern, E. Larson, C. J. Carey, Í. Polat, Y. Feng, E. W. Moore, J. VanderPlas, D. Laxalde, J. Perktold, R. Cimrman, I. Henriksen, E. A. Quintero, C. R. Harris, A. M. Archibald, A. H. Ribeiro, F. Pedregosa, P. van Mulbregt, and SciPy 1.0 Contributors, *Nature Methods* **17** (2020) 261–272.

-
99. A. Meurer, C. P. Smith, M. Paprocki, O. Čertík, S. B. Kirpichev, M. Rocklin, A. Kumar, S. Ivanov, J. K. Moore, S. Singh, T. Rathnayake, S. Vig, B. E. Granger, R. P. Muller, F. Bonazzi, H. Gupta, S. Vats, F. Johansson, F. Pedregosa, M. J. Curry, A. R. Terrel, v. Roučka, A. Saboo, I. Fernando, S. Kulal, R. Cimrman, and A. Scopatz, *PeerJ Computer Science* **3** (Jan., 2017) e103.
 100. The mpmath development team, *mpmath: a Python library for arbitrary-precision floating-point arithmetic (version 1.3.0)*, 2023. <http://mpmath.org/>.